

# Quantitative spectroscopy of late O-type main-sequence stars with a hybrid non-LTE method

P. Aschenbrenner<sup>1</sup>, N. Przybilla<sup>1</sup>, and K. Butler<sup>2</sup>

<sup>1</sup> Universität Innsbruck, Institut für Astro- und Teilchenphysik, Technikerstr. 25/8, 6020 Innsbruck, Austria  
e-mail: patrick.aschenbrenner@student.uibk.ac.at ; norbert.przybilla@uibk.ac.at

<sup>2</sup> LMU München, Universitätssternwarte, Scheinerstr. 1, 81679 München, Germany

Received ; accepted

## ABSTRACT

**Context.** Late O-type stars at luminosities  $\log L/L_{\odot} \lesssim 5.2$  show weak winds with mass-loss rates lower than  $10^{-8} M_{\odot} \text{ yr}^{-1}$ . This implies that, unlike their more massive and more luminous siblings, their photospheric layers are not strongly affected by the stellar wind.

**Aims.** A hybrid non-local thermodynamic equilibrium (non-LTE) approach – line-blanketed hydrostatic model atmospheres computed under the assumption of LTE in combination with non-LTE line-formation calculations – is tested for analyses of late O-type stars with masses up to  $\sim 25 M_{\odot}$ . A sample of 20 mostly sharp-lined Galactic O stars of spectral types O8 to O9.7 and luminosity classes V and IV, previously studied in the literature using full non-LTE model atmospheres, is investigated.

**Methods.** Hydrostatic and plane-parallel atmospheric structures and synthetic spectra computed with Kurucz’s ATLAS12 code together with the non-LTE line-formation codes DETAIL and SURFACE, which account for the effects of turbulent pressure on the atmosphere, were employed. High-resolution spectra were analysed for atmospheric parameters using hydrogen lines, multiple ionisation equilibria, and elemental abundances. Fundamental stellar parameters were derived by considering stellar evolution tracks and *Gaia* Early Data Release 3 (EDR3) parallaxes. Interstellar reddening was characterised by fitting spectral energy distributions from the UV to the mid-IR.

**Results.** A high precision and accuracy is achieved for all derived parameters for 16 sample stars (4 objects show composite spectra). Turbulent pressure effects turn out to be significant for the quantitative analysis. Effective temperatures are determined to 1-3% uncertainty levels, surface gravities to 0.05 to 0.10 dex, masses to better than 8%, radii to better than 10%, and luminosities to better than 20% uncertainty typically. Abundances for C, N, O, Ne, Mg, Al, and Si are derived with uncertainties of 0.05 to 0.10 dex and for helium within 0.03 to 0.05 dex ( $1\sigma$  standard deviations) in general. Overall, results from previous studies using unified photosphere plus wind (full) non-LTE model atmospheres are reproduced, and with higher precision. The improvements are most pronounced for elemental abundances, and smaller microturbulent velocities are found. An overall good agreement is found between our spectroscopic distances and those from *Gaia*. *Gaia* EDR3-based distances to the Lac OB1b association and to the open clusters NGC 2244, IC 1805, NGC 457, and IC 1396 are determined as a byproduct. The derived N/C versus N/O abundance ratios tightly follow the predictions from stellar evolution models. Two ON stars show a very high degree of mixing of CNO-processed material and appear to stem from binary evolution.

**Key words.** Stars: abundances – Stars: atmospheres – Stars: early-type – Stars: evolution – Stars: fundamental parameters – Stars: massive

## 1. Introduction

The O stars span the widest range of masses of all the spectral types of the Morgan-Keenan (MK) sequence, from about  $18 M_{\odot}$  at the transition to the main-sequence B stars to upper masses beyond  $100 M_{\odot}$ . They and their progeny (e.g. blue supergiants, luminous blue variables, and Wolf-Rayet stars) are the main sources of ionising UV photons in star-forming galaxies and of momentum input to the interstellar medium (ISM) via intense stellar winds that dominate their evolution throughout their short lifetimes. The ends of their lives give rise to some of the most extreme galactic objects, such as core-collapse supernovae, and, in some cases, to long-duration soft-spectrum gamma-ray bursts (Maeder & Meynet 2012). Their typical stellar remnants are black holes. Binary O stars can form black hole binaries that can coalesce within a Hubble time, yielding measurable gravitational wave events. O-type stars are therefore widely studied for all these aspects, and many more.

The O-star regime is a domain for hydrodynamical modelling as mass outflows are a dominant factor throughout all phases of their lives (e.g. Chiosi & Maeder 1986; Puls et al. 2008). However, among them exists the class of the so-called weak-wind O stars. Their existence was finally recognised with the work of Martins et al. (2005) – and subsequent work by Marcolino et al. (2009) and de Almeida et al. (2019) – on metal-rich Galactic O stars, despite earlier findings in the low-metallicity Small Magellanic Cloud (SMC; Bouret et al. 2003; Martins et al. 2004) that were less conclusive, and some first indications date back as early as the work of Chlebowski & Garmy (1991). These weak-wind O stars have a low luminosity, with  $\log L/L_{\odot} \lesssim 5.2$ , and show mass-loss rates lower than  $10^{-8} M_{\odot} \text{ yr}^{-1}$ , weaker by up to two orders of magnitude than predicted by standard wind theory (Vink et al. 2000, 2001, but see Vink & Sander 2021 and Marcolino et al. 2022 for more recent results, and Lucy 2010 and Sundqvist et al. 2019 for alternative approaches). Terminal velocities of low-luminosity O stars were also found to be low, such that the conjunction with low mass-

loss rates implied a reduced line-force parameter,  $\alpha$  (e.g. Martins et al. 2005). A physical trigger mechanism for the weak-wind phenomenon may be X-ray emission from shocked gas in the optically thin stellar wind that penetrates into the region below the critical point, thus reducing the radiative acceleration and the mass-loss rate because of surplus ionisation (Drew et al. 1994; see e.g. Martins et al. 2005 and Puls et al. 2008 for further discussion). However, the issue has not yet been settled conclusively.

Low-luminosity O stars were subjected to analysis with hydrostatic hydrogen+helium model atmospheres in radiative equilibrium that accounted for deviations from local thermodynamic equilibrium (LTE; so-called non-LTE models) as early as the seminal work by Auer & Mihalas (1972). A focus on applications of such models was given in the analysis of a few nitrogen-rich ON stars by Schönberner et al. (1988), which exposed material processed by the CNO cycle on their surfaces and on luminosity effects at spectral class O9.5 by Voels et al. (1989). Several low-luminosity O stars were investigated by Herrero et al. (1992) within a larger sample of O stars, who identified the fundamental problem of the mass discrepancy, the mismatch between spectroscopically derived masses and evolutionary masses, and the helium discrepancy. Hydrostatic H+He non-LTE atmospheres were used for the last time in the works of Villamariz et al. (2002) and Villamariz & Herrero (2005) to derive helium and CNO abundances. These works used follow-up non-LTE line-formation calculations that considered the effects of metal line blocking and a consistent treatment of microturbulence (Villamariz & Herrero 2000). They provided observational constraints for rotational mixing of CNO-cycled products in late O-type stars for comparison with predictions from the first stellar evolution grids of rotating massive stars that had become available at that time (Heger & Langer 2000; Meynet & Maeder 2000).

In that period, unified model atmospheres – self-consistent spherically extended hydrodynamic non-LTE atmospheres that combine photospheric layers at subsonic velocities with the supersonic stellar wind – became available. Initially, H+He compositions were realised (Santolaya-Rey et al. 1997), and applications mostly ignored low-luminosity O stars (Puls et al. 1996). Further methodological progress was made by considering non-LTE metal line blanketing and including iron-group elements, first for hydrostatic atmospheres with the codes PAM (Grigsby et al. 1992) and TLUSTY (Hubeny & Lanz 1995) and later for unified photosphere plus wind models with CMFGEN (Hillier & Miller 1998), PoWR (Gräfener et al. 2002), and FASTWIND (Puls et al. 2005).

First applications of these modern unified non-LTE models included the stellar parameter determination for the low-luminosity standard O star 10 Lac (Herrero et al. 2002) and work on SMC stars (Bouret et al. 2003; Martins et al. 2004) and Galactic objects that established the weak-wind phenomenon (Martins et al. 2005). Investigations of the Orion Trapezium cluster and comparison stars followed (Simón-Díaz et al. 2006), extending the discussion to refined rotational velocities and elemental abundances.

Further progress led to more comprehensive investigations that included a full spectral synthesis of the UV and optical spectra of O stars, including weak-wind stars (e.g. Martins et al. 2012). Elemental abundance investigations concentrated on nitrogen, which shows the strongest changes when mixing with CNO-processed material occurs, seen in particular in the ON stars (Walborn et al. 2011; Martins et al. 2015b). These investigations were later extended to include all three elements, carbon, nitrogen, and oxygen (Martins et al. 2015a; Carneiro et al.

2019), in order to trace the full CNO signature in the main-sequence evolution and beyond (Przybilla et al. 2010; Maeder et al. 2014). At about the same time, interest in the effects of magnetic fields on the atmospheres of massive stars and their evolution grew. Among other massive stars, a number of weak-wind O stars were investigated for the presence of magnetic fields via two large spectropolarimetric surveys, the B fields in OB stars (BOB; Morel et al. 2015; Fossati et al. 2015; Schöller et al. 2017) and the Magnetism in Massive Stars (MiMeS) surveys (Wade et al. 2016). Finally, the availability of larger samples of high-resolution spectra of O stars, in particular from the IACOB project – including many weak-wind objects – led to mass quantitative analyses, for example with respect to rotational velocities and additional line-broadening effects (Simón-Díaz & Herrero 2014) and stellar parameters (Holgado et al. 2018, 2022).

All numerical modelling must make assumptions and simplifications in order to handle real stellar atmospheres. As a consequence, not all aspects of the observations will be reproduced perfectly. For example, the following two issues can be improved in the quantitative analysis of weak-wind, low-luminosity O stars. First of all, a solution to the He I singlet problem is desirable. It is difficult to reproduce singlet and triplet lines simultaneously with non-LTE codes at effective temperatures of about 35 000 K (Najarro et al. 2006), though workarounds exist (Puls et al. 2020). Secondly, the abundance determinations of these stars are afflicted with large uncertainties, which can reach more than 0.3 dex (Martins et al. 2015a), in contrast to a mere 0.05 to 0.10 dex for just slightly cooler early B-type stars (e.g. Nieva & Przybilla 2012). This is attributed to non-LTE effects that are much more severe in O stars than in B stars (Martins et al. 2015a).

Such challenges are the motivation for the present work, which aims to improve the accuracy and, in particular, the precision of weak-wind, low-luminosity O-star analyses in order to provide tight observational constraints on photospheric conditions for future work on the weak-wind problem. These analyses provide the boundary conditions for the base of the stellar wind, the place where the (unexpectedly low) mass-loss rate is initiated.

Further motivation comes from the availability of results from the *Gaia* mission (Gaia Collaboration et al. 2016), and in particular from the Early Data Release 3 (EDR3; Gaia Collaboration et al. 2021), which have a strong impact on the determination of fundamental stellar parameters for all kinds of stars. These results have so far not been considered for weak-wind late O-type stars. Parallaxes for massive stars still tend to have substantial uncertainties in many cases, but often the stars are still located in the OB associations or open star clusters where they were formed. This offers the possibility of verifying stellar characteristics more precisely than is feasible from the individual distances alone – an advantage that is exploited here.

The paper is organised as follows. Observations and data reduction are discussed in Sect. 2. An overview of the models used for the analysis is given in Sect. 3 and of the analysis methodology in Sect. 4. Results from the star sample analysis are summarised in Sect. 5. Finally, a summary of the individual objects is given in Sect. 6 to round out their characterisation, and a general summary and discussion are presented in Sect. 7. Appendices A and B discuss the distance determination and show exemplary spectrum fits for the standard star 10 Lac, and Appendices C to F discuss sample star distances in the context of the host star clusters NGC 2244, IC 1805, NGC 457, and IC 1396.

**Table 1.** Overview of the sample stars and observing log.

ID#	Object	Common name	Sp.T. <sup>a</sup>	V <sup>b</sup> mag	B – V <sup>b</sup> mag	U – B <sup>b</sup> mag	Date YYYY-MM-DD	T <sub>exp</sub> s	S/N
ESPaDOnS $R = 68\,000$									
1 <sup>f</sup>	HD 66788		O8 V	9.454(10)	–0.077(14)	–0.931(19)	2010-02-01	2400	180
2	HD 14633		ON8.5 V	7.459(12)	–0.204(13)	–1.050(28)	2009-10-09	5200	430
3 <sup>f</sup>	HD 37061	NU Ori	O9 V <sup>c</sup>	6.830	0.23	–0.59	2007-03-08	3 × 3200	700
4	HD 258691		O9 V	9.700(0)	0.570(0)	–0.453(15)	2008-01-23	2 × 3440	200
5	HD 201345		ON9.2 IV	7.660	–0.130	–0.950	2010-07-26	2800	220
6	HD 57682		O9.2 IV	6.418(8)	–0.189(6)	–1.026(4)	2009-05-04	2 × 2400	700
7	HD 227757		O9.5 V	9.217(13)	0.186(13)	–0.744(5)	2010-07-26	1160	90
8	BD –13 4930		O9.5 V	9.435(7)	0.273(17)	–0.709(32)	2010-06-25	3200	140
9	BD +60 499		O9.5 V	10.300(23)	0.542(7)	–0.507(9)	2008-08-19	3200	120
10	BD +57 247		O9.5 IV <sup>d</sup>	9.941(10)	0.204(5)	–0.704(5)	2014-02-13	6960	160
11	HD 207538		O9.7 IV	7.305(14)	0.324(8)	–0.640(0)	2008-07-30	4000	400
FEROS $R = 48\,000$									
12 <sup>f</sup>	HD 46966		O8.5 IV	6.881(11)	–0.055(15)	–0.912(12)	2006-01-03, 2006-01-05	2 × 600	550
13	HD 46202		O9.2 V	8.186(15)	0.178(11)	–0.737(13)	2008-04-16 to 19, 2008-04-26	6 × 720	400
14	HD 38666	μ Col	O9.5 V	5.169(4)	–0.281(6)	–1.077(64)	2011-11-07	120	300
15 <sup>f</sup>	HD 155889		O9.5 IV	6.551(9)	–0.016(8)	–0.881(13)	2012-05-20	400	320
16	HD 54879		O9.7 V <sup>e</sup>	7.638(13)	–0.007(4)	–0.867(4)	2012-05-19	600	260
FOCES $R = 40\,000$									
17	HD 214680	10 Lac	O9 V	4.879(14)	–0.201(8)	–1.036(10)	2005-09-21	6 × 600	400
18	HD 34078	AE Aur	O9.5 V	5.956(15)	0.225(5)	–0.704(15)	2005-09-21	2 × 540, 3 × 450	250
19	HD 206183		O9.5 V	7.419(11)	0.126(12)	–0.787(5)	2005-09-27	2700	200
20	HD 36512	ν Ori	O9.7 V	4.618(13)	–0.264(7)	–1.068(8)	2005-09-28	2 × 360	300

**Notes.** <sup>(a)</sup> Spectral types for most objects were adopted from Martins et al. (2015a), which are mostly based on the work of Sota et al. (2011, 2014)

<sup>(b)</sup> Mermilliod (1997), Morel & Magnenat (1978) <sup>(c)</sup> Bragança et al. (2012) <sup>(d)</sup> Hoag & Applequist (1965) <sup>(e)</sup> Sota et al. (2011) <sup>(f)</sup> These stars show spectroscopic binarity or multiplicity and are excluded from the detailed analyses.

## 2. Observations and data reduction

For our analysis, we obtained spectra of 20 late O-type dwarfs, ranging from O9.7 to O8 in spectral type and IV to V in luminosity class. All have been subjected to quantitative analysis before (17 objects alone were investigated by Martins et al. 2015a), sometimes by several independent studies. Most of the sample stars are apparently slow rotators that show sharp lines. They were found to be single, to be single-lined binary members (SB1), or to have only spatially resolved binary or multiple partners that were not expected to contribute second light to the recorded spectra (see the details below).

Table 1 gives an overview of the sample stars, ordered by spectral type for the observations per instrument and an observing log. An internal ID number is given, the object is identified by its Henry-Draper (HD) or its Bonner Durchmusterung (BD) designation, where applicable a common name is given, the V magnitude and the B – V and U – B colours, the observing date(s), exposure time(s)  $T_{\text{exp}}$  and the resulting signal-to-noise ratio (S/N) of the analysed spectrum, measured at  $\sim 5000\text{ Å}$ .

Eleven stars were observed with the Echelle Spectro-Polarimetric Device for the Observation of Stars (ESPaDOnS; Manset & Donati 2003) on the 3.6 m Canada-France-Hawaii Telescope (CFHT) at Mauna Kea, Hawaii. The spectra cover a wavelength range from 3700 to 10 500 Å at a resolving power of  $R = \lambda/\Delta\lambda \approx 68\,000$ . An additional five stars were observed with the Fiberfed Extended Range Optical Spectrograph (FEROS; Kaufer et al. 1999) on the Max-Planck-Gesellschaft/European Southern Observatory (ESO) 2.2 m telescope at La Silla in Chile, with a wavelength coverage from 3600 to 9200 Å at  $R \approx 48\,000$ . The remaining four stars were observed with the Fibre Optics Cassegrain Echelle Spectrograph (FOCES; Pfeiffer et al. 1998)

on the 2.2 m telescope at the Calar Alto Observatory in Spain. The FOCES spectra cover a wavelength range from 3860 to 9400 Å with  $R \approx 40\,000$ .

In the case of ESPaDOnS, pipeline-reduced spectra were downloaded from the CFHT Science Archive at the Canadian Astronomy Data Centre<sup>1</sup> and in the case of FEROS, Phase 3 data from the ESO Science Portal<sup>2</sup>. The spectra were normalised by fitting a spline function through carefully selected continuum points. For FOCES the raw data needed to be reduced. Initially, a median filter was applied to the raw images to remove bad pixels and cosmics. The FOCES semi-automatic pipeline (Pfeiffer et al. 1998) was then used for the data reduction: subtraction of bias and darks, flat-fielding, wavelength calibration based on Th-Ar exposures, rectification and merging of the echelle orders. Finally, the spectra were shifted into the laboratory rest frame via cross-correlation with appropriate synthetic spectra. If multiple spectra – preferably from the same night – were available, we co-added them to increase the S/N.

Examples of the final spectra are shown in Fig. 1 for three spectral windows. Optical spectra of late O-type stars are highly valuable for elemental abundance determinations because they show the largest line density among the O stars, making the largest number of chemical elements accessible. This line density rapidly declines towards hotter temperatures and for increasing rotational velocity. Most of the sample stars are slow rotators with (projected) rotational velocity  $v \sin i \lesssim 30\text{ km s}^{-1}$ , HD 14633 in Fig. 1 belongs to the three faster rotators investigated here, with  $v \sin i \approx 100\text{ km s}^{-1}$ . It should be noted that a few of the stars

<sup>1</sup> <https://www.cadc-ccda.hia-ihp.nrc-cnrc.gc.ca/en/cfht/>

<sup>2</sup> <https://archive.eso.org/scienceportal/home>



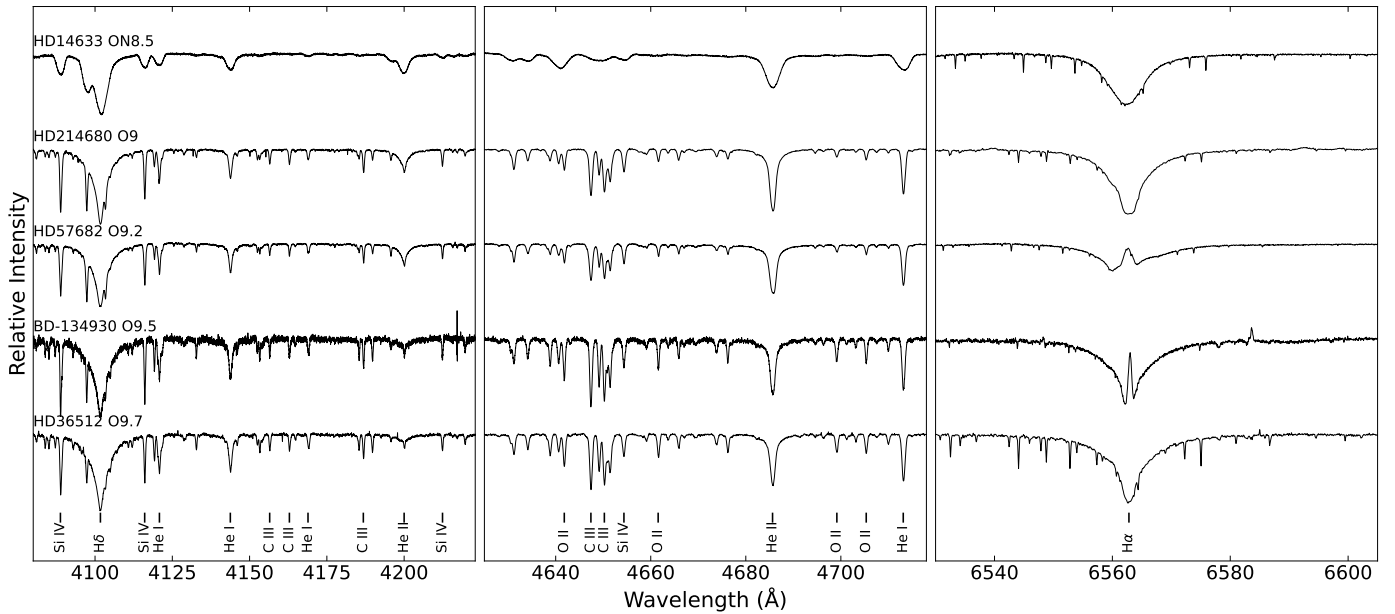


**Fig. 1.** Examples of normalised spectra of the spectral sequence of stars investigated here, arranged from hottest (top) to coolest (bottom). Displayed are three spectral windows, around H $\delta$  (left), He II  $\lambda$ 4686 Å (middle), and H $\alpha$  (right panel). The major spectral features are identified; the sharp absorption lines around H $\alpha$  are telluric H $_2$ O features.

**Table 2.** IUE spectra used for the study.

ID#	SW	Date YYYY-MM-DD	LW	Date YYYY-MM-DD
2	P08149	1980-03-03	R07080	1980-03-03
	P08150	1980-03-03	R08633	1980-08-27
	P09922	1980-08-27	...	...
5	P34159	1988-08-31	P13967	1988-08-31
6	P11156	1981-01-26	P27453	1994-02-20
	P50071	1994-02-20	R09788	1981-01-26
9	P04132	1979-02-03	R03662	1979-02-03
10	P20285	1983-06-22	R16208	1983-06-22
13	P06911	1979-10-19	R05873	1979-10-19
14	P14340	1981-06-26	P01510	1982-04-05
	P21795	1983-12-18	P01921	1983-06-28
	P22768	1984-04-16	P02426	1983-12-18
20	P08164	1980-03-04	P11155	1981-01-26
	R07097	1980-03-04	R09787	1981-01-26

show emission in H $\alpha$ . This stems either from a H II region, as in the case of BD –13 4930 – we also note the weak [N II] emission components there – or, as is the case for HD 57682 (Grunhut et al. 2009) and HD 54879 (Castro et al. 2015, their Fig. 9), from magnetically confined circumstellar gas.

Various (spectro-)photometric data were used in the present work in addition to the Echelle spectra. Low-dispersion, large-aperture spectra taken with the International Ultraviolet Explorer (IUE; Table 2) were downloaded from the Mikulski Archive for Space Telescopes (MAST<sup>3</sup>). The short-wavelength (SW) data cover the range  $\lambda$ 1150–1978 Å and the long-wavelength (LW) data  $\lambda$ 1851–3347 Å. For three stars (BD –13 4930, HD 34078, and HD 214680), spectra obtained by the *Hubble* Space Telescope’s (HST) Space Telescope Imaging Spectrograph (STIS) are on hand. The spectrophotometric data were co-added for further analysis in the cases where multiple IUE data were available for an object. Alternatively, UV photometric

data were considered, stemming either from the Astronomical Netherlands Satellite (ANS; Wesselius et al. 1982) or from the joint Belgian–UK Ultraviolet Sky Survey Telescope (Thompson et al. 1995) on board the European Space Research Organisation Thor-Delta satellite (TD1). Moreover, Johnson *UBV* magnitudes (Mermilliod 1997; Morel & Magnenat 1978), *JHK* magnitudes from the Two Micron All Sky Survey (2MASS; Cutri et al. 2003) and Wide-Field Infrared Survey Explorer (WISE) photometry (Cutri et al. 2021) were adopted.

**Rejected stars.** Despite the fact that we had pre-selected previously analysed stars for our sample, four objects (i.e. 20% of our initial sample) turned out to show second or even third light. Examples for the observational evidence are presented in Fig. 2.

HD 66788 (ID#1) shows extra broad absorption bluewards of the sharp He I/II lines of the main light source, apparently due to a faster-rotating later O- or early B-type star. As the vast majority of massive stars are found in multiple systems (Sana et al. 2012; Chini et al. 2012), this can be viewed as the first indication that the star is a candidate physical binary and requires further investigation. The spectral signature is more difficult to identify in the Balmer lines, but is visible in H $\alpha$  to the trained eye, and it vanishes in the continuum noise for metal lines. A similar signature is present in a FEROS spectrum taken about 5 yrs earlier, which Marcolino et al. (2009) analysed under the assumption that HD 66788 is a single star.

HD 37061 (NU Ori, ID#3) is the ionising star of the H II region M 43 close to the Orion nebula, which was studied in detail on the basis that it is single by Simón-Díaz et al. (2011) based on spectra at  $R \approx 7500$ –8000. It is in fact a triple system (see Fig. 2 for the comparison of two spectra taken at different times). A very detailed and conclusive study of the triple system by Shultz et al. (2019) came to our attention only later.

HD 46966 (ID#12) was analysed as a single star in several studies (e.g. Martins et al. 2012, 2015a; Holgado et al. 2018; Carneiro et al. 2019) so far. However, the spectrum shows a consistent pattern of ‘spiky’ cores best viewed in several metal lines

<sup>3</sup> <https://archive.stsci.edu/iue/>

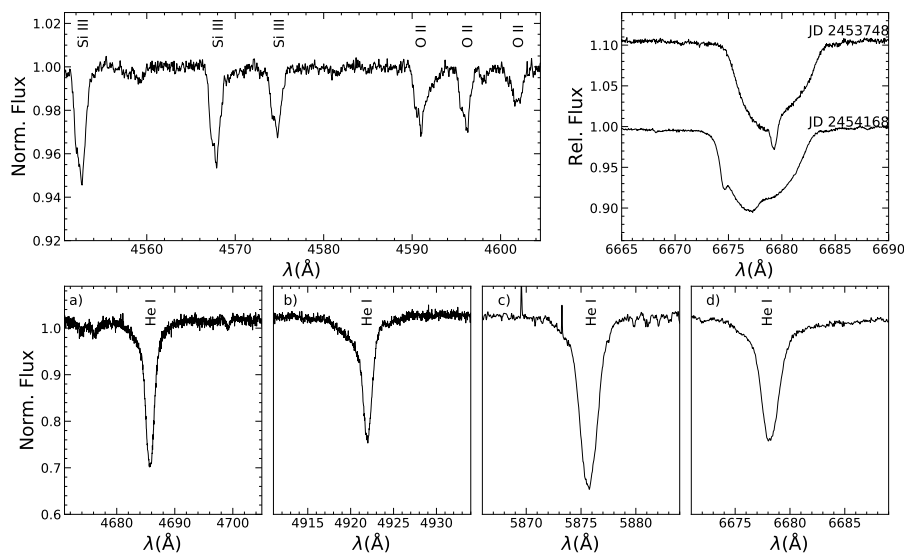


**Fig. 2.** Examples of stars rejected for further analysis in this work, based on spectral features. The metal lines in the spectrum of HD 46966 (top-left panel) show a systematic double-peak structure. The spectrum of HD 37061 (top-right panel) has three distinct components, which change position in wavelength with time. The helium lines in HD 66788 (bottom panels a and b) and HD 155889 (bottom panels c and d) show asymmetric line profiles, indicating a second line component in the blue wings. We note that He I  $\lambda 4922$  Å is asymmetric because of a forbidden component in the blue wing, but the observed extended blue wing in panel (b) is wider than expected if the star were to be single.

(see Fig. 2). We suggest that this may be the spectroscopic signature of a companion, with both stars being viewed nearly pole-on, which may explain the sharp lines. This would be consistent with the finding of a constant radial velocity by Chini et al. (2012). The ‘spikes’ are also unlikely to be a signature of some low-order non-radial pulsations, as only a red noise component was found in the variable photometry measured by the Convection, Rotation et Transits planétaires mission (CoRoT; Blomme et al. 2011). More recently, a resolved companion 50 mas away and fainter by  $\Delta H = 1.1$  mag was found by Sana et al. (2014) at near-IR wavelengths and confirmed by Aldoretta et al. (2015) using a broad optical filter with the Fine Guidance Sensors on board the HST, with  $\Delta m_{F5ND} \approx 1.1$  mag. With such a brightness difference and little colour difference, one would indeed expect to see a second line system in the spectrum, as suggested above. HD 155889 (ID#15) shows extra blue absorption, best seen in the red He I lines (see Fig. 2). This indicates the presence of a slightly cooler, faster-rotating companion. Indeed, Sota et al. (2014) note a double-lined SB2 nature for the object, but without giving further details. The Washington Double Star Catalog lists a companion with a separation of  $0.2''$  at  $\Delta m \approx 0.6$  mag (Mason et al. 2001), which appears compatible with the origin of the second line system in the spectrum.

The four stars were consequently removed from further analysis in the present work, as the basic assumptions of our analysis methodology are valid for single stars only. We note that our methodology can be extended to treat composite spectra (see e.g. Irrgang et al. 2014; González et al. 2017, 2019), but this is beyond the scope of the present work.

In addition, HD 14633 (ID#2) was resolved into two sources by Aldoretta et al. (2015) using the HST, finding a distance of  $\sim 20$  mas at  $\Delta m_{F5ND} \approx 1.6 \pm 1.1$  mag. We do not see an indication for the presence of second light in the available spectrum, but any signature could easily hide within the rotationally broadened spectral lines. However, it may be negligible, in particular if the companion is at the fainter end of the magnitude difference range. We kept the star in the analysed sample but note that for many of the stellar parameters and abundances we found larger uncertainties than for most of the other sample objects. Aldoretta et al. (2015) also found a close companion to HD 46202, at a distance of  $\sim 87$  mas and  $\Delta m_{F583W} = 2.166 \pm 0.008$  mag. As we do not see a second line system in the spectrum, we keep the star in the analysed sample.

### 3. Model atmospheres and spectrum synthesis

#### 3.1. Models and programs

Our analysis methodology applied to the interpretation of the weak-wind O-star spectra is based on a hybrid non-LTE approach, a non-LTE spectral synthesis is performed on LTE model atmospheres. The LTE atmospheres were computed with the ATLAS9 and ATLAS12 codes (Kurucz 1993, 2005), where the former was mostly used to compute starting models for the latter. Both codes assume plane-parallel geometry, hydrostatic, radiative and LTE, stationarity and chemical homogeneity. Line blanketing is realised via consideration of pre-tabulated opacity distribution functions (ODFs) in ATLAS9, whereas ATLAS12 employs opacity sampling (OS), which provides flexibility in the chemical composition. ATLAS12 also allows the effects of turbulent pressure on the atmospheric stratification to be accounted for, by considering it as an extra term in the hydrostatic equation.

The non-LTE computations were conducted with DETAIL and SURFACE (Giddings 1981; Butler & Giddings 1985). In a first step, the radiative transfer equation together with the rate equations were solved with DETAIL for the LTE atmospheric structure computed with ATLAS12, using an accelerated lambda iteration scheme by Rybicki & Hummer (1991) and considering line blocking based on the Kurucz OS scheme (with the exception of the calculations for hydrogen and helium, where the opacity averaging via ODFs is required to avoid the He I singlet problem, Nieva & Przybilla 2007). State-of-the-art model atoms were adopted according to Table 3, in which the ions considered per element, the number of explicit terms (plus superlevels) and radiative bound-bound transitions, and references are given. All model atoms are completed by the ground term of the next higher ionisation stage.

While most of the model atoms were used previously in various studies, a new model atom for O II/III was employed here – replacing the previously used O II model atom of Becker & Butler (1988) –, a brief summary is given in the following. Level energies were adopted from Martin et al. (1993) for O II and from Moore (1993) for O III. These were combined into 176 LS-coupled (Russell-Saunders coupling) terms up to principal quantum number  $n=8$  and the levels for  $n=9$  combined into two superlevels, one each for the doublet and quartet spin systems of O II. For O III this resulted in 132 terms up to  $n=6$  and 2 superlevels combining the levels for  $n=7$  for the singlet

**Table 3.** Model atoms for non-LTE calculations with DETAIL.

Ion	Terms	Transitions	Reference
H	20	190	[1]
He I/II	29+6/20	162/190	[2]
C II/III/IV	68/70/53	425/373/319	[3]
N II	77	462	[4]
O II/III	176+2/132+2	2559/1515	[5]
Ne II	78	992	[6]
Mg II	37	236	[7]
Al III	46+1	272	[8]
Si III/IV	68+4/33+2	572/242	[9]

**Notes.** Data for different ionisation stages are separated by a slash. If present, the number of superlevels is indicated after a plus sign.

**References.** [1] Przybilla & Butler (2004); [2] Przybilla (2005); [3] Nieva & Przybilla (2006, 2008); [4] Przybilla & Butler (2001); [5] Przybilla & Butler (in prep.); [6] Morel & Butler (2008); [7] Przybilla et al. (2001a); [8] Przybilla (in prep.); [9] Przybilla & Butler (in prep.).

and triplet spin systems. Oscillator strengths and photoionisation cross-sections were for the most part adopted from the Opacity Project (OP; e.g. Seaton et al. 1994), with several improved data taken from Froese Fischer & Tachiev (2004). The strongest resonance lines with broad line wings were treated as fine-structure transitions, accounting for Stark broadening using broadening coefficients from Kurucz<sup>4</sup>. Photoionisation cross-sections missing in the OP data were assumed to be hydrogenic. Electron impact-excitation data for a large number of transitions were available from the ab initio calculations of Tayal (2007, 80 transitions) and Mao et al. (2020, 3748 transitions) for O II and from Tayal & Zatsarinny (2017, 2346 transitions) for O III. Missing data were provided by the use of van Regemorter’s formula (van Regemorter 1962) for radiatively permitted transitions or Allen’s formula (Allen 1973) for forbidden transitions. All collisional ionisation data were provided via the Seaton formula (Seaton 1962) using OP photoionisation threshold cross-sections, or hydrogenic values.

Then, synthetic spectra were calculated with SURFACE using the non-LTE occupation numbers provided by DETAIL, considering both refined fine-structure transition data and line-broadening data. Oscillator strengths from Wiese et al. (1996) and recent data from Kurucz were replaced by multi-configuration Hartree-Fock data by Froese Fischer & Tachiev (2004) for O II/III (as for other elements and ions, also accounting for data from Froese Fischer et al. 2006), which was essential to achieve a close match between observations and model spectra. Both DETAIL and SURFACE were updated recently to account for level dissolution of H I and He II using the implementation of Hubeny et al. (1994), which yields a better modelling of the series limits. The spectrum synthesis for hydrogen and neutral helium was further updated by Stark-broadening tables of Tremblay & Bergeron (2009) and Beauchamp et al. (1997), respectively. For atmospheric parameters not covered by these tables, broadening data by Dimitrijevic & Sahal-Brechot (1990) were employed instead.

For the first (coarse) step of the analysis a grid ranging from 31 000 to 35 000 K in effective temperature (step size 1000 K), 3.8 to 4.3 in logarithm of gravity (step size 0.1), 2 to 16 km s<sup>-1</sup> in microturbulent velocity (step size 2 km s<sup>-1</sup>), and 0.07 to 0.13 in helium abundance by number (step size 0.02) was calculated and used to determine initial solutions. The boundaries are selected to contain typical literature values for late O-type dwarfs.

Then, smaller micro-grids with half the step size and elemental abundance steps of 0.1 dex were computed per star and further iteration steps were made to refine the analysis.

The individual line analyses were performed with the Spectral Plotting and Analysis Suite (SPAS; Hirsch 2009). The program allows instrumental, (radial-tangential) macroturbulent and rotational broadening to be applied flexibly to the synthetic spectra and can be used to fit up to three different parameters, interpolating on the pre-calculated grids to the actual parameters, using bi-cubic spline fitting. SPAS employs the downhill simplex algorithm (Nelder & Mead 1965) to find minima in the  $\chi^2$  landscape.

### 3.2. Comparison with hydrostatic full non-LTE models

The comparison between our hybrid and a full non-LTE approach for the hydrostatic case was already made by Nieva & Przybilla (2007, see their Sect. 5 for a comprehensive discussion), for parameters also relevant to the present work. In summary, they found that atmospheric structures computed with ATLAS and TLUSTY (as adopted from the OSTAR2002 grid; Lanz & Hubeny 2003) show excellent agreement in the effective temperature range from below 32 500 to 35 000 K. Deviations in the temperature structures amount to less than 1% in the inner atmosphere, which includes the formation regions of the weaker lines and the wings of the stronger features, and increase to 2–3% for the formation regions of the cores of most of the H and He lines. Stronger deviations occur only in the outermost parts of the atmospheres, which, however, are modified by the hydrodynamic outflow even in the weak wind case (this includes the formation region of the H $\alpha$  core and some metal resonance lines in the UV). Spectral energy distributions (SEDs) computed with ATLAS+DETAIL and TLUSTY also agree well, with some small differences occurring at the He II continua in the extreme UV. Hydrogen and helium lines computed with DETAIL+SURFACE on either ATLAS or TLUSTY atmospheric structures show excellent agreement, while the original line profiles from the OSTAR2002 grid showed the He I singlet problem. The small deviations compared to the hydrostatic full non-LTE models come with the advantage of significantly reduced computation time. Because of that, more complex model atoms can be employed, tailored model grids for each analysed star including variations of microturbulent velocities can be computed, and the uncertainties introduced by the grid spacing can be reduced. Our hybrid non-LTE method is applied systematically to a sample of weak-wind late O-type main-sequence stars for the first time.

### 3.3. Comparison with unified non-LTE atmospheres

A comparison of the atmospheric structures computed with ATLAS12 in LTE and the unified (photosphere + wind) non-LTE code FASTWIND (Santolaya-Rey et al. 1997; Puls et al. 2005) is shown in Fig. 3. The atmospheric and wind parameters were chosen according to the model of Martins et al. (2005) for HD 38666, which are representative for the sample stars. Two wind solutions were considered, for the wind mass-loss prescription of Vink et al. (2000) and for the observed weak wind with a mass-loss rate reduced by about two orders of magnitude. Both solutions are practically identical for the deepest atmospheric layers. Temperatures differ by about 1% in the regions where the weak (metal) line spectrum is formed, and the difference increases to ~2–3% at the formation depths of the cores of the stronger lines (most hydrogen Balmer and the He I lines), with the LTE solution showing higher temperatures. The temperature

<sup>4</sup> <http://kurucz.harvard.edu/atoms.html>

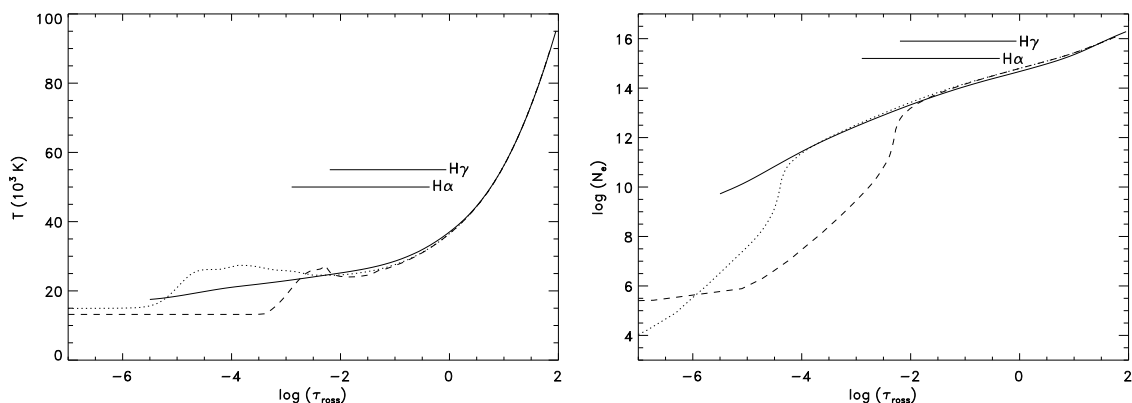


**Fig. 3.** Comparison of ATLAS12 (full line) and FASTWIND model atmospheres for an effective temperature of 33 000 K, surface gravity 4.0, microturbulent velocity 5 km s<sup>-1</sup>, and solar metallicity. *Left panel:* Temperature structure. *Right panel:* Electron density structure as a function of Rosseland optical depth,  $\tau_{\text{ross}}$ . The two FASTWIND models were computed for the parameters stellar radius  $R = 6.58 R_{\odot}$ , wind terminal velocity  $v_{\infty} = 1200$  km s<sup>-1</sup>,  $\beta$ -velocity-field parameter  $\beta = 1.0$ , and mass-loss rates  $\log \dot{M} (M_{\odot} \text{ yr}^{-1}) = -9.5$  (weak wind, dotted line) and  $\log \dot{M} (M_{\odot} \text{ yr}^{-1}) = -7.41$  (wind mass-loss rate according to Vink et al. 2000, dashed line). Formation depths for the Balmer H $\alpha$  and H $\gamma$  lines are indicated.

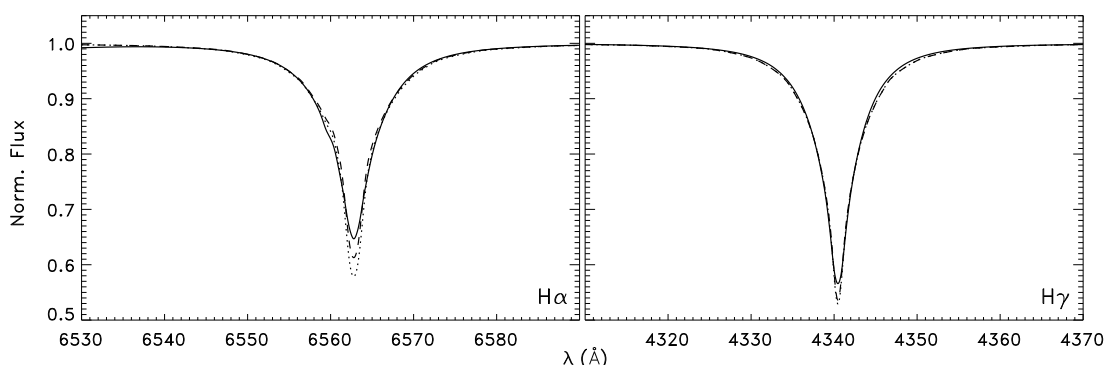


**Fig. 4.** Comparison of Balmer line profiles computed with ATLAS12-DETAIL-SURFACE and FASTWIND. *Left panel:* H $\alpha$ . *Right panel:* H $\gamma$ . The line coding is as in Fig. 3. All models were convolved with a rotational profile corresponding to  $v_{\text{rot}} = 30$  km s<sup>-1</sup>.

rise of the unified models at lower optical depths is seen only by the strongest lines in the optical, like H $\alpha$ .

The effect of the wind strength is more pronounced in the density structure, represented here by the electron density. Overall, the run of electron density with Rosseland optical depth  $\tau_{\text{ross}}$  agrees rather well between the weak-wind FASTWIND and the ATLAS12 model, with the former showing the onset of the wind at  $\log \tau_{\text{ross}} \approx -4$ . The higher mass-loss rate on the other hand would shift the onset of the wind to  $\log \tau_{\text{ross}} \approx -2$ , well within the formation region of H $\alpha$ .

Model profiles for H $\alpha$  and H $\gamma$  (including the He II blends) for the three atmospheric stratifications are shown in Fig. 4. Significant differences occur essentially only in the line cores. The H $\alpha$  line core of the solution with a higher mass-loss rate is shallower than in the weak-wind solution because of the density drop that sets in deeper in the atmosphere. On the other hand, the even shallower profile of the hydrostatic hybrid non-LTE solution results from the higher local temperature at core formation depths. The H $\gamma$  line shows close agreement. Similar agreement between the three models is found for the He I lines, while the He II lines are stronger in the hybrid non-LTE solution, reflecting the local temperature being higher by several hundred degrees (which can be seen by the effect on the He II blend to the blue wing of H $\alpha$  in Fig. 4). We conclude that the use of our hydrostatic hybrid non-LTE approach overall reproduces solutions of unified non-LTE models for the parameter range investigated here.

### 3.4. Turbulent pressure

Their location close to the Eddington limit makes O-type stars susceptible to additional factors that impact the delicate balance between the counteracting gravitational and radiative acceleration. One of these may be turbulent motions (microturbulence) that give rise to ‘turbulent pressure’  $P_{\text{turb}} = \frac{1}{2} \rho \xi^2$ , with  $\rho$  being the gas density and  $\xi$  the microturbulent velocity. The main effect will be on the pressure stratification, and one may expect an increased importance of this the closer the star is to the Eddington limit, and the larger the microturbulent velocity. ATLAS12 allows the effects of turbulent pressure on the model atmosphere computations to be taken into account by adding the above term to the hydrostatic equation.

In the following we investigate the effects of turbulent pressure on the atmospheric structure and synthetic spectra by comparing model calculations with and without the extra term at otherwise unchanged parameters. The model for BD +57 247 was chosen as the star shows one of the lower gravity values and the highest microturbulence of the entire sample, so it is to be expected that the effects will be the greatest of the sample stars.

A comparison of the resulting temperature and electron density stratifications as a function of Rosseland optical depth  $\tau_{\text{ross}}$  is shown in Fig. 5. Differences in temperature are negligible, as they amount to less than 100 K at line-formation depths. More pronounced are the differences in electron density, which are locally lower in the case where turbulent pressure is accounted for. This has a small but noticeable effect on the Stark broadening of



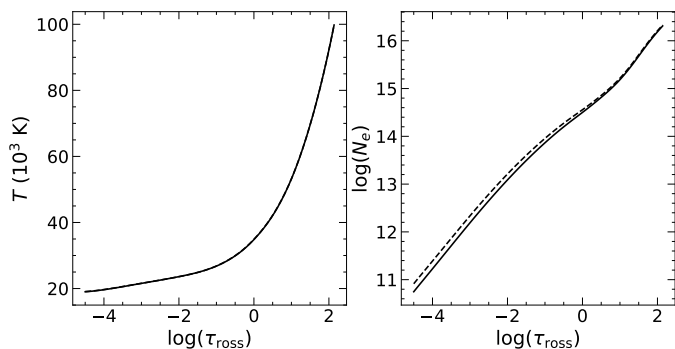


**Fig. 5.** Effects of turbulent pressure on the atmospheric structure in terms of temperature (*left*) and electron number density (*right panel*) as a function of  $\tau_{\text{Ross}}$ . The solid line shows the model that includes turbulent pressure, and the dashed line is for the same model without turbulent pressure. Atmospheric parameters for BD +57 247 were used for the comparison, with  $T_{\text{eff}} = 31\,200$  K,  $\log g = 3.87$ , and  $\xi = 16$  km s $^{-1}$ .

the hydrogen lines (see Fig. 6). While the higher gravity values derived in the case of calculations with turbulent pressure, by  $\leq 0.05$  dex, lie within the uncertainties of the spectral analysis, the effect is systematic. The cores of the helium and some metal lines are affected, with some lines being strengthened and others being weakened. The effects may appear small in Fig. 6, but, in particular, the change of equivalent width of the Si III triplet lines by 20% for the strongest multiplet line and gradually slightly less for the weaker multiplet members is highly significant in this case, as the triplet lies at the heart of many quantitative analyses, like the Very Large Telescope Fibre Large Array Multi Element Spectrograph (VLT-FLAMES) massive star survey (e.g. Hunter et al. 2007) or the VLT-FLAMES Tarantula Survey (e.g. Garland et al. 2017). Not only the ionisation balance of Si III/IV is shifted, but the microturbulence determination may also be affected. Numerous other lines show similar effects. However, the effects of microturbulent pressure will be smaller for the majority of the sample stars, because of the typically smaller microturbulent velocities (we note that often much higher values are stated in the literature), but this may change if weak-wind late O-type giants are investigated, or supergiants.

The consideration of the effects of turbulent pressure may also be important for the outer density structure of hydrodynamic models, where a depth-dependent microturbulent velocity is sometimes considered that increases from subsonic values in the photosphere (i.e. comparable to the cases here) up to one-tenth of the wind terminal velocity (Martins et al. 2015a), reaching microturbulent velocities beyond 200 km s $^{-1}$  for a typical late O-type dwarf star.

## 4. Spectral analysis

### 4.1. Stellar parameter and abundance determination

In a first step, the atmospheric parameters effective temperature  $T_{\text{eff}}$ , surface gravity  $\log(g)$  (in cgs units), the microturbulent velocity  $\xi$  and helium abundance by number  $y$ , as well as the projected rotational velocity  $v \sin i$  and macroturbulent velocity  $\zeta$  were constrained by as many spectral indicators as possible. An iterative approach was employed for this in order to overcome ambiguities because of correlations between some parameters until all parameters were constrained in a consistent way. In a second step, the various non-LTE elemental abundances  $\varepsilon(X) = \log(X/H) + 12$  for elements  $X$  were derived.

#### 4.1.1. Effective temperature and surface gravity

The sample stars cover a relatively small region in the  $T_{\text{eff}}$ - and  $\log g$ -parameter space because of the concentration on O8 to O9.7 spectral types and luminosity classes V and IV. Overall, the sample stars can be expected to fall in the range of 31 000 to 35 000 K in  $T_{\text{eff}}$  and 4.3 (about the value of the zero-age main sequence) to 3.8 in  $\log g$ . Ionisation equilibria of He I/II, C II/III/IV, O II/III, and Si III/IV (i.e.  $T_{\text{eff}}$  was adjusted so that lines from the different ionisation stages of an element indicate the same abundance at a given value of  $\log g$ ) were established as temperature indicators. The surface gravity was adjusted such that the Stark-broadened wings of the Balmer lines were reproduced at a given  $T_{\text{eff}}$ . The adopted combination of  $T_{\text{eff}}/\log g$  is given by the values where all indicators match the observations simultaneously. In principle, additional ionisation equilibria are available from the optical spectra, for example N II/III. However, we lack a reliable model atom for the latter ionisation stage.

#### 4.1.2. Microturbulence and elemental abundances

The microturbulent velocity was adjusted so that the element abundance of individual lines in the spectral fitting became independent of the strengths of the lines (for visualisation purposes, equivalent widths of these lines were measured). The main indicators were the carbon and silicon lines. Closely related to this was the determination of the elemental abundances. Helium plays a particular role because of its larger mean molecular weight, which may modify the atmospheric pressure stratification depending on the helium abundance. For a given set of atmospheric parameters, we calculated a small grid of synthetic spectra for an element and fitted individual line profiles employing SPAS, aiming at  $\chi^2$  minimisation. The final abundance values and their uncertainties were computed once all atmospheric parameters were fixed in the iterative process, as the statistical mean and its  $1\sigma$  standard deviation, based on all considered lines (marked outliers were removed using  $\sigma$ -clipping).

#### 4.1.3. Projected rotational velocity and macroturbulence

Both parameters were derived simultaneously by fitting the profiles of numerous metal lines. The synthetic lines were broadened with rotational and a radial-tangential macroturbulence profiles (Gray 2005) and a Gaussian instrumental profile as appropriate for the resolving power of the three instruments. The necessity for considering non-rotational broadening in O-type stars is well established (e.g. Simón-Díaz et al. 2017). Atmospheric velocity fields due to a sub-surface convection zone and stellar pulsations, among others, are the phenomena that are summarised by the macroturbulence parameter. To account for the line depth the elemental abundance was included as a third fit parameter to achieve an optimum fit of each line.

#### 4.1.4. SED fitting

A comparison of the model SED with observations allows one to test whether the derived solution also reproduces the global energy output of a star. The observed SEDs were constructed from HST or IUE spectrophotometry, or ANS or TD1 UV photometry, and Johnson, 2MASS and WISE photometry. On the model side, the starting ATLAS9 model fluxes were adopted, as they are directly usable for the comparison with the low-resolution observations without any further processing. They are equivalent to ATLAS12 models for the purpose of SED fitting because the



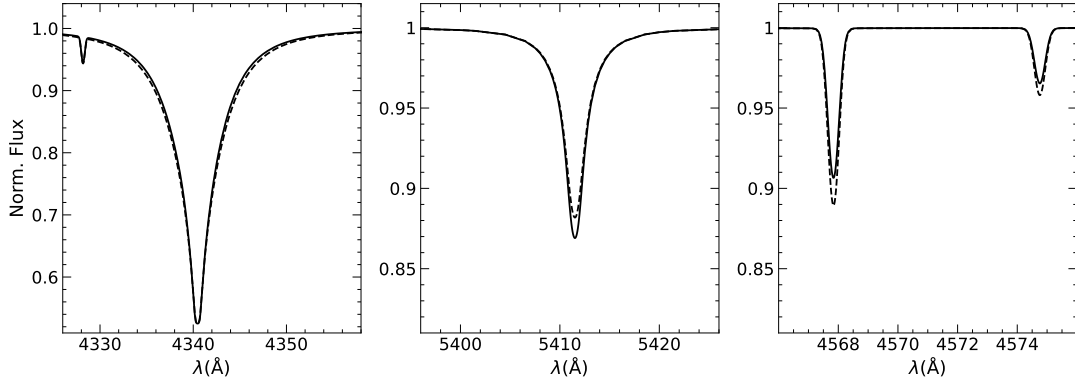


**Fig. 6.** Effects of turbulent pressure on the line profiles of H $\gamma$  (left), He II  $\lambda 5411$  Å (centre), and two of the Si III triplet lines (right panel). The solid line shows the model that includes turbulent pressure, and the dashed line is for the same model without turbulent pressure.

temperature structures are practically identical for nearly scaled-solar abundances (as is the case here). To account for interstellar extinction the reddening law of Fitzpatrick (1999) was used, parameterised by the colour excess  $E(B - V)$  and the ratio of total-to-selective extinction  $R_V = A_V/E(B - V)$ . To obtain both parameters the model SEDs were matched to the observations. Synthetic magnitudes were computed by integrating the model flux over the normalised transmission profile of each filter, applying zero points in the Vega system, and then reddened. The transmission profiles and zero-points were taken from the SVO Filter Profile Service<sup>5</sup> (Rodrigo et al. 2012; Rodrigo & Solano 2020).

The bolometric corrections  $B.C. = \bar{m}_{\text{bol}} - \bar{m}_V$  were obtained via synthetic magnitudes (marked by barred variables). The zero point for the synthetic bolometric magnitude was chosen such that the absolute bolometric magnitude of the Sun,  $M_{\text{bol},\odot} = 4.74$ , was reproduced when using an ATLAS9 model atmosphere for solar parameters.

#### 4.2. Spectroscopic distances

The stellar flux measured at Earth  $f_\lambda = F_\lambda \cdot (\pi R^2/d^2)$  depends on the astrophysical flux emitted at the surface of the star,  $F_\lambda$ , the distance to the star,  $d$ , and the stellar radius,  $R$ . The measurement of the magnitude  $m_X$  with a filter with normalised transmission profile  $T(\lambda)$  can be expressed as

$$\begin{aligned} m_X &= -2.5 \log \left( \int f_\lambda T(\lambda) d\lambda \right) + zp \\ &= -2.5 \log \left( \int F_\lambda T(\lambda) d\lambda \right) + zp - 2.5 \log(\pi R^2/d^2), \end{aligned} \quad (1)$$

with  $zp$  being the zero point of the given filter  $X$ .

Expressing the stellar radius in terms of the stellar mass  $M$  and surface gravity  $\log(g)$  and using the definition for synthetic magnitudes one can solve Eq. (1) for the distance (in units of parsec). This distance depends on spectroscopically derived parameters and, hence, is called the spectroscopic distance:

$$d_{\text{spec}} = 6.63 \cdot 10^{-6} \sqrt{M/M_\odot \cdot 10^{0.4(m_X - \bar{m}_X) - \log(g)}} \text{ pc}. \quad (2)$$

In Eq. (2) the stellar mass – which still needs to be determined – is given in solar units,  $m_X$  is the observed magnitude,  $\bar{m}_X$  the synthetic magnitude of the reddened SED (we use  $V$  magnitudes in the following) and  $\log(g)$  is given in cgs units.

<sup>5</sup> <http://svo2.cab.inta-csic.es/theory/fps/>

#### 4.3. Fundamental parameters

In a final step the fundamental stellar parameters were determined in analogy to previous work on early B-type stars (Nieva & Przybilla 2014). The stellar evolutionary masses  $M_{\text{evol}}$  were found by comparing the position of the stars in the spectroscopic Hertzsprung-Russell diagram (sHRD; Langer & Kudritzki 2014) relative to Geneva evolutionary tracks (Ekström et al. 2012). Non-rotating models were employed here, because the sample stars are (in most cases presumably true) slow rotators. Stellar radii were then derived from the definition of the surface gravity  $\log(g) = GM/R^2$  and the stellar luminosity followed directly from the Stefan-Boltzmann law  $L = 4\pi\sigma R^2 T_{\text{eff}}^4$ , with  $\sigma$  being the Stefan-Boltzmann constant. This also facilitated conversion to absolute bolometric magnitudes  $M_{\text{bol}}$  and, considering  $B.C.$ , to the absolute visual magnitude  $M_V$ . Evolutionary ages  $\tau_{\text{evol}}$  were finally derived in the Hertzsprung-Russell diagram (HRD) by comparison of the sample star positions with the loci of isochrones based on the Ekström et al. tracks for non-rotating stars.

#### 4.4. Limitations of the hybrid non-LTE approach

As our hybrid non-LTE approach is based on hydrostatic model atmospheres it faces limitations with respect to describing late O-type stars comprehensively. In particular, the phenomena associated with the hydrodynamical stellar wind outflow can obviously not be addressed. Wind parameters that require modelling, such as the mass-loss rate ( $\dot{M}$ ) or the wind velocity-law parameter ( $\beta$ ), cannot be constrained – though the wind terminal velocity ( $v_\infty$ ) can be empirically determined from the absorption troughs of the observed UV resonance lines. However, these parameters do not impact the photospheric layers in a significant way in the weak-wind case, so that the analysis of the photospheric spectrum remains unaffected.

Also, the generation of X-rays in wind-embedded shocks (see e.g. Carneiro et al. 2016; Puls et al. 2020) cannot be described within this framework. The soft X-ray and extreme-UV back-illumination of the photosphere can affect the ionisation balance there, such that the line formation of some particular spectral features may be impacted. In principle, photospheric lines connected to UV-transitions are affected, but the effects are dependent on the strength of the illumination. The impact of X-rays on the metal-line formation was studied only in the case of carbon so far (Carneiro et al. 2019), finding negligible effects in the  $T_{\text{eff}}$  range between 30 000 and 35 000 K both for dwarfs and

**Table 4.** Stellar parameters for the sample stars.

#	Name	$T_{\text{eff}}$ K	$\log(g)$ cgs	$y$	$\xi$ km s <sup>-1</sup>	$v \sin(i)$ km s <sup>-1</sup>	$\zeta$	$E(B-V)$ mag	$R_V$	$B.C.$ mag	$M_V$ mag	$M_{\text{bol}}$ mag	$M/M_{\odot}$	$R/R_{\odot}$	$\log L/L_{\odot}$	$\log \tau_{\text{evol}}$ yr	$d_{\text{Gaia}}^a$ pc	$d_{\text{spec}}$ pc
2	HD 14633	34000	3.90	0.088	6	125	74	0.09	2.80	-3.05	-4.67	-7.72	23.2	9.0	4.98	6.64	1482	2142
2a <sup>b</sup>		± 1000	0.10	0.008	2	5	18	0.02	0.10	0.07	0.22	0.21	1.3	1.2	0.08	0.07	<sup>159</sup> 131	253
		±									-3.74	-6.79	9.8	5.8	4.61	...		...
											0.32	0.32	3.0	1.1	0.13	...		...
4	HD 258691	33300	4.02	0.080	8	20	39	0.90	3.35	-3.08	-4.08	-7.16	19.9	7.2	4.76	6.63	1563	1433
5	HD 201345	± 500	0.05	0.007	2	6	8	0.04	0.20	0.04	0.10	0.09	0.4	0.5	0.04	0.07	<sup>290</sup> 212	84
		32000	3.80	0.089	12	91	61	0.18	2.70	-2.97	-4.66	-7.63	21.7	9.7	4.95	6.72	1918	2328
		± 500	0.10	0.007	2	2	10	0.02	0.10	0.04	0.28	0.28	1.8	1.6	0.11	0.02	<sup>147</sup> 128	284
5a <sup>b</sup>		±									-4.27	-7.21	14.7	8.0	4.78	...		...
											0.32	0.32	4.0	1.5	0.13	...		...
6	HD 57682	33500	3.93	0.082	4	10	33	0.12	3.10	-3.11	-4.40	-7.51	21.7	8.4	4.90	6.65	1115	1228
7	HD 227757	± 800	0.05	0.012	2	1	4	0.02	0.10	0.06	0.11	0.09	0.8	0.5	0.04	0.04	<sup>100</sup> 85	74
		33300	4.04	0.094	8	17	31	0.51	3.10	-3.08	-4.02	-7.10	19.6	7.0	4.73	6.61	2080	2141
		± 400	0.08	0.008	2	4	4	0.02	0.10	0.03	0.20	0.20	0.7	0.8	0.08	0.14	<sup>62</sup> 59	201
8	BD -13 4930	32900	4.14	0.093	6	8	23	0.55	3.30	-3.07	-3.63	-6.70	18.0	6.0	4.58	6.49	1664	1786
9	BD +60 499	± 300	0.05	0.007	2	2	4	0.02	0.10	0.02	0.10	0.10	0.2	0.4	0.04	0.17	<sup>52</sup> 49	104
		33800	4.09	0.092	6	19	34	0.83	3.25	-3.13	-3.91	-7.04	19.7	6.6	4.71	6.53	2052	2023
		± 300	0.05	0.007	2	2	2	0.02	0.10	0.02	0.11	0.11	0.3	0.4	0.04	0.11	<sup>63</sup> 59	118
10	BD +57 247	31200	3.87	0.096	16	16	31	0.63	2.51	-2.91	-4.30	-7.21	19.0	8.4	4.78	6.76	3469	3403
11	HD 207538	± 500	0.05	0.010	2	1	5	0.02	0.10	0.04	0.11	0.10	0.5	0.6	0.04	0.03	<sup>234</sup> 206	200
		31400	3.93	0.089	8	32	42	0.62	2.70	-2.94	-4.12	-7.05	18.4	7.7	4.72	6.75	849	891
		± 500	0.05	0.006	2	3	3	0.02	0.10	0.04	0.10	0.09	0.4	0.5	0.04	0.03	<sup>12</sup> 12	52
13	HD 46202	33900	4.16	0.080	6	11	33	0.55	3.00	-3.14	-3.71	-6.85	19.2	6.0	4.64	6.38	1411	1130
14	HD 38666	± 500	0.05	0.008	2	1	4	0.02	0.10	0.04	0.09	0.08	0.4	0.3	0.03	0.23	<sup>273</sup> 197	66
		33400	4.12	0.096	8	125	42	0.04	3.10	-3.09	-3.78	-6.87	18.9	6.3	4.64	6.49	587	581
		± 300	0.05	0.007	2	8	10	0.02	0.10	0.02	0.11	0.11	0.3	0.4	0.04	0.15	<sup>33</sup> 29	34
16	HD 54879	32200	4.06	0.086	4	0	0	0.36	3.10	-3.02	-3.78	-6.80	17.8	6.5	4.62	6.65	1252	1149
17	HD 214680	± 700	0.05	0.008	2	1	1	0.02	0.10	0.05	0.10	0.09	0.6	0.3	0.03	0.10	<sup>57</sup> 52	69
		34550	4.04	0.083	5	14	32	0.11	3.10	-3.19	-4.17	-7.36	21.6	7.4	4.84	6.55	456	552
		± 300	0.05	0.009	2	1	2	0.02	0.10	0.02	0.12	0.12	0.5	0.5	0.05	0.08	<sup>29</sup> 26	32
18	HD 34078	33200	4.06	0.085	8	9	23	0.56	3.20	-3.08	-3.93	-7.01	19.2	6.8	4.70	6.60	389	418
19	HD 206183	± 300	0.05	0.008	2	2	3	0.02	0.10	0.02	0.11	0.11	0.3	0.5	0.04	0.08	<sup>5</sup> 5	24
		33100	4.06	0.085	4	4	21	0.45	3.10	-3.08	-3.91	-6.99	19.1	6.8	4.69	6.60	921	970
		± 300	0.05	0.006	2	2	4	0.02	0.10	0.02	0.11	0.11	0.3	0.5	0.04	0.08	<sup>16</sup> 16	57
20	HD 36512	32900	4.20	0.087	7	8	26	0.05	3.10	-3.07	-3.45	-6.52	17.5	5.5	4.51	6.29	407	386
		± 600	0.05	0.006	2	4	4	0.02	0.10	0.04	0.09	0.08	0.5	0.3	0.03	0.37	<sup>25</sup> 22	23

**Notes.** Uncertainties are  $1\sigma$  values. <sup>(a)</sup> [Gaia Collaboration et al. \(2016, 2021\)](#), distances and uncertainties correspond to inverted EDR3 parallaxes.

<sup>(b)</sup> Alternative solution, adopting the *Gaia* distance instead of the spectroscopic distance. See Sect. 5 for details.

supergiants, a situation that changes above a  $T_{\text{eff}}$  of 40 000 K. We assume that other metals may follow this behaviour, which, however, should be verified by studies similar to that of [Carneiro et al. \(2019\)](#).

Overall, it appears that no serious limitations for meaningful analyses based on a hydrostatic hybrid non-LTE approach exist for the photospheric spectra of weak-wind late O-type stars. This may not only apply to the dwarfs and sub-giants investigated here, but may also be extended to giant stars later than O8 at  $\log L/L_{\odot} \lesssim 5.2$  ([de Almeida et al. 2019](#)). These are expected to have stronger stellar winds, of the order  $10^{-9}$  to  $10^{-8} M_{\odot} \text{ yr}^{-1}$ , which, however, is still weaker than the ‘strong wind’ scenario discussed in Sect. 3.3, which had a negligible impact on the photospheric layers. Moreover, the hybrid non-LTE approach may be applicable at even higher temperatures for objects below the main sequence with insignificant stellar winds, such as for hot members of the sub-dwarf B (sdB) class (e.g. [Przybilla et al. 2006b](#)) and the hotter sub-dwarf O (sdO) stars ([Heber 2009, 2016](#)), to the point where non-LTE effects become non-negligible for the atmospheric structure calculations. This would require the provision of model atoms for more highly-ionised metal species than employed in the present work. On the other

hand, the hydrogen- or helium-only atmospheres of hot white dwarfs should be readily applicable, again up to the point where non-LTE effects become important for the atmospheric structure modelling.

## 5. Results

The results of the sample star analyses are summarised in Tables 4 and 5. The former lists the stellar parameters: the internal identification number is given, the HD designation, effective temperature, surface gravity, surface helium abundance (number fraction), microturbulent, projected rotational and macroturbulent velocity, colour excess, total-to-selective extinction parameter, bolometric correction, absolute visual and bolometric magnitude, evolutionary mass, radius, luminosity, evolutionary age, the *Gaia* EDR3 distance (from the inversion of the parallax) and the spectroscopic distance. The corresponding  $1\sigma$  uncertainties are given in the lines below the observed values. Table 5 concentrates on the elemental abundances: again, the internal identification number and the HD designation are given and abundance values for eight elements, plus the sum of the carbon, nitrogen and oxygen abundances and the stellar metallicity (by mass).

**Table 5.** Chemical abundances for the sample stars.

#	Name	log X/H+12									Z (by mass)
		He I/II	C II/III/IV	N II	O II/III	$\Sigma$ CNO	Ne II	Mg II	Al III	Si III/IV	
2	HD 14633	10.98 (13) $\pm 0.04$	7.64 (7) 0.14	8.46 (8) 0.11	8.29 (12) 0.05	8.72 0.15	8.07 (2) 0.05	7.55 (1) 0.05	6.50 (1) 0.10	7.41 (7) 0.11	0.010 0.001
4	HD 258691	10.94 (12) $\pm 0.04$	8.29 (4) 0.03	7.89 (10) 0.08	8.61 (20) 0.05	8.83 0.07	8.30 (8) 0.10	7.41 (3) 0.03	6.40 (3) 0.03	7.21 (10) 0.12	0.013 0.001
5	HD 201345	10.99 (14) $\pm 0.04$	7.74 (6) 0.09	8.54 (11) 0.09	8.56 (17) 0.12	8.88 0.16	8.32 (2) 0.05	7.52 (1) 0.03	6.50 (1) 0.10	7.50 (11) 0.10	0.014 0.001
6	HD 57682	10.95 (11) $\pm 0.07$	8.19 (13) 0.07	8.18 (9) 0.05	8.62 (35) 0.06	8.86 0.09	8.13 (8) 0.06	7.40 (3) 0.03	6.35 (3) 0.03	7.32 (13) 0.11	0.013 0.001
7	HD 227757	11.01 (15) $\pm 0.04$	8.50 (14) 0.07	8.14 (11) 0.08	8.83 (38) 0.09	9.05 0.13	8.30 (4) 0.04	7.65 (1) 0.05	6.60 (3) 0.03	7.58 (17) 0.09	0.018 0.002
8	BD −13 4930	11.01 (15) $\pm 0.03$	8.39 (15) 0.10	8.10 (11) 0.06	8.76 (38) 0.06	8.98 0.10	8.31 (5) 0.03	7.62 (2) 0.04	6.53 (3) 0.03	7.50 (13) 0.06	0.016 0.001
9	BD +60 499	11.01 (13) $\pm 0.04$	8.32 (16) 0.09	8.19 (6) 0.02	8.83 (39) 0.10	9.02 0.16	8.29 (4) 0.03	7.58 (3) 0.03	6.47 (3) 0.05	7.48 (16) 0.07	0.017 0.002
10	BD +57 247	11.02 (12) $\pm 0.05$	8.01 (15) 0.09	8.35 (12) 0.07	8.43 (9) 0.06	8.77 0.09	8.05 (3) 0.03	7.43 (3) 0.03	6.34 (3) 0.05	7.09 (7) 0.11	0.010 0.001
11	HD 207538	10.99 (13) $\pm 0.03$	8.19 (10) 0.08	8.21 (15) 0.06	8.63 (36) 0.06	8.87 0.09	8.21 (6) 0.05	7.57 (3) 0.03	6.47 (3) 0.05	7.36 (16) 0.13	0.013 0.001
13	HD 46202	10.94 (15) $\pm 0.05$	8.20 (11) 0.10	7.84 (8) 0.05	8.62 (34) 0.05	8.81 0.09	8.10 (7) 0.06	7.48 (1) 0.03	6.36 (3) 0.03	7.30 (12) 0.04	0.012 0.001
14	HD 38666	11.02 (13) $\pm 0.04$	8.50 (6) 0.04	8.25 (6) 0.15	8.82 (16) 0.04	9.06 0.08	8.27 (1) 0.03	7.58 (1) 0.03	6.58 (2) 0.05	7.45 (11) 0.10	0.017 0.001
16	HD 54879	10.97 (16) $\pm 0.04$	8.27 (13) 0.07	7.67 (10) 0.04	8.60 (38) 0.07	8.80 0.11	8.19 (7) 0.11	7.50 (3) 0.04	6.34 (5) 0.05	7.26 (15) 0.16	0.012 0.001
17	HD 214680	10.95 (9) $\pm 0.05$	8.36 (13) 0.07	8.11 (13) 0.08	8.77 (40) 0.06	8.98 0.10	8.24 (7) 0.07	7.59 (1) 0.03	6.50 (3) 0.03	7.48 (15) 0.10	0.016 0.001
18	HD 34078	10.97 (13) $\pm 0.05$	8.26 (12) 0.07	7.78 (12) 0.11	8.65 (35) 0.06	8.84 0.10	8.26 (8) 0.07	7.50 (3) 0.03	6.41 (3) 0.03	7.33 (16) 0.12	0.013 0.001
19	HD 206183	10.97 (13) $\pm 0.04$	8.26 (13) 0.09	7.89 (12) 0.08	8.60 (32) 0.06	8.82 0.10	8.20 (5) 0.03	7.41 (1) 0.03	6.28 (3) 0.03	7.29 (13) 0.08	0.012 0.001
20	HD 36512	10.98 (15) $\pm 0.03$	8.32 (17) 0.10	7.85 (12) 0.05	8.68 (41) 0.06	8.88 0.11	8.22 (7) 0.04	7.47 (1) 0.03	6.39 (3) 0.03	7.32 (15) 0.08	0.013 0.001
CAS <sup>a,b</sup>		10.99 $\pm 0.01$	8.35 0.04	7.79 0.04	8.76 0.05	8.93 0.08	8.09 0.05	7.56 0.05	6.30 0.07	7.50 0.06	0.014 0.002

**Notes.** Numbers in brackets denote the number of analysed spectral lines. Each spectral line was given the same weight for calculating the average. Abundance uncertainties are  $1\sigma$  standard deviations from the line-to-line scatter, not standard errors of the mean.

<sup>(a)</sup> Nieva & Przybilla (2012) <sup>(b)</sup> Przybilla et al. (2013)

The number of spectral lines for each ionisation stage employed for the analysis is indicated in brackets, and  $1\sigma$  standard deviations are given to characterise the uncertainties. For comparison, cosmic abundance standard (CAS) values as found from early B-type stars in the solar neighbourhood (Przybilla et al. 2008; Nieva & Przybilla 2012; Przybilla et al. 2013) are also tabulated.

### 5.1. Atmospheric and fundamental stellar parameters

Relative uncertainties in the stars' effective temperatures  $\delta T_{\text{eff}} = \Delta T_{\text{eff}}/T_{\text{eff}} \approx 1\text{--}3\%$  and uncertainties of  $\Delta \log g \approx 0.05$  to  $0.10$  dex in surface gravity are found in the present work. This is comparable to previous work on analyses of massive early-type main-sequence to supergiant stars using the ATLAS-DETAIL-SURFACE suite of codes (Przybilla et al. 2006a; Nieva & Przybilla 2012; Farnstein & Przybilla 2012; Weißmayer et al. 2022). Relative uncertainties of the helium abundances amount to  $\delta y \approx 7\text{--}15\%$  owing to the line-to-line scatter from the set of analysed He I lines.

The uncertainty of the microturbulent velocity is limited by the step size in the grid used for fitting, and so a conservative estimate of  $\Delta \xi \approx 2 \text{ km s}^{-1}$  was adopted throughout this study. The effects of projected rotational and macroturbulent velocity on the line profiles are interconnected. The relative uncertainties amount to from below  $10\%$  to several  $10\%$ . An exception

is the star HD 54879, which has an exceptionally low rotational velocity.

Another (weaker) ambiguity is found for the pair of colour excess and the total-to-selective extinction parameter. The fitting described in Sect. 4.1.4 produced uncertainties of  $\Delta E(B - V) \approx 0.02$  mag and  $\Delta R_V \approx 0.1$  in most cases. A  $\Delta B.C.$  of  $0.02$  to  $0.07$  mag was derived for the sample stars and the uncertainties in the absolute visual and bolometric magnitudes amount to  $0.1$  to  $0.2$  mag typically.

Values for evolved masses  $M_{\text{evol}}$  were derived based on zero-age main sequence (ZAMS) mass estimates, considering the mass lost during the main-sequence evolution by inspection of the evolution tracks of Ekström et al. (2012) (see our Sect. 5.7). The uncertainties of the evolved masses are assumed to be identical to the ZAMS mass uncertainty,  $\delta M_{\text{ZAMS}} = \delta M_{\text{evol}}$ , with values ranging between  $2$  and  $5\%$  typically. Radii show relative errors  $\delta R$  from  $5$  to slightly over  $10\%$  in most cases. Luminosity uncertainties amount to about  $10\text{--}20\%$  typically. Finally, the derived *Gaia* EDR3-based and the spectroscopic distances show a large range of relative uncertainties, from about  $1$  to  $20\%$ , with the *Gaia* values typically being the more precise.

For our two ON stars, HD 14633 and HD 201345, two solutions are given in Table 4. The solutions with IDs #2 and #5 were derived under the standard assumptions described above.



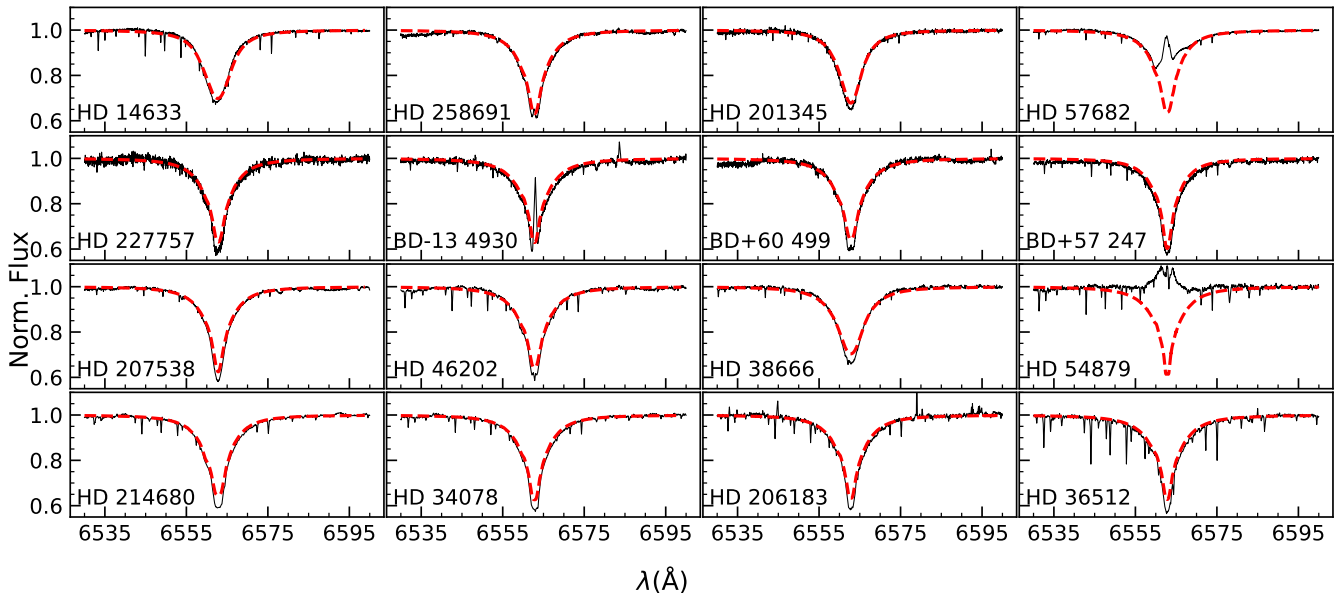


**Fig. 7.** Comparison of the observed spectra (black solid) and the global best fitting model (red dashed) of the  $H\alpha$  line for all analysed stars.

However, these two stars show notably discrepant spectroscopic and *Gaia* parallaxes. Assuming the *Gaia* distances and not the spectroscopic distances to be correct, one can redetermine the stars' absolute visual and bolometric magnitudes by adopting the *Gaia*-based distance modulus (the reddening values and bolometric corrections remain unaltered), and use Eq. 2 to solve for the masses (yielding larger relative mass uncertainties) and derive the other fundamental parameters. These are the alternative solutions #2a and #5a in Table 4. We note that all atmospheric parameters are unchanged for these alternative solutions and the age cannot be determined, because a different evolution scenario, possibly involving mass exchange in a close binary system, needs to be invoked, which is beyond the scope of the present paper (see Sect. 5.7 for further discussion).

The  $H\alpha$  line is the most sensitive spectral feature in the optical to effects of a stellar wind. A comparison of the global best fitting model based on the derived atmospheric parameters with the observed  $H\alpha$  profiles for all analysed sample stars is shown in Fig. 7. Good matches are obtained typically, except for the very cores. As implied by the comparison in Sect. 3.3, the cores are slightly too shallow, because of locally too high temperatures of the atmospheric models in the  $H\alpha$  line core formation region.

The peculiar  $H\alpha$  shapes of three sample stars are also understood. The star BD -13 4930 shows an emission feature in the line core that stems from a  $H\text{II}$  region (we also note the weak  $[\text{NII}]$  emission components). The emission in the spectrum of HD 57682 stems from magnetically confined circumstellar gas (Grunhut et al. 2009), and analogously in the case of HD 54879 (Castro et al. 2015).

## 5.2. Comparison with literature values

Several of our sample stars were analysed in previous studies. In order to compare our hybrid non-LTE approach with full non-LTE studies we discuss two cases as examples in this section, without aiming to achieve completeness with respect to the available literature (a few cases will be summarised in Sect. 6).

The first case we discuss are the atmospheric parameters of the O9 V standard star 10 Lac (HD 214680). Modern studies with line-blanketed hydrodynamic non-LTE atmospheres, such

**Table 6.** Comparison of atmospheric parameters for 10 Lac.

$T_{\text{eff}}$ (K)	$\log g$ (cgs)	$\xi$ (km s $^{-1}$ )	Reference
$35500 \pm 500$	$3.95 \pm 0.10$	$10^a$	Herrero et al. (2002)
$36000^{+800}_{-900}$	$4.03^{+0.13}_{-0.12}$	$15.5^{+4.1}_{-3.8}$	Mokiem et al. (2005)
$36000 \pm 1000$	$3.9 \pm 0.1$	$10^a$	Simón-Díaz et al. (2006)
$35000 \pm 1000$	$4.05 \pm 0.15$	$\geq 10^b$	Martins et al. (2015a)
$35200 \pm 500$	$3.89 \pm 0.05$	12	Holgado et al. (2018)
$34550 \pm 300$	$4.04 \pm 0.05$	$5 \pm 2$	this work

**Notes.** <sup>(a)</sup> adopted <sup>(b)</sup> adopted as 10 km s $^{-1}$  at the photosphere base and reaching 10% of the terminal velocity at the top of the atmosphere

as FASTWIND and CMFGEN, have converged on consistent values for  $T_{\text{eff}}$  and  $\log g$ , with values typically overlapping within the respective uncertainties, as summarised in Table 6. Microturbulent velocities  $\xi$  are often adopted in the literature, only sometimes determined. Our solution is only slightly cooler, indicates a gravity on the high side of the previous determinations and has a much smaller microturbulence, but we stress the excellent match of the synthetic with the observed spectrum (see Fig. B.1), the match of the SED fit, and the agreement of the spectroscopic with the Lac OB1b association distance (in the absence of a consistent parallax measurement), as discussed later. From this we can conclude that our approach produces an overall consistent result with solutions from full non-LTE modelling for this anchor of the MK system, though providing a significantly smaller microturbulent velocity. The modern  $T_{\text{eff}}$  values are about 2000 K cooler than derived from analyses based on pure H+He non-LTE model atmospheres in the past (for a discussion, see e.g. Herrero et al. 2002).

The second case is the comparison of the solutions for the many sample stars in common with the work of Martins et al. (2015a) and Holgado et al. (2018, 2022). This is visualised in Fig. 8. The agreement in effective temperature determinations (left panel) is very good with the Martins et al. data, with only one significant outlier (the ON star HD 201345), while the Holgado et al. results are shifted overall to higher  $T_{\text{eff}}$ . Our surface gravities are in many cases consistent with the Martins et al. results, though a small shift towards higher values should be

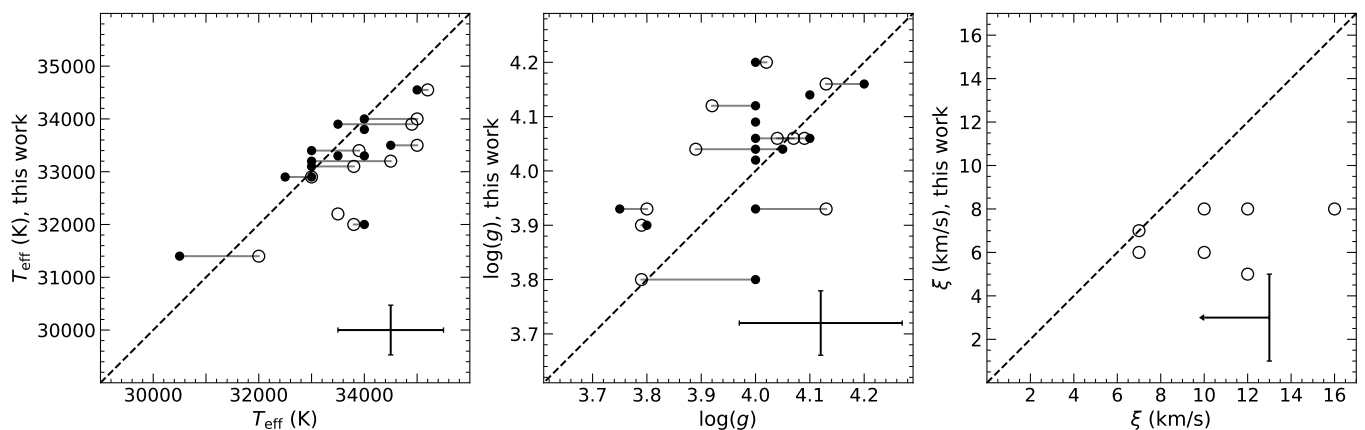


**Fig. 8.** Comparison of our  $T_{\text{eff}}$  (left),  $\log g$ -values (middle), and microturbulence (right panel) with data from Martins et al. (2015a,b, dots) and Holgado et al. (2018, 2022, circles). A uniform value of  $\xi = 10 \text{ km s}^{-1}$  was adopted for the photospheric layers of the stars in the Martins et al. work. Different literature results for the same star are connected by black lines. Typical error bars from the Martins et al. work are indicated in the left and middle panels; the uncertainties from Holgado et al. are slightly smaller, and for the microturbulent velocities they provide only upper limits in many cases.

noted (middle panel, again with the exception of HD 101345). The same trend is more pronounced compared with the Holgado et al. data (in analogy to the findings from a comparison between CMFGEN and FASTWIND by Massey et al. 2013). Martins et al. (2015a) adopted a depth-variable microturbulent velocity starting from  $10 \text{ km s}^{-1}$  at the photosphere and reaching 10% of the terminal velocity at the top of the atmosphere. Consequently, the comparison of microturbulent velocities in Fig. 8 is restricted to the work of Holgado et al. (2018), with our values being smaller by trend (we note that only upper limits were provided by Holgado et al. in many cases from the analysis of the He I/II lines, which are not ideal indicators for microturbulence because of their strengths). We conclude that our hydrostatic hybrid non-LTE approach to the quantitative spectroscopy of weak-wind O-type dwarfs produces overall results consistent with state-of-the-art hydrodynamic full non-LTE model atmosphere analyses, albeit at smaller microturbulence (as in B-type supergiants; Weßmayer et al. 2022).

Finally, we briefly mention that the O9.2 V star HD 46202 and the O9.7 V star HD36512 were analysed previously with a hybrid non-LTE modelling approach very similar to the one employed here, by Briquet et al. (2011), and by Nieva & Simón-Díaz (2011) and Nieva & Przybilla (2012), respectively. The solutions at  $T_{\text{eff}} = 34\,100 \pm 600 \text{ K}$ ,  $\log g = 4.17 \pm 0.07$  and  $\xi = 6 \pm 2 \text{ km s}^{-1}$  for HD 46202 and  $T_{\text{eff}} = 33\,400 \pm 200 \text{ K}$ ,  $\log g = 4.30 \pm 0.05$  and  $\xi = 4 \pm 1 \text{ km s}^{-1}$  for HD 36512 are consistent with our results.

### 5.3. Elemental abundances

Uncertainties for the elemental abundances in Table 5 were conservatively estimated as the  $1\sigma$  standard deviations from the line-to-line scatter of the individual line abundances within a chemical species. In general, these statistical uncertainties typically range from  $\sim 0.05$ – $0.10$  dex and rarely exceed the upper value. The number of lines analysed per species and object is larger or equal to two, typically. Exceptionally, only the strongest Mg II line  $\lambda 4481 \text{ Å}$  can be analysed for the faster rotators among the sample stars. Standard errors of the mean amount to typically  $0.01$ – $0.03$  dex for the elemental abundances in each star.

In addition, systematic errors need to be considered for the abundances. They depend primarily on the quality of the

model atoms (on the extent, on the processes considered, and on the atomic data employed) and on the uncertainties in the atmospheric parameters (see for example Przybilla et al. 2000, 2001a,b and Przybilla & Butler 2001). Given the experience gained previously, we expect the systematic uncertainties here to amount to  $\sim 0.1$  dex as well.

Table 5 also gives the metallicity  $Z$  of the sample stars (mass fraction). As our coverage of important elements is incomplete, missing elements were supplemented by assuming solar abundances (Asplund et al. 2009). Monte Carlo error propagation was used to constrain the uncertainties.

The abundance determination for many chemical species allows global synthetic spectra to be calculated for each star. This includes blended features that were excluded from the detailed analysis. The global synthetic spectra can closely reproduce many details of the observed spectra, but several features, like N III lines, are still unaccounted for (see Appendix B for a discussion and Fig. B.1 for a comparison of synthetic and observed spectrum for the example of 10 Lac). The goodness-of-fit of our global best model for this star is representative considering the sample overall. We chose to show a detailed spectral fit for this star because it is a very important star among our sample as the MK standard for the spectral-type O9V. In addition, we chose 10 Lac because it is the hottest object of our sample, where non-LTE effects as well as wind effects can be expected to be among the strongest in the sample stars. Many photospheric emission lines in the spectrum of 10 Lac and the other sample stars are reliably reproduced by the global synthetic spectra as well (see Fig. B.2 for some examples). The reproduction is not as complete as reached in previous work on BA-type supergiants (Przybilla et al. 2006a) and B-type main-sequence to supergiant stars (Nieva & Przybilla 2012; Weßmayer et al. 2022). This will require additional efforts in providing the required model atoms.

Previous work on elemental abundances of early B-type stars at distances out to about 400 pc from the Sun has found chemical homogeneity, establishing the CAS values (see Table 5). A direct comparison of the O-star abundances is only possible for two objects, HD 34078 (ID#18) and HD 36512 (ID#20), with the abundances of the latter being in good agreement with the study of Nieva & Przybilla (2012). Overall, agreement of the abundance values for these stars and the CAS is found within the mutual uncertainties, though the neon and aluminium abundances appear

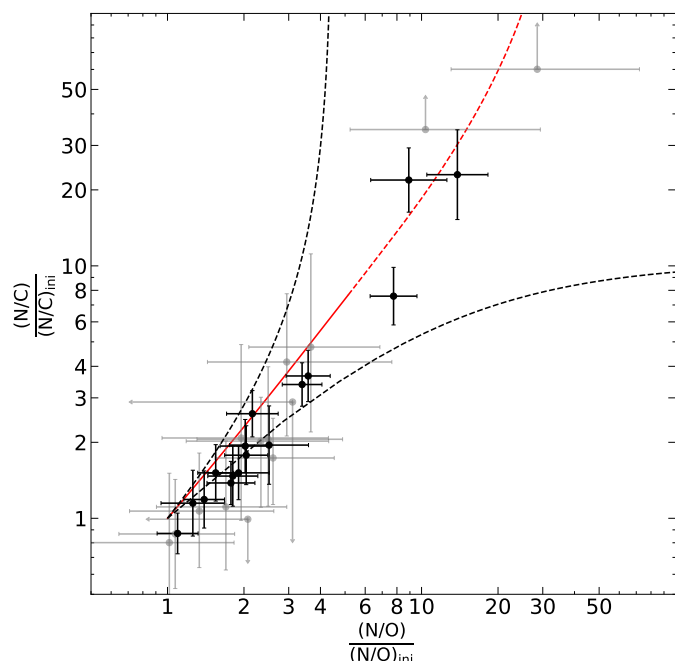


**Fig. 9.** Ratio of the abundance number fraction ( $N/C$ ) as a function of  $N/O$ . The observed abundances (black dots with error bars) are normalised with respect to CAS values and the theoretical data to the solar abundances used for the stellar evolution models. The red line shows a rotating evolutionary model of a  $20 M_{\odot}$  star (Ekström et al. 2012), which is representative for the mean mass of our sample stars. The transition from solid to dashed indicates the end of the main sequence. The dashed black lines show theoretical bounds for the CN cycle (i.e. assuming oxygen shows a constant abundance, shown with the upward-evolving curve) and for the ON cycle (i.e. assuming carbon to be at equilibrium abundance, shown by the horizontally evolving curve). The same stars from the analyses of Martins et al. (2015a,b) are shown in grey.

to be slightly higher than the CAS values. This holds if the comparison is extended to stars at distances out to  $\sim 1$  kpc that are located in the Local Spiral Arm, at similar galactocentric radii as the original CAS sample, objects HD207538 (ID#11), HD 38666 (ID#14), HD 214680 (ID#17), and HD 206183 (ID#19). Elemental abundances in our sample stars beyond the Local Spiral Arm are subject to Galactic abundance gradients.

#### 5.4. Signatures of mixing with CNO-processed material

Several effects lead to mixing of the atmospheres of rotating stars with CNO-processed matter from the stellar core, such as meridional circulation or shear mixing in the presence of differential rotation (e.g. Maeder & Meynet 2012; Langer 2012), further modified by magnetic fields. The most sensitive indicators for mixing with nuclear-processed matter are the nitrogen-to-carbon ( $N/C$ ) and nitrogen-to-oxygen ( $N/O$ ) ratios, which can be combined into a  $N/C$  versus  $N/O$  plot (Przybilla et al. 2010). This plot shows little dependence on the initial stellar masses, rotation velocities, and nature of the mixing processes up to relative enrichment of  $N/O$  by a factor of  $\sim 4$ , and thus it constitutes an ideal test for the quality of observational results (Maeder et al. 2014).

Ratios of the surface carbon, nitrogen and oxygen fractions are expected to appear in a relatively tight locus in the  $N/C$  versus  $N/O$  diagram, as displayed in Fig. 9. The abundance ratios were normalised to the initial values so as to make the comparison with the evolution tracks easier – the observations were

normalised relative to CAS abundances and the models to their respective (solar) initial values. Two analytical boundary solutions can be defined. Either the CN cycle can be assumed to be operational, with oxygen to remain constant at the initial high value, which corresponds to the curve that moves almost vertically away from the pristine values; or the ON-cycle is assumed to be at work, with carbon to remain at a low equilibrium value, which corresponds to the horizontal boundary curve. The predictions of stellar evolution models fall between the two extremes, as with the track for a rotating  $20 M_{\odot}$  star of Ekström et al. (2012) shown in Fig. 9.

The CNO signatures of the sample stars indeed follow the predicted theoretical locus in Fig. 9 tightly, with most objects being compatible with the predicted amount of mixing on the main sequence and falling below a value of four times the initial value. However, we note that the prediction is for a star with an initial rotation  $v_{\text{ini}}$  of 40% of the critical velocity  $v_{\text{crit}}$ , while the true rotational velocities of the sample stars are not known, only their  $v \sin i$  values. The most mixed object that may still be compatible with a main-sequence scenario is BD +57 247 (ID#10) at  $N/C$  and  $N/O$  values around eight times the initial values, probably stemming from an initially fast rotator, as the star is still well within its core hydrogen-burning phase (see Sect. 5.7). The two other objects with a much higher mixing signature are the two ON stars, HD 14633 (ID#2) and HD 201345 (ID#5), which are likely to have reached their extremely high amount of mixing not by rotationally induced processes in a single-star scenario, but from a binary channel involving mass overflow (see the discussion in Sect. 5.7).

As for the atmospheric parameters, our CNO results are also compared to the data from the full non-LTE model atmosphere analyses by Martins et al. (2015a,b), which cover almost all of the sample stars (grey symbols in Fig. 9). Noticeable are the much smaller error bars in our analysis (we note the logarithmic axes of the figure), and some systematic shifts, which are easily recognised for the two ON stars. Moreover, several upper or lower limits from the work of Martins et al. could be replaced by actual determinations in our work. We consider the significant reduction of uncertainties in abundance determinations with respect to previous work on weak-wind late O-type stars as one of the most important achievements of the present work.

Finally, we want to draw attention to the sum of CNO abundances,  $\Sigma \text{CNO} = \log(\Sigma \text{CNO}/\text{H}) + 12$ , which can be used to verify the catalytic nature of the CNO-process, where individual nuclei of C, N and O are only transmuted, the sum being conserved. Again, a meaningful comparison with the CAS values can only be made for stars IDs #18 and #20 (see Sect. 5.3), which leads to compatible values. Also, for the extended range of stars #11, #14, #17 and #19 compatibility is found, with the exception of slightly high values for HD 38666 (ID#14), which, however, are in agreement when systematic uncertainties of the abundances are considered. For the other objects Galactic abundance gradients have to be considered once more. Only the ON star, HD 14633 (ID#2), is noticeable for its low  $\Sigma \text{CNO}$  value. We note that this might be explained by contamination from an additional source (see Sect. 2). A second continuum reduces the contrast between line to continuum opacity, weakening the original line depths with respect to a single-star scenario and consequently reducing the derived abundances, which may be a factor here.



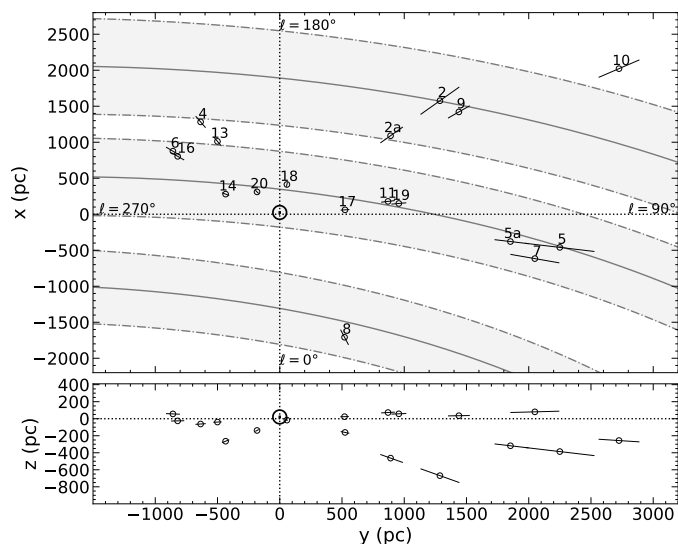


**Fig. 10.** Distribution of the analysed stars in the Milky Way, relative to the position of the Sun at the origin of the Cartesian coordinate system. *Upper panel:* Distribution of the stars in the Galactic plane; the Galactic centre lies in the direction  $\ell = 0^\circ$ . The sketched spiral arm locations are according to Xu et al. (2021), based on the spiral structure model of Reid et al. (2019), from top to bottom: the Perseus, Local, and Sagittarius spiral arms. *Lower panel:* Elevation of the stars above or below the plane. The error bars indicate distance uncertainties from the spectroscopic distances and for IDs#2a and 5a from the inverted *Gaia* EDR3 parallaxes. Numbers correspond to the internal ID numbers.

### 5.5. Spectroscopic distances

Spectroscopic distances for the sample stars as calculated using Eq. 2 are quoted in Table 4. Based on these the distribution of the sample stars in the Milky Way in a Cartesian coordinate system centred on the Sun is shown in Fig. 10. This shows the projection on the Galactic plane in the upper panel and perpendicular to it in the lower panel. The positions of the stars can be compared to the local spiral structure based on *Gaia* EDR3 data by Xu et al. (2021), implying that stars ID#5 to 7, 11, 14, and 16 to 20 are located in the Local spiral arm, star ID#8 is located in the Sagittarius spiral arm and the remainder of the analysed stars in the Perseus spiral arm. It is reassuring to find these young stars overall within spiral arms, as expected, and it is a first qualitative indicator that the spectroscopic distances are not too far off from *Gaia* EDR3 constraints on the star-forming regions of the Milky Way. With regard to the  $z$  distance, most stars are located within one scale height of the thin disc, again as can be expected. Exceptions are the two runaway and ON stars HD 14633 (ID#2) and HD 201345 (ID#5), with BD +57 247 (ID#10), appearing to be an intermediate case (we note that the scale height is in principle increasing towards the outer Galactic disc, Yu et al. 2021). The classical runaway star HD 38666 ( $\mu$  Col, ID#14) has also reached some distance from the Galactic plane, about two scale heights. The other classical runaway in the star sample, HD34078 (AE Aur, ID#18) is located well within the thin disc.

A comparison of our spectroscopic distances with the independent distances based on inverted *Gaia* EDR3 parallaxes is shown in Fig. 11. Overall, good agreement of the two independent distances is found, with the relative differences amounting to typically less than  $\sim 10\%$ . Significantly larger spectroscopic distances are found for HD 214680 (10 Lac) and the two runaway ON stars HD 14633 and HD 201345, a significantly lower spectroscopic distance is found for HD 46202. The case

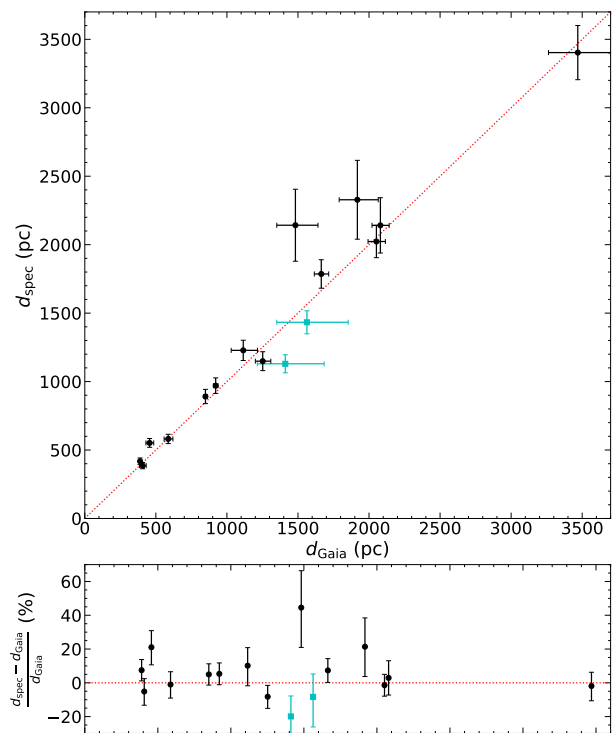


**Fig. 11.** Comparison of *Gaia* EDR3 parallax-based distances with our spectroscopic values (upper panel) and the relative differences between them (lower panel). Stars with a RUWE factor  $> 4$  are marked by cyan squares.

of 10 Lac is discussed in detail in Appendix A. In brief, the *Gaia* EDR3 parallax measurement seems to be systematically biased, but an average *Gaia* EDR3-based distance to the Lac OB1b association – if adopted for 10 Lac – is in good agreement with the spectroscopic distance. The differences for the two ON stars are likely related to their particular evolutionary history (see below), and the spectroscopic distance to HD 46202 may be affected by unrecognised systematic effects of the companion on the analysed spectrum. We note that the *Gaia* EDR3 distance to HD 46202 fits the parent NGC 2244 cluster distance better (see Appendix C) despite the close companion not being accounted for in the five-parameter solution of EDR3, probably leading to the large re-normalised unit weight error (RUWE)  $> 4$  for this star.

### 5.6. Interstellar sight lines – Reddening law

Two examples of ATLAS9 model flux fits to observed SEDs are shown in Fig. 12. One example is for 10 Lac (HD 214680), which has a wide HST spectrophotometric coverage throughout the UV and optical, as extracted from CALSPEC (Bohlin et al. 2014) in addition to our adopted standard photometric coverage. The second example is for the more reddened star HD 54879, which has only photometric coverage of the observed SED. A similar fit quality was achieved for the other sample stars. Both parameters,  $E(B - V)$  and  $R_V$  could be determined to high precision and accuracy facilitating further studies of ISM properties that depend on such high-quality characterisations of the sight lines towards the background stars (e.g. Ebenbichler et al. 2022). The data for  $R_V$  range between 2.5 and 3.35 and concentrate mostly around the typical ISM value of 3.1, and the reddening values vary between 0.05 and 0.90 (see Table 4 for a summary).

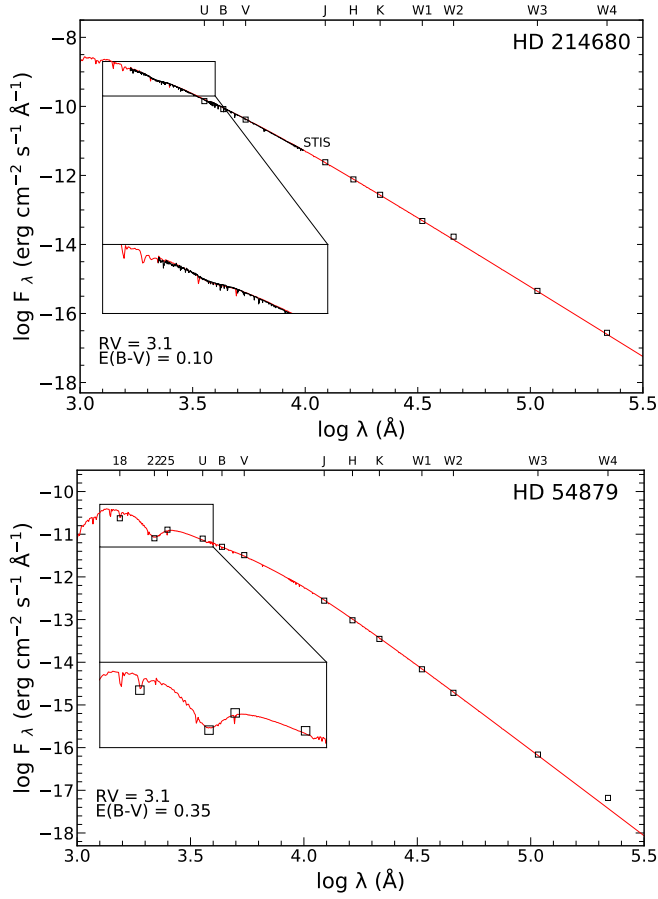


**Fig. 12.** Example SED fits of reddened ATLAS9 fluxes (red) to observed UV-spectra (black), if available, and photometric measurements for two sample stars: Johnson *UBV* (Mermilliod 1997), 2MASS *JHK* (Cutri et al. 2003), WISE *W1* to *W4* (Cutri et al. 2021), and ANS magnitudes (Wesselius et al. 1982). The insets zoom in on the UV range.

We emphasise that UV coverage is highly important for a tight ISM sight line characterisation via SED fitting. While the HST data have the highest quality, it is a rare resource. The extensive coverage of bright hot stars in the IUE archive is therefore an asset. However, many valuable complementary data are found in the less well-known archives of the ANS (Wesselius et al. 1982) and TD1 (Thompson et al. 1995) missions.

### 5.7. Evolutionary status

The evolutionary status of the sample stars on the main sequence can be constrained by comparison with stellar evolution tracks. Three complementary diagnostic diagrams may be employed for this, the Kiel diagram ( $\log g$  vs  $\log T_{\text{eff}}$ ), the physical HRD ( $\log L/L_{\odot}$  vs  $\log T_{\text{eff}}$ ) and the spectroscopic HRD (sHRD,  $\log(\mathcal{L}/\mathcal{L}_{\odot})$  versus  $\log T_{\text{eff}}$ , introduced by Langer & Kudritzki 2014, with  $\mathcal{L} = T_{\text{eff}}^4/g$ ). The Kiel diagram and the sHRD are based solely on observed atmospheric parameters. On the other hand, the physical HRD requires knowledge of the distance and interstellar extinction. The extinction is derived from  $A_V = R_V E(B - V)$ , and we prefer spectroscopic distances. The positions of the sample stars in all three diagrams with respect to evolutionary tracks for non-rotating stars by Ekström et al. (2012) are given in Fig. 13 and we stress the very similar positions relative to the evolution tracks in all three diagrams. Ages are then determined from the comparison with the isochrones.

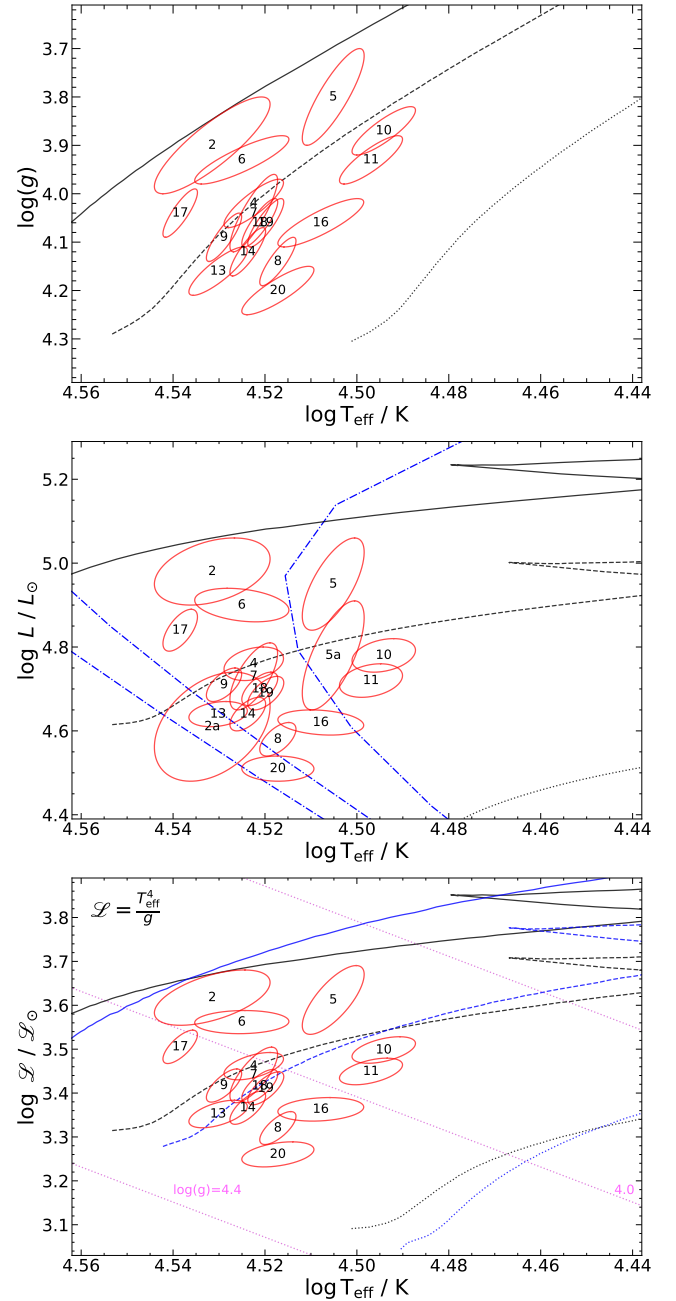


**Fig. 13.** Position of the analysed stars (red ellipses) in the  $T_{\text{eff}}\text{-}\log(g)$  diagram (upper panel), HRD (middle panel) and sHRD (lower panel). The error ellipses outline  $1\sigma$ -uncertainties, the stars are identified by their ID number according to Table 1. Additionally, evolutionary tracks of Ekström et al. (2012) for non-rotating stars at solar metallicity  $Z = 0.014$  are indicated ( $25 M_{\odot}$ : solid,  $20 M_{\odot}$ : dashed,  $15 M_{\odot}$ : dotted line). The HRD includes isochrones from Ekström et al. (2012) for  $\log \tau_{\text{evol}}(\text{yr}) = 6.0, 6.4$  and  $6.7$  (blue dash-dotted lines, left to right). In the sHRD lines of constant  $\log g$  are indicated by dotted magenta lines. In addition the sHRD shows evolutionary tracks for rotating stars ( $v/v_{\text{crit}} = 0.4$ ) in blue for comparison.

The picture is consistent with the evolution of core hydrogen-burning single stars with masses of  $17.5 M_{\odot}$  to about  $23 M_{\odot}$  distributed from close to the ZAMS to an age of  $\log \tau_{\text{evol}}(\text{yr}) \simeq 6.8$ , that is, quite advanced in the main-sequence evolution.

The comparison with evolution tracks for non-rotating stars is mostly motivated by the relatively small  $v \sin i$  of the stars. However, the values of  $i$  are not known, and therefore one can

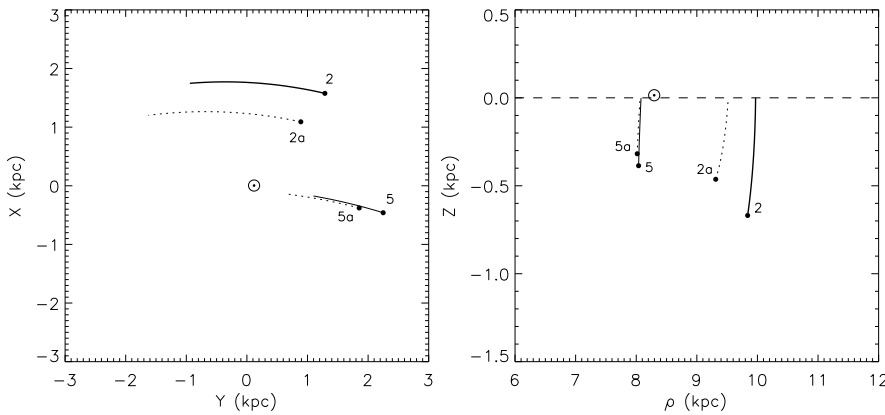


**Fig. 14.** Sketch of the orbits of the two sample runaway ON stars HD 14633 (IDs#2, 2a) and HD 201345 (IDs#5, 5a) in the Galactic potential. Galactic Cartesian coordinates  $XYZ$  are employed, with the origin shifted to the position of the Sun for better comparison with Fig. 10, adopting the galactocentric distance from the [Gravity Collaboration et al. \(2019\)](#). *Left panel:* Galactic plane projection. *Right panel:* Meridional projection,  $\rho$ , is the galactocentric distance, with the Galactic mid-plane indicated by the dashed line. The current positions of the stars are indicated by black dots, the curves show the trajectory calculated backwards in time until the Galactic mid-plane was crossed.

expect the stars to rotate faster than is apparent. A comparison with rotating evolutionary tracks shows mean deviations below 3% in  $M/M_{\odot}$  and below 1% in  $\log \tau_{\text{evol}}$ . This view is supported by the CNO mixing signature (Fig. 9), but the mixing is compatible with initial rotation velocities  $v_{\text{ini}}/v_{\text{crit}} < 0.4$ , that is, excluding faster rotation with the possible exception of BD +57 247 (and the different evolution scenarios for the two ON stars; see below). Systematic effects on the derived parameters are covered well by the error ellipses, as the evolution of non-rotating and initially 40% critically rotating stars is very similar in this part of the HRD (see Fig. 5 of [Ekström et al. 2012](#)).

The presence of large-scale magnetic fields is known to potentially affect the evolution of massive stars, including magnetic braking ([Meynet et al. 2011](#)). Two stars of the sample were found to show magnetic fields: HD 54879 ([Castro et al. 2015](#)) and HD 57682 ([Grunhut et al. 2009](#)), both with field strengths below 1 kG. A spurious detection of a magnetic field in HD 34078 (AE Aur) was reported by [Grunhut et al. \(2017\)](#). For all other objects at least one spectropolarimetric non-detection of magnetic fields has been reported in the literature ([Fossati et al. 2015](#); [Grunhut et al. 2017](#); [Schöller et al. 2017](#)), except for BD +57 247. As the spectrum of this star adopted for the present work was taken in spectropolarimetric mode, we briefly inspected the pipeline-reduced Stokes  $V$  spectrum, but no obvious spectropolarimetric signature is present (a more thorough analysis is desirable, but beyond the scope of the present work). The presence of magnetic fields leads to rotational modulation because of the formation of spots on the surface, which in turn allows rotational periods to be determined. Indeed, both magnetic stars turn out to be (extremely) slow rotators, with HD 57682 having a rotational period of  $\sim 63.5$  d ([Grunhut et al. 2012](#)) and HD 54879 of possibly 7.2 yr ([Järvinen et al. 2022](#)). In terms of CNO mixing signatures, HD 57682 shows the fifth strongest signature of our star sample, while HD 54879 is the least-mixed star. Rotational spin-down for stars with radiation-driven winds in the presence of a magnetic field can be fast, of the order of  $\sim 1$  Myr ([ud-Doula et al. 2009](#)), and so one may speculate that HD 57682 has been spun down from an initially larger rotation rate that allowed mixing to occur, whereas HD 54879 appears to have always been a slow rotator, now spun down to almost zero rotation.

Finally, we wish to address the evolutionary status of the two ON stars in our sample, HD 14633 (ID#2) and HD 201345 (ID#5). Their mixing signature can only be reached with difficulty on the main sequence in the framework of rotational mixing in single star evolution. Instead, they may have resulted from the evolution of close binaries (e.g. [Vanbeveren et al. 1998](#); [Langer 2012](#)). As the evolution of close binaries involves ad-

ditional (continuous) parameters, such as the initial masses of the stars and the initial period of the binary (e.g. [Wellstein et al. 2001](#)), properties of the resulting evolving binary systems are best studied via population synthesis (e.g. [Sen et al. 2022](#)). Since the calculation of tailored evolution scenarios is beyond the scope of the present paper, we can only sketch a likely scenario.

The mass donors in close binaries typically evolve into helium stars that only briefly pass the O-type range in the HRD ([Wellstein et al. 2001](#)), so our two sample ON stars may be the long-lived mass gainers, that is, the initially less-massive secondaries of such systems. We stress two findings from the work of [Wellstein et al. \(2001\)](#): i) mass gainers can reach the region of effective temperatures and luminosities of ordinary late O-type stars as investigated here at significantly lower stellar mass and ii) they can spend millions of years there.

Both sample ON stars are located untypically far from the mid-plane of the Galactic disc, where the higher gas densities favour star formation to occur, at more than two to three scale heights ([Yu et al. 2021](#)) (see our Sect. 5.5). HD 14633 is a runaway in a SB1 system with a  $\sim 15.4$  d orbital period, high eccentricity ( $e \approx 0.7$ ) and small mass function ([Bolton & Rogers 1978](#); [Boyajian et al. 2005](#); [Mahy et al. 2022](#)), in which the low-mass companion is suggested to possibly be a neutron star in a ‘quiet’ massive X-ray binary by [Boyajian et al. \(2005\)](#). On the other hand, HD 201345 shows no signs of radial-velocity variability ([Martins et al. 2015b](#)) – it may therefore be single –, but like HD 14633 it is a runaway star. The question arises as to which mechanism led the stars to become runaway stars and whether this may be related to them showing an extremely pronounced CNO mixing signature.

We employed the Galactic potential as described by [Allen & Santillan \(1991\)](#) together with the code of [Odenkirchen & Brosche \(1992\)](#) to calculate the Galactic orbit and kinematic parameters of the two stars for two solutions, depending on whether  $d_{\text{spec}}$  (solution for ID#2 and 5) or alternatively  $d_{\text{Gaia}}$  (solution ID#2a and 5a) is used to test the single-star or binary hypothesis. Otherwise, *Gaia* EDR3 proper motions were used and radial velocities of  $-38.17 \pm 0.08$  km s $^{-1}$  ([Pourbaix et al. 2004](#)) for HD 14633 and of  $19.2 \pm 2.5$  km s $^{-1}$  ([Gontcharov 2006](#)) for HD 201345. The results are sketched in Fig. 14, in the Galactic plane projection and for a meridional cut. For reasons of clarity, we do not show error ranges (from Monte Carlo calculations), as they are comparatively large and dominated by the uncertainties in the distances. The space velocities of HD 14633 relative to the standard of rest are 75 and 58 km s $^{-1}$  for cases 2 and 2a, and 102 and 86 km s $^{-1}$  for HD 201345 for cases 5 and 5a, respectively. The velocity components pointing away from the Galactic mid-plane are 47 and 26 km s $^{-1}$  for cases 2 and 2a, and 73 and



59 km s<sup>-1</sup> for cases 5 and 5a, respectively. The flight times from the Galactic mid-plane to the current position amount to 12 and 13 Myr for cases 2 and 2a, and to ~5 Myr for both cases 5 and 5a.

A possible scenario for case 5a for HD 201345 may be that it had experienced mass overflow as the gainer in a binary system, now exposing highly CNO-processed material at its surface that was close to the core of its initial binary companion. This companion may have subsequently exploded in a core-collapse supernova, breaking up the system and thus explaining the current single-star nature of HD 201345. The flight time necessary to reach the current position is likely compatible with its life time, in particular if the breakup happened from a position within one scale height below, instead of the mid-plane itself. We note that the flight time is still compatible with the stellar lifetime for case 5, with a dynamical ejection scenario (Poveda et al. 1967) as an alternative to the supernova ejection scenario (Blaauw 1961). However, the CNO mixing signature remains difficult to explain in that case. We therefore favour the binary scenario for HD 201345, with current fundamental stellar parameters according to case 5a.

The travel time for HD 14633 to its current position rules out a scenario where it has evolved as a single star without interaction with its binary partner (case 2), as this is about 50% longer than the main-sequence lifetime of such a late O-type star. Even if it started from within one scale height below the disc, case 2 is unlikely. Consequently case 2a is more likely, implying that HD14633 accreted highly processed matter from its companion during the evolution of the binary. The apparently more massive companion exploded in a core-collapse supernova (if the neutron star nature of the companion is correct; Boyajian et al. 2005), without breaking up the system, but the supernova kick sufficed to make the system a runaway. A central question is whether accretion onto a main-sequence star can produce a ~10 M<sub>⊙</sub> object with the observed luminosity of  $\log L/L_{\odot} \approx 4.6$  at the derived  $T_{\text{eff}}$  of sufficient lifetime (an ordinary 10 M<sub>⊙</sub> star produces  $\log L/L_{\odot} \approx 3.0$  for a ~25 Myr lifetime). Perhaps accretion onto a helium star needs to be invoked, implying a more complex mass exchange history for the binary. As already mentioned, without detailed binary evolution modelling – which is beyond the scope of the present paper – no final conclusions on the past evolution of HD 14633 can be drawn here.

## 6. Summary of individual objects

Important details for the individual sample stars are summarised in the following, both from the literature and the present work. The comparison with literature data from Sect. 5.2 is not repeated here in detail.

HD 14633 (ID#2). This ON star with markedly enriched nitrogen and both depleted carbon and oxygen is probably the most enigmatic object of our star sample. It is the visible component of a runaway SB1 system with ~15.4 d orbital period, high eccentricity and small mass function (Bolton & Rogers 1978; Boyajian et al. 2005; Mahy et al. 2022), located about 3 scale heights below the Galactic mid-plane, a position that requires ~13 Myrs to reach it from the mid-plane within the Perseus spiral arm. This is longer than the lifetime of a normal late O-type star. The system is further complicated by the presence of a second optical source, resolved by the Fine Guidance Sensor on board the HST, at ~20 mas distance with  $\Delta m_{\text{F5ND}} \approx 1.6 \pm 1.1$  mag (Aldoretta et al. 2015), which corresponds to a linear distance of ~30 AU at  $d_{\text{Gaia}} \approx 1.5$  kpc (i.e. it is not related to the close companion). As a runaway triple system appears to be unlikely,

this is probably a chance alignment along the line of sight (it should be on the faint end of the magnitude difference found, as we see no indication of features from this second light source, neither in our spectrum nor in the SED; see also Mahy et al. 2022). HD 14633 has a RUWE of 1.090 in *Gaia* EDR3, apparently the second source is not interfering with the astrometric solution either (in view of the apparent zero impact of the second light source on all observables an independent confirmation of its existence is desirable). Our derived parameters agree very well with those from the most recent CMFGEN-based analysis by Mahy et al. (2022), in particular with respect to the  $d_{\text{Gaia}}$ -based (spectroscopic) mass. The O-star luminosity of such a ~10 M<sub>⊙</sub> star may require consideration of a more complex evolution history, possibly with accretion of highly CNO-processed material onto a helium star. Certainly, the star deserves further investigations in particular regarding population synthesis in the context of binary evolution in order to pinpoint its origin.

HD 258691 (ID#4). The star is one of the seven O-stars members of the young open cluster NGC 2244 that excite the Rosette Nebula (Román-Zúñiga & Lada 2008). The probably most reliable distance to NGC 2244 ( $1.39 \pm 0.1$  kpc) and age ( $2.3 \pm 0.2$  Myr) determination available in the literature stems from the analysis of the detached eclipsing massive binary V578 Mon (Hensberge et al. 2000). The distance is shorter than photometric estimates of typically 1.6 to 1.7 kpc (see Román-Zúñiga & Lada 2008), but it is in excellent agreement with our spectroscopic distance of HD 258691 and the *Gaia* EDR3-based distance to NGC 2244 of  $1464_{-84}^{+94}$  pc ( $1\sigma$  standard deviation; see Appendix C); the *Gaia* EDR3 astrometric solution for HD 258691 is unreliable because of a RUWE of ~7. Our analysis complements the work of Martins et al. (2012) who have analysed all the O stars of NGC 2244 using full non-LTE techniques with CMFGEN, except for HD 258691. They find an age of about 2 to 4 Myrs for the O-star population in NGC 2244, which is in good agreement with our derived age of HD 258691. Finally, we note the apparent visual faintness of HD 258691 when compared to the other NGC 2244 O stars, it is about 1.5 mag fainter in *V* than the next brightest O star, HD 46202. This comes from a much higher reddening, as the star is located close to a dark lane in the Rosette Nebula. In the *K*-band it is only 0.2 mag fainter than HD 46202.

HD 201345 (ID#5). The second runaway ON star of our star sample that has travelled untypically far from the Galactic mid-plane, its flight time being compatible with its age. It appears to be single and has likely accreted highly processed matter from a companion, which apparently exploded in a core-collapse supernova that broke apart the binary and accelerated HD 201345 out from the Galactic plane, with a footpoint of the orbit in the Local spiral arm. Its mass is less than expected for a normal late O-type star, but in the range of mass-gaining secondaries according to the binary evolution models of Wellstein et al. (2001).

HD 57682 (ID#6). This is a runaway star from the CMa OB1 association, ejected about 1 Myr ago possibly in a binary supernova event, showing a bow shock in the WISE W3 and W4 bands (Fernandes et al. 2019). The star is magnetic, with a field strength of below 1 kG (Grunhut et al. 2009), and it is a slow rotator with a period of ~63.5 d (Grunhut et al. 2012). It shows one of the stronger CNO-mixing signatures of the sample stars.

HD 227757 (ID#7). The star is a member of the Cyg OB3 association (e.g. Garmany & Stencel 1992; see Quintana & Wright 2021 for an *Gaia* EDR3 view on this). Our  $T_{\text{eff}}$  and  $\log g$  values are significantly higher than those derived by Mahy et al. (2015) based on an analysis with CMFGEN, but agreement is found for the fundamental stellar parameters. The authors estimate an age be-

tween 3 and 5 Myr for the Cyg OB2 association, which is in excellent agreement with our value for HD 227757. The star shows an intermediate level of nitrogen enrichment.

BD -13 4930 (ID#8). The star is a member of the open cluster NGC 6611 in the Eagle Nebula (M16). BD -13 4930 is the brightest star in the original HST image of the ‘Pillars of Creation’, in between the two easternmost pillars (also in 3D; see the discussion by [McLeod et al. 2015](#)). It was previously observed within the VLT-FLAMES survey of massive stars ([Evans et al. 2005](#)) under the ID NGC 6611-006 and analysed using TLUSTY models ([Hunter et al. 2009](#)). [Maeder et al. \(2014\)](#) indicated that the model found using the atmospheric parameters of [Hunter et al. \(2009\)](#) does not provide a convincing fit to the observed spectrum, which is bolstered here by finding significantly different atmospheric parameters and elemental abundances. In particular, we find a higher metallicity than for similar objects in the solar neighbourhood, which is expected for a star in the Sagittarius spiral arm. [Hunter et al. \(2009\)](#) on the other hand found the star to be metal-poor. It is mildly nitrogen-enhanced. NGC 6611 was subject to a thorough investigation based on *Gaia* EDR3 data by [Stoop et al. \(2022\)](#). BD -13 4930 is fully compatible with their derived cluster distance of  $1706 \pm 7$  pc (standard error of the mean), proper motion and radial velocity and a member of the ‘young’ population of massive stars according to its age. Its extinction  $A_V = 1.82$  is smaller than the mean of the young population of stars ( $A_V = 3.6 \pm 0.1$ , [Stoop et al. 2022](#)), but this may be explained by a location in front of the bulk of the cluster as the region shows a marked radial increase in extinction ([McLeod et al. 2015](#)) and the next brightest star of the same spectral type in NGC 6611, BD -13 4928, is 0.65 mag fainter in  $V$ , while they are equally bright in  $K$ .

BD +60 499 (ID#9). The star is located in the open cluster IC 1805, near the centre of the Heart Nebula. We find excellent agreement between the spectroscopic and the *Gaia* EDR3 distance, which is consistent with the *Gaia* EDR3 cluster distance of  $2108^{+129}_{-115}$  pc ( $1\sigma$  standard deviation; see Appendix D). The stellar age is also consistent with the cluster age of 1–3 Myr (e.g. [Massey et al. 1995](#)). BD +60 499 was suggested to be a radial velocity variable ([Huang & Gies 2006](#); [Rauw & Nazé 2016](#)); however, there is no sign of significant second light from the available data. It shows one of the stronger CNO-mixing signatures.

BD +57 247 (ID#10). The star is a probable member of the open cluster NGC 457 according to the WEBDA database<sup>6</sup>. However, its derived distance puts it at the far side of the cluster distance of  $3026^{+262}_{-223}$  pc ( $1\sigma$  standard deviation; see Appendix E). BD +57 247 is also younger than the cluster age of about 24 Myr found in the literature ([Kharchenko et al. 2013](#); [Dias et al. 2021](#)) and also younger than our revised cluster age of ~9–10 Myr in Appendix E. The star was considered a blue straggler by [Mermilliod \(1982\)](#), but the present results imply it to be a background object to NGC 457, lying about 0.4 kpc farther away. It shows one of the larger reddening values among the sample stars despite a Galactic latitude of  $-4.3^\circ$ . Our analysis is the first using non-LTE techniques. BD +57 247 has the largest CNO mixing signature among the sample stars that may be compatible with rotational mixing on the main sequence, assuming it to be an initially faster rotator than average.

HD 207538 (ID#11). The star is a member of IC 1396, lying outside the Elephant’s Trunk Nebula. Both its spectroscopic and *Gaia* EDR3 distance are compatible with the *Gaia* EDR3 cluster

distance of  $954^{+119}_{-95}$  pc ( $1\sigma$  standard deviation; see Appendix F), though the *Gaia* distance is on the short side. It appears to be at the older limit of the cluster age of 3 to 5 Myr ([Errmann et al. 2013](#)). HD 207538 shows one of the stronger nitrogen enrichments.

HD 46202 (ID#13). Like HD 258691 the star is a member of the NGC 2244 cluster inside the Rosetta Nebula ([Román-Zúñiga & Lada 2008](#)). Observations with the CoRoT satellite detected the presence of  $\beta$  Cep-like pulsations of very small amplitude ( $\sim 0.1$  mmag, [Briquet et al. 2011](#)). The stellar parameters derived in that study are in excellent agreement with the present findings based on two independent data reductions. The spectroscopic distance to HD 46202 is shorter than the *Gaia* EDR3-based cluster distance of  $1464^{+94}_{-84}$  pc ( $1\sigma$  standard deviation; see Appendix C), while the *Gaia* EDR3 astrometric solution for HD 46202 is unreliable because of a  $\text{RUWE} \approx 5$ . The poor astrometric solution may be related to the presence of a close companion to HD 46202, at a distance of  $\sim 87$  mas and  $\Delta m_{F583W} = 2.166 \pm 0.008$  mag ([Aldoretta et al. 2015](#)). This would correspond to a spectral type of B1.5 or B2 for the companion, which is in the middle of the range of spectral types where  $\beta$  Cephei pulsations are strongest. Possibly, the observed sub-millimagnitude pulsational amplitudes do not stem from the O star, but from the companion, diluted in magnitude in the combined light. This may have the potential to explain why the excitation of the observed pulsation modes is inconsistent with the observed atmospheric parameters of the O star ([Briquet et al. 2011](#)). The presence of a binary companion of such a magnitude usually leads to an observable second line system. In order to hide this within the observed narrow lines, one would need to see the system from near-pole on, such that radial-velocity variations are absent ([Chini et al. 2012](#)) – and also implying that HD 46202 is actually a faster rotator. Further investigations should be undertaken to study whether second light and possibly fast (differential) rotation and gravity darkening ([Zorec et al. 2017](#)) can resolve these remaining discrepancies.

HD 38666 ( $\mu$  Col, ID#14), HD 34078 (AE Aur, ID#18). Both stars are classical late O-type runaway stars originating in the Local Spiral arm. HD 34078 shows a bow shock ([France et al. 2007](#)). They were suggested to stem from a common ejection event in the nascent Orion Trapezium cluster based on Hipparcos data ([Hoogerwerf et al. 2000](#)). However, more recent investigations based on *Gaia* EDR3 measurements dismiss this scenario ([Bhat et al. 2022](#)). Our analysis finds very similar atmospheric and fundamental stellar parameters for both stars. Within the mutual uncertainties they have the same age. HD 38666 shows enriched nitrogen, while HD 34078 is compatible with pristine CAS abundances.

HD 54879 (ID#16). Like HD 57682, this star is a member of the CMA OB1 association, located close to the association centre ([Fernandes et al. 2019](#)). It also shows a magnetic field of strength below 1 kG ([Castro et al. 2015](#)) and is an even slower rotator with a period of possibly longer than 7 yr ([Järvinen et al. 2022](#)). HD 54879 is the least CNO-mixed star of the sample.

HD 214680 (10 Lac, ID#17). 10 Lac is the ionising source of the H II region Sh2-126 in the Lac OB1b association and the anchor point of the MK system for spectral type O9 V. While it was too distant to derive a meaningful distance by the original Hipparcos data release ([ESA 1997](#)) it is on the bright side for the *Gaia* mission. Our spectroscopic distance is in agreement with the re-reduction of the Hipparcos mission by [van Leeuwen \(2007\)](#) and our determination of the Lac OB1b association dis-

<sup>6</sup> <https://webda.physics.muni.cz/>

tance of  $d_{\text{LacOB1b}} = 542^{+65}_{-52}$  pc ( $1\sigma$  standard deviation; see Appendix A for a discussion). Several of the more recent analyses with full non-LTE model atmosphere techniques and our work have converged on consistent stellar parameters for 10 Lac (see Sect. 5.2). It shows an intermediate level of nitrogen enrichment.

HD 206183 (ID#19). The star is a member of IC 1396, lying inside the Elephant's Trunk Nebula. As for HD 207538, both the spectroscopic and the *Gaia* EDR3 distance agree with the cluster distance (see Appendix F), and the stellar age fits with the cluster age. HD 206183 shows near-pristine CNO abundances.

HD 36512 ( $\nu$  Ori, ID#20). The star is the intrinsically bluest member of the Ic subgroup of the Ori OB1 association (for an overview, see e.g. Bally 2008). Traditionally, it was used as an anchor point of the spectral type B0 V in the MK system until a fine adjustment of the classification scheme at the transition from the B to the O stars by Sota et al. (2011) such that it now defines the O9.7 V spectral type. It was reanalysed here as a connection point to previous work using hybrid non-LTE modelling (Nieva & Simón-Díaz 2011; Nieva & Przybilla 2012, 2014), finding agreement in the derived stellar parameters. The star shows CNO abundances consistent with pristine values.

## 7. Summary and discussion

We implemented and tested a hybrid non-LTE modelling technique for the quantitative analysis of weak-wind late O-type stars. The technique provides accurate and precise atmospheric parameters and elemental abundances and, when coupled with stellar evolution models and *Gaia* parallaxes, fundamental stellar parameters as well. This allows a full characterisation of this class of stars to be achieved, except for the stellar wind parameters. Overall, results from previous full non-LTE modelling were reproduced. We went beyond the current state-of-the-art approaches by considering the effects of turbulent pressure on the atmospheric stratification and line formation, which produce small but systematic effects.

Of the initial sample of 20 carefully selected stars from the literature, four had to be excluded from further analysis because of clear contamination of the spectra by second light, which highlights the usefulness of high-S/N and high-resolution spectra in this context. The remaining 16 stars were comprehensively analysed (one for the first time in non-LTE), including interstellar sight line characterisation, and they were individually put in the context of recent findings reported in the literature. Fourteen are 'ordinary' main-sequence stars, though some of them would benefit from further detailed investigations, in particular the binary status of HD 46202. For the two ON stars of the sample, we argue that they accreted strongly CNO-processed matter from their (former) binary companion stars, and that the supernova explosions of these companions led to their expulsion from the Galactic plane as runaway stars. They certainly need to be investigated further in the context of population synthesis models for binary evolution to pinpoint their exact evolution channels.

In the future, extensions of the model atom database, focusing on N III, S III/IV, and Fe IV, would be desirable. Once the observed spectra are comprehensively covered by the models, faster-rotating weak-wind late O-type stars will be fully accessible for analysis. Moreover, it should be possible to analyse lower-resolution spectra of such stars, observed with existing 10-metre-class telescopes even in galaxies beyond the Local Group, such as in the dwarf irregular galaxy Sextans A (Lorenzo et al. 2022). Furthermore, automation of the analysis is required for the analysis of larger spectroscopic datasets (e.g. Blomme et al.

2022; Xiang et al. 2022; Morel et al. 2022; Holgado et al. 2022), with machine-learning techniques being the most promising avenues.

The most important aspect of the present work, besides the atmospheric and spectral modelling, is the impact of *Gaia* data on the characterisation of the weak-wind late O-type stars. Here parallaxes to infer distances, and therefore luminosities and proper motions, are crucial since they allow cluster membership or runaway status to be constrained. They were made available most recently in *Gaia* EDR3. A reassuring result from the present work is the overall good agreement of spectroscopic and EDR3-based distances. However, the uncertainties of both can be considerable. As several of our objects are located in young star clusters, we estimated cluster distances on the basis of EDR3 parallaxes of massive cluster member stars (see the appendices). Noticeable is the large scatter of the member stars in parallaxes, which is also apparent in other works that consider extended cluster star samples (see, for example, the detailed study of NGC 6611 by Stoop et al. 2022). Often, the parallaxes of individual cluster member stars disagree, with the differences being (much) larger than the uncertainties of the individual parallaxes. These differences cannot be overcome by considering zero-point corrections for the parallaxes (e.g. Lindegren et al. 2021). Because of the relative brightness of the cluster members and their relative proximity, a high significance of the parallaxes,  $\varpi/\Delta\varpi > 20$ , is typical, so we ignored zero-point corrections altogether. We conclude that EDR3 parallaxes apparently still contain significant systematics, for example unaccounted binarity, in particular for early-type stars, which require identification and minimisation in future data releases.

The full *Gaia* DR3 (Gaia Collaboration 2022) also provides the atmospheric parameters  $T_{\text{eff}}$  and  $\log g$  for 12 of the 16 stars analysed here. Among them, two-thirds are (mis)classified as white dwarfs with  $T_{\text{eff}}$  between about 21 000 and 30 000 K and  $\log g$  values between 3.5 and 4.0. The other objects are classified as stars with  $T_{\text{eff}}$  between about 6600 and 24 000 K and  $\log g$  values between 2.8 and 3.7. Obviously, the *Gaia* astrophysical parameter inference system (Apsis) needs to be improved in order to enable it to correctly characterise late O-type stars. For the very limited parameter space investigated here, we can confirm that  $\log g$  values are underestimated by  $\sim 0.4$  dex by Apsis for O stars (Fouesneau et al. 2022) – though the maximum deviation for the present stars is  $\sim 1.2$  dex in one case. The  $T_{\text{eff}}$  underestimation is, however, much larger than the 1000 to 5000 K claimed by Fouesneau et al. and amounts to  $\sim 4000$  to 26 000 K, with half of the stars showing deviations of more than 10 000 K.

Finally, one may ask whether the analyses conducted in the present work can contribute to the development of a better understanding of the weak-wind phenomenon. A trivial answer would be no, as the wind lies outside the physical framework established by our hydrostatic approach. However, our work allows the photospheric layers to be looked at in detail. These layers form the base of the stellar wind or, in other words, the lower boundary condition for the wind solution. As we were able to reproduce the observed optical spectra with our global solutions (see Appendix B for an example), without consideration of stellar winds, this indicates that the sample stars have winds that are weak enough not to affect the photospheric layers. Much larger mass-loss rates than predicted by Vink et al. (2000) would be required for this.

A difference from most previous works is the smaller microturbulent velocities (by trend) derived here. Using the hybrid non-LTE approach, we were able to derive individual microturbulence velocities for our sample stars from minimising abun-



dance trends as a function of the strengths of metal lines, in contrast to the majority of literature studies, where the microturbulent velocities at photospheric layers were assumed to have a particular value. The few studies where photospheric microturbulence values for late O-type dwarfs were in fact determined (for SMC stars) found similar values (Bouret et al. 2003; Martins et al. 2004), or they gave compatible upper limits (e.g. Holgado et al. 2018). Microturbulence has an impact on the broadening of spectral lines and therefore on the line acceleration. The effect is such that larger microturbulent velocities give broader lines and therefore provide a higher  $g_L$  in the subsonic region. On the other hand, the shadowing of the continuum flux by the broader photospheric lines leads to a lower line acceleration beyond the sonic point. The combined effect gives a reduced mass-loss rate (Lucy 2007, see also Babel 1996 for some earlier considerations). This behaviour of reduced mass-loss rates in conjunction with larger terminal velocities due to increased turbulent velocities was independently derived by Sundqvist et al. (2019). As a result, the lower microturbulent velocities found here are unlikely to contribute to the solution of the weak-wind problem.

**Acknowledgements.** We are grateful to A. Irrgang for updates and extensions of the DETAIL/SURFACE codes. We thank J. Puls for valuable comments on the manuscript, and our referee E. S. G. de Almeida for suggestions that helped to improve the manuscript. This research has made use of the services of the ESO Science Archive Facility. Based on data obtained from the ESO Science Archive Facility with DOI(s): <https://doi.org/10.18727/archive/24>. Based on observations collected at the Centro Astronómico Hispano Alemán at Calar Alto (CAHA), operated jointly by the Max-Planck Institut für Astronomie and the Instituto de Astrofísica de Andalucía (CSIC), proposal H2005-2.2-016. This research used the facilities of the Canadian Astronomy Data Centre operated by the National Research Council of Canada with the support of the Canadian Space Agency. It is also based on observations made with the NASA/ESA Hubble Space Telescope obtained from the Space Telescope Science Institute, which is operated by the Association of Universities for Research in Astronomy, Inc., under NASA contract NAS 5–26555. This work has made use of data from the European Space Agency (ESA) mission *Gaia* (<https://www.cosmos.esa.int/gaia>), processed by the *Gaia* Data Processing and Analysis Consortium (DPAC, <https://www.cosmos.esa.int/web/gaia/dpac/consortium>). Funding for the DPAC has been provided by national institutions, in particular the institutions participating in the *Gaia* Multilateral Agreement. This publication makes use of data products from the Two Micron All Sky Survey, which is a joint project of the University of Massachusetts and the Infrared Processing and Analysis Center/California Institute of Technology, funded by the National Aeronautics and Space Administration and the National Science Foundation. It also makes use of data products from the Wide-field Infrared Survey Explorer, which is a joint project of the University of California, Los Angeles, and the Jet Propulsion Laboratory/California Institute of Technology, funded by the National Aeronautics and Space Administration. We have made use of the WEBDA database, operated at the Department of Theoretical Physics and Astrophysics of the Masaryk University.

## References

Aldoretta, E. J., Caballero-Nieves, S. M., Gies, D. R., et al. 2015, *AJ*, 149, 26  
 Allen, C. & Santillan, A. 1991, *Rev. Mexicana Astron. Astrofis.*, 22, 255  
 Allen, C. W. 1973, *Astrophysical quantities*, 3rd ed. (London: Athlone Press)  
 Asplund, M., Grevesse, N., Sauval, A. J., & Scott, P. 2009, *ARA&A*, 47, 481  
 Auer, L. H. & Mihalas, D. 1972, *ApJS*, 24, 193  
 Babel, J. 1996, *A&A*, 309, 867  
 Bally, J. 2008, in *Handbook of Star Forming Regions, Volume I*, ed. B. Reipurth (San Francisco: ASP), 459  
 Beauchamp, A., Wesemael, F., & Bergeron, P. 1997, *ApJS*, 108, 559  
 Becker, S. R. & Butler, K. 1988, *A&A*, 201, 232  
 Bhat, A., Irrgang, A., & Heber, U. 2022, *A&A*, 663, A39  
 Blaauw, A. 1961, *Bull. Astron. Inst. Netherlands*, 15, 265  
 Blomme, R., Daflon, S., Gebran, M., et al. 2022, *A&A*, 661, A120  
 Blomme, R., Mahy, L., Catala, C., et al. 2011, *A&A*, 533, A4  
 Bohlin, R. C., Gordon, K. D., & Tremblay, P. E. 2014, *PASP*, 126, 711  
 Bolton, C. T. & Rogers, G. L. 1978, *ApJ*, 222, 234  
 Bouret, J. C., Lanz, T., Hillier, D. J., et al. 2003, *ApJ*, 595, 1182  
 Boyajian, T. S., Beaulieu, T. D., Gies, D. R., et al. 2005, *ApJ*, 621, 978  
 Bragança, G. A., Daflon, S., Cunha, K., et al. 2012, *AJ*, 144, 130

Briquet, M., Aerts, C., Baglin, A., et al. 2011, *A&A*, 527, A112  
 Butler, K. & Giddings, J. R. 1985, *Newsletter of Analysis of Astronomical Spectra*, 9 (Univ. London)  
 Carneiro, L. P., Puls, J., Hoffmann, T. L., Holgado, G., & Simón-Díaz, S. 2019, *A&A*, 623, A3  
 Carneiro, L. P., Puls, J., Sundqvist, J. O., & Hoffmann, T. L. 2016, *A&A*, 590, A88  
 Castro, N., Fossati, L., Hubrig, S., et al. 2015, *A&A*, 581, A81  
 Chen, W. P. & Lee, H. T. 2008, in *Handbook of Star Forming Regions, Volume I*, ed. B. Reipurth (San Francisco: ASP), 124  
 Chini, R., Hoffmeister, V. H., Nasserri, A., Stahl, O., & Zinnecker, H. 2012, *MNRAS*, 424, 1925  
 Chiosi, C. & Maeder, A. 1986, *ARA&A*, 24, 329  
 Chlebowski, T. & Garmany, C. D. 1991, *ApJ*, 368, 241  
 Cutri, R. M., Skrutskie, M. F., van Dyk, S., et al. 2003, *VizieR Online Data Catalog*, II/246  
 Cutri, R. M., Wright, E. L., Conrow, T., et al. 2021, *VizieR Online Data Catalog*, II/328  
 de Almeida, E. S. G., Marcolino, W. L. F., Bouret, J. C., & Pereira, C. B. 2019, *A&A*, 628, A36  
 De Becker, M., Rauw, G., Manfroid, J., & Eenens, P. 2006, *A&A*, 456, 1121  
 Dias, W. S., Monteiro, H., Moitinho, A., et al. 2021, *MNRAS*, 504, 356  
 Dimitrijevic, M. S. & Sahal-Brechot, S. 1990, *A&AS*, 82, 519  
 Drew, J. E., Denby, M., & Hoare, M. G. 1994, *MNRAS*, 266, 917  
 Ebenbichler, A., Postel, A., Przybilla, N., et al. 2022, *A&A*, 662, A81  
 Ekström, S., Georgy, C., Eggenberger, P., et al. 2012, *A&A*, 537, A146  
 Errmann, R., Neuhäuser, R., Marschall, L., et al. 2013, *Astron. Nachr.*, 334, 673  
 ESA. 1997, *ESA Spec. Publ.*, Vol. 1200 (Noordwijk: ESA Publications Division)  
 Evans, C. J., Smartt, S. J., Lee, J. K., et al. 2005, *A&A*, 437, 467  
 Fernandes, B., Montmerle, T., Santos-Silva, T., & Gregorio-Hetem, J. 2019, *A&A*, 628, A44  
 Firnstein, M. & Przybilla, N. 2012, *A&A*, 543, A80  
 Fitzpatrick, E. L. 1999, *PASP*, 111, 63  
 Flynn, C., Sekhri, R., Venville, T., et al. 2022, *MNRAS*, 509, 4276  
 Fossati, L., Castro, N., Schöller, M., et al. 2015, *A&A*, 582, A45  
 Fouesneau, M., Frémat, Y., Andrae, R., et al. 2022, *arXiv e-prints*, arXiv:2206.05992  
 France, K., McCandliss, S. R., & Lupu, R. E. 2007, *ApJ*, 655, 920  
 Froese Fischer, C. & Tachiev, G. 2004, *At. Data Nucl. Data Tables*, 87, 1  
 Froese Fischer, C., Tachiev, G., & Irimia, A. 2006, *At. Data Nucl. Data Tables*, 92, 607  
 Gaia Collaboration. 2022, *VizieR Online Data Catalog*, I/355  
 Gaia Collaboration, Brown, A. G. A., Vallenari, A., et al. 2018, *A&A*, 616, A1  
 Gaia Collaboration, Brown, A. G. A., Vallenari, A., et al. 2021, *A&A*, 649, A1  
 Gaia Collaboration, Prusti, T., de Bruijne, J. H. J., et al. 2016, *A&A*, 595, A1  
 Garland, R., Dufton, P. L., Evans, C. J., et al. 2017, *A&A*, 603, A91  
 Garmany, C. D. & Stencel, R. E. 1992, *A&AS*, 94, 211  
 Garrison, R. F. & Kormendy, J. 1976, *PASP*, 88, 865  
 Giddings, J. R. 1981, PhD thesis, (Univ. London)  
 Goncharov, G. A. 2006, *Astronomy Letters*, 32, 759  
 González, J. F., Briquet, M., Przybilla, N., et al. 2019, *A&A*, 626, A94  
 González, J. F., Hubrig, S., Przybilla, N., et al. 2017, *MNRAS*, 467, 437  
 Gräfener, G., Koesterke, L., & Hamann, W. R. 2002, *A&A*, 387, 244  
 Gravity Collaboration, Abuter, R., Amorim, A., et al. 2019, *A&A*, 625, L10  
 Gray, D. F. 2005, *The Observation and Analysis of Stellar Photospheres*, 3rd edn. (Cambridge: Cambridge University Press)  
 Griem, H. R. 1960, *ApJ*, 132, 883  
 Grigsby, J. A., Morrison, N. D., & Anderson, L. S. 1992, *ApJS*, 78, 205  
 Grunhut, J. H., Wade, G. A., Marcolino, W. L. F., et al. 2009, *MNRAS*, 400, L94  
 Grunhut, J. H., Wade, G. A., Neiner, C., et al. 2017, *MNRAS*, 465, 2432  
 Grunhut, J. H., Wade, G. A., Sundqvist, J. O., et al. 2012, *MNRAS*, 426, 2208  
 Heber, U. 2009, *ARA&A*, 47, 211  
 Heber, U. 2016, *PASP*, 128, 082001  
 Heger, A. & Langer, N. 2000, *ApJ*, 544, 1016  
 Hensberge, H., Pavlovski, K., & Verschueren, W. 2000, *A&A*, 358, 553  
 Herrero, A., Kudritzki, R. P., Vilchez, J. M., et al. 1992, *A&A*, 261, 209  
 Herrero, A., Puls, J., & Najarro, F. 2002, *A&A*, 396, 949  
 Hillier, D. J. & Miller, D. L. 1998, *ApJ*, 496, 407  
 Hillwig, T. C., Gies, D. R., Bagnuolo, William G., J., et al. 2006, *ApJ*, 639, 1069  
 Hirsch, H. A. 2009, PhD thesis, (Univ. Erlangen-Nürnberg)  
 Hirschi, R., Meynet, G., & Maeder, A. 2004, *A&A*, 425, 649  
 Hoag, A. A. & Applequist, N. L. 1965, *ApJS*, 12, 215  
 Holgado, G., Simón-Díaz, S., Barbá, R. H., et al. 2018, *A&A*, 613, A65  
 Holgado, G., Simón-Díaz, S., Herrero, A., & Barbá, R. H. 2022, *A&A*, 665, A150  
 Hoogerwerf, R., de Bruijne, J. H. J., & de Zeeuw, P. T. 2000, *ApJ*, 544, L133  
 Huang, W. & Gies, D. R. 2006, *ApJ*, 648, 580  
 Hubeny, I., Hummer, D. G., & Lanz, T. 1994, *A&A*, 282, 151  
 Hubeny, I. & Lanz, T. 1995, *ApJ*, 439, 875  
 Hunter, I., Brott, I., Langer, N., et al. 2009, *A&A*, 496, 841



- Hunter, I., Dufton, P. L., Smartt, S. J., et al. 2007, *A&A*, 466, 277
- Irrgang, A., Przybilla, N., Heber, U., et al. 2014, *A&A*, 565, A63
- Järvinen, S. P., Hubrig, S., Schöller, M., et al. 2022, *MNRAS*, 510, 4405
- Kaufer, A., Stahl, O., Tubbessing, S., et al. 1999, *The Messenger*, 95, 8
- Kharchenko, N. V., Piskunov, A. E., Schilbach, E., Röser, S., & Scholz, R. D. 2013, *A&A*, 558, A53
- Kimeswenger, S., Rainer, M., Przybilla, N., & Kausch, W. 2021, *AJ*, 161, 66
- Kun, M., Kiss, Z. T., & Balog, Z. 2008, in *Handbook of Star Forming Regions*, Volume I, ed. B. Reipurth (San Francisco: ASP), 136
- Kurucz, R. 1993, CD-ROM No. 13 (Cambridge, Mass.: SAO)
- Kurucz, R. L. 2005, *Mem. Soc. Astron. Ital. Suppl.*, 8, 14
- Langer, N. 2012, *ARA&A*, 50, 107
- Langer, N. & Kudritzki, R. P. 2014, *A&A*, 564, A52
- Lanz, T. & Hubeny, I. 2003, *ApJS*, 146, 417
- Lindgren, L., Bastian, U., Biermann, M., et al. 2021, *A&A*, 649, A4
- Lorenzo, M., Garcia, M., Najarro, F., et al. 2022, *MNRAS*, 516, 4164
- Lucy, L. B. 2007, *A&A*, 468, 649
- Lucy, L. B. 2010, *A&A*, 512, A33
- Maeder, A. & Meynet, G. 2012, *Reviews of Modern Physics*, 84, 25
- Maeder, A., Przybilla, N., Nieva, M. F., et al. 2014, *A&A*, 565, A39
- Mahy, L., Rauw, G., De Becker, M., Eenens, P., & Flores, C. A. 2015, *A&A*, 577, A23
- Mahy, L., Sana, H., Shenar, T., et al. 2022, *A&A*, 664, A159
- Manset, N. & Donati, J.-F. 2003, *Proc. SPIE*, 4843, 425
- Mao, J., Badnell, N. R., & Del Zanna, G. 2020, *A&A*, 643, A95
- Marcolino, W. L. F., Bouret, J. C., Martins, F., et al. 2009, *A&A*, 498, 837
- Marcolino, W. L. F., Bouret, J. C., Rocha-Pinto, H. J., Bernini-Peron, M., & Vink, J. S. 2022, *MNRAS*, 511, 5104
- Martin, W. C., Kaufman, V., & Musgrove, A. 1993, *J. Phys. Chem. Ref. Data*, 22, 1179
- Martins, F., Hervé, A., Bouret, J. C., et al. 2015a, *A&A*, 575, A34
- Martins, F., Mahy, L., Hillier, D. J., & Rauw, G. 2012, *A&A*, 538, A39
- Martins, F., Schaerer, D., Hillier, D. J., & Heydari-Malayeri, M. 2004, *A&A*, 420, 1087
- Martins, F., Schaerer, D., Hillier, D. J., et al. 2005, *A&A*, 441, 735
- Martins, F., Simón-Díaz, S., Palacios, A., et al. 2015b, *A&A*, 578, A109
- Mason, B. D., Wycoff, G. L., Hartkopf, W. I., Douglass, G. G., & Worley, C. E. 2001, *AJ*, 122, 3466
- Massey, P., Johnson, K. E., & Degioia-Eastwood, K. 1995, *ApJ*, 454, 151
- Massey, P., Neugent, K. F., Hillier, D. J., & Puls, J. 2013, *ApJ*, 768, 6
- McLeod, A. F., Dale, J. E., Ginsburg, A., et al. 2015, *MNRAS*, 450, 1057
- Megeath, S. T., Townsley, L. K., Oey, M. S., & Tieftrunk, A. R. 2008, in *Handbook of Star Forming Regions*, Volume I, ed. B. Reipurth (San Francisco: ASP), 264
- Mermilliod, J. C. 1982, *A&A*, 109, 37
- Mermilliod, J. C. 1997, *VizieR Online Data Catalog*, 2168
- Meynet, G., Eggenberger, P., & Maeder, A. 2011, *A&A*, 525, L11
- Meynet, G. & Maeder, A. 2000, *A&A*, 361, 101
- Mokiem, M. R., de Koter, A., Puls, J., et al. 2005, *A&A*, 441, 711
- Moore, C. E. 1993, *Tables of Spectra of Hydrogen, Carbon, Nitrogen, and Oxygen Atoms and Ions* (Boca Raton, FL: CRC Press)
- Morel, M. & Magnenat, P. 1978, *A&AS*, 34, 477
- Morel, T., Blazère, A., Semaan, T., et al. 2022, *A&A*, 665, A108
- Morel, T. & Butler, K. 2008, *A&A*, 487, 307
- Morel, T., Castro, N., Fossati, L., et al. 2015, in *New Windows on Massive Stars*, ed. G. Meynet, C. Georgy, J. Groh, & P. Stee, Vol. 307, 342
- Najarro, F., Hillier, D. J., Puls, J., Lanz, T., & Martins, F. 2006, *A&A*, 456, 659
- Nelder, J. A. & Mead, R. 1965, *Computer Journal*, 7, 308
- Nieva, M. F. & Przybilla, N. 2006, *ApJ*, 639, L39
- Nieva, M. F. & Przybilla, N. 2007, *A&A*, 467, 295
- Nieva, M. F. & Przybilla, N. 2008, *A&A*, 481, 199
- Nieva, M. F. & Przybilla, N. 2012, *A&A*, 539, A143
- Nieva, M. F. & Przybilla, N. 2014, *A&A*, 566, A7
- Nieva, M. F. & Simón-Díaz, S. 2011, *A&A*, 532, A2
- Odenkirchen, M. & Brosche, P. 1992, *Astronomische Nachrichten*, 313, 69
- Pfeiffer, M. J., Frank, C., Baumüller, K., Fuhrmann, K., & Gehren, T. 1998, *A&AS*, 130, 381
- Pourbaix, D., Tokovinin, A. A., Batten, A. H., et al. 2004, *A&A*, 424, 727
- Poveda, A., Ruiz, J., & Allen, C. 1967, *Bol. Obs. Tonantzintla Tacubaya*, 4, 86
- Przybilla, N. 2005, *A&A*, 443, 293
- Przybilla, N. & Butler, K. 2001, *A&A*, 379, 955
- Przybilla, N. & Butler, K. 2004, *ApJ*, 609, 1181
- Przybilla, N., Butler, K., Becker, S. R., & Kudritzki, R. P. 2001a, *A&A*, 369, 1009
- Przybilla, N., Butler, K., Becker, S. R., & Kudritzki, R. P. 2006a, *A&A*, 445, 1099
- Przybilla, N., Butler, K., Becker, S. R., Kudritzki, R. P., & Venn, K. A. 2000, *A&A*, 359, 1085
- Przybilla, N., Butler, K., & Kudritzki, R. P. 2001b, *A&A*, 379, 936
- Przybilla, N., Firnstein, M., Nieva, M. F., Meynet, G., & Maeder, A. 2010, *A&A*, 517, A38
- Przybilla, N., Nieva, M. F., & Butler, K. 2008, *ApJ*, 688, L103
- Przybilla, N., Nieva, M. F., & Edelmann, H. 2006b, *Baltic Astronomy*, 15, 107
- Przybilla, N., Nieva, M. F., Irrgang, A., & Butler, K. 2013, *EAS Publ. Ser.*, 63, 13
- Puls, J., Kudritzki, R. P., Herrero, A., et al. 1996, *A&A*, 305, 171
- Puls, J., Najarro, F., Sundqvist, J. O., & Sen, K. 2020, *A&A*, 642, A172
- Puls, J., Urbaneja, M. A., Venero, R., et al. 2005, *A&A*, 435, 669
- Puls, J., Vink, J. S., & Najarro, F. 2008, *A&A Rev.*, 16, 209
- Quintana, A. L. & Wright, N. J. 2021, *MNRAS*, 508, 2370
- Rauw, G. & Nazé, Y. 2016, *A&A*, 594, A82
- Reid, M. J., Menten, K. M., Brunthaler, A., et al. 2019, *ApJ*, 885, 131
- Rodrigo, C. & Solano, E. 2020, *Contributions to the XIV.0 Scientific Meeting of the Spanish Astronomical Society*
- Rodrigo, C., Solano, E., & Bayo, A. 2012, *IVOA Working Draft*
- Román-Zúñiga, C. G. & Lada, E. A. 2008, in *Handbook of Star Forming Regions*, Volume I, ed. B. Reipurth (San Francisco: ASP), 928
- Rybicki, G. B. & Hummer, D. G. 1991, *A&A*, 245, 171
- Sana, H., de Mink, S. E., de Koter, A., et al. 2012, *Science*, 337, 444
- Sana, H., Le Bouquin, J. B., Lacour, S., et al. 2014, *ApJS*, 215, 15
- Santolaya-Rey, A. E., Puls, J., & Herrero, A. 1997, *A&A*, 323, 488
- Schöller, M., Hubrig, S., Fossati, L., et al. 2017, *A&A*, 599, A66
- Schönberner, D., Herrero, A., Becker, S., et al. 1988, *A&A*, 197, 209
- Schöning, T. & Butler, K. 1989a, *A&AS*, 78, 51
- Schöning, T. & Butler, K. 1989b, *A&A*, 219, 326
- Seaton, M. J. 1962, in *Atomic and Molecular Processes*, ed. D. R. Bates, 375
- Seaton, M. J., Yan, Y., Mihalas, D., & Pradhan, A. K. 1994, *MNRAS*, 266, 805
- Sen, K., Langer, N., Marchant, P., et al. 2022, *A&A*, 659, A98
- Shi, H. M. & Hu, J. Y. 1999, *A&AS*, 136, 313
- Shultz, M., Le Bouquin, J. B., Rivinius, T., et al. 2019, *MNRAS*, 482, 3950
- Simón-Díaz, S., García-Rojas, J., Esteban, C., et al. 2011, *A&A*, 530, A57
- Simón-Díaz, S., Godart, M., Castro, N., et al. 2017, *A&A*, 597, A22
- Simón-Díaz, S. & Herrero, A. 2014, *A&A*, 562, A135
- Simón-Díaz, S., Herrero, A., Esteban, C., & Najarro, F. 2006, *A&A*, 448, 351
- Sota, A., Maíz Apellániz, J., Morrell, N. I., et al. 2014, *ApJS*, 211, 10
- Sota, A., Maíz Apellániz, J., Walborn, N. R., et al. 2011, *ApJS*, 193, 24
- Stoop, M., Kaper, L., de Koter, A., et al. 2022, *arXiv e-prints*, arXiv:2207.08452
- Sundqvist, J. O., Björklund, R., Puls, J., & Najarro, F. 2019, *A&A*, 632, A126
- Sung, H., Bessell, M. S., Chun, M.-Y., et al. 2017, *ApJS*, 230, 3
- Tayal, S. S. 2007, *ApJS*, 171, 331
- Tayal, S. S. & Zatsarinny, O. 2017, *ApJ*, 850, 147
- Thompson, G. I., Nandy, K., Jamar, C., et al. 1995, *VizieR Online Data Catalog*, II/59B
- Tremblay, P. E. & Bergeron, P. 2009, *ApJ*, 696, 1755
- ud-Doula, A., Owocki, S. P., & Townsend, R. H. D. 2009, *MNRAS*, 392, 1022
- van Leeuwen, F. 2007, *A&A*, 474, 653
- van Regemorter, H. 1962, *ApJ*, 136, 906
- Vanbeveren, D., De Loore, C., & Van Rensbergen, W. 1998, *A&A Rev.*, 9, 63
- Villamariz, M. R. & Herrero, A. 2000, *A&A*, 357, 597
- Villamariz, M. R. & Herrero, A. 2005, *A&A*, 442, 263
- Villamariz, M. R., Herrero, A., Becker, S. R., & Butler, K. 2002, *A&A*, 388, 940
- Vink, J. S., de Koter, A., & Lamers, H. J. G. L. M. 2000, *A&A*, 362, 295
- Vink, J. S., de Koter, A., & Lamers, H. J. G. L. M. 2001, *A&A*, 369, 574
- Vink, J. S. & Sander, A. A. C. 2021, *MNRAS*, 504, 2051
- Voels, S. A., Bohannan, B., Abbott, D. C., & Hummer, D. G. 1989, *ApJ*, 340, 1073
- Wade, G. A., Neiner, C., Alecian, E., et al. 2016, *MNRAS*, 456, 2
- Walborn, N. R., Maíz Apellániz, J., Sota, A., et al. 2011, *AJ*, 142, 150
- Wellstein, S., Langer, N., & Braun, H. 2001, *A&A*, 369, 939
- Wesselius, P. R., van Duinen, R. J., de Jonge, A. R. W., et al. 1982, *A&AS*, 49, 427
- Weßmayer, D., Przybilla, N., & Butler, K. 2022, *A&A*, 668, A92
- Wiese, W. L., Fuhr, J. R., & Deters, T. M. 1996, *J. Phys. & Chem. Ref. Data.*, Monograph 7 (Melville, NY: AIP Press)
- Xiang, M., Rix, H.-W., Ting, Y.-S., et al. 2022, *A&A*, 662, A66
- Xu, Y., Hou, L. G., Bian, S. B., et al. 2021, *A&A*, 645, L8
- Yu, Y., Wang, H.-F., Cui, W.-Y., et al. 2021, *ApJ*, 922, 80
- Zorec, J., Rieutord, M., Espinosa Lara, F., et al. 2017, *A&A*, 606, A32

## Appendix A: The distance to 10 Lac

The distance determination to the important MK standard star 10 Lac (HD 214680) deserves a dedicated discussion. The distance is unfortunately not tightly constrained because the star was too distant for the Hipparcos mission to measure a reliable parallax (both in the original and the revised data reduction), and at  $V = 4.88$  mag it is bright for the *Gaia* mission (Gaia Collaboration et al. 2016), in both data releases, DR2 and EDR3. Table A.1 summarises the available parallax  $\varpi$  and proper motion measurements  $\mu_\alpha$  and  $\mu_\delta$  (in right ascension  $\alpha$  and declination  $\delta$ , respectively) from the Hipparcos and *Gaia* missions, as well as the resulting distances, and the spectroscopic distance from the present work. The parallax and proper motion measurements disagree and a resolution of the discrepancies is beyond the scope of the present work. This possibly points to the existence of unconsidered systematic effects.

Only the van Leeuwen (2007) value is compatible with our spectroscopic distance, which may be by chance, so an independent constraint would be desirable. The star 10 Lac is the ionising source of the 10 Lac nebula complex (consisting in particular of the H II region Sh2-126) that coincides with the Lac OB1b association (Chen & Lee 2008) (see our Fig. A.1). Two bright early B-type stars are identified, while two other Lac OB1 stars lie outside of the field shown. An indirect distance estimation can be achieved by analysis of the parallaxes of the fainter Lac OB1b members, for which *Gaia* should have delivered more reliable data.

We therefore selected Lac OB1b association member stars of spectral type B (and 10 Lac) according to Chen & Lee (2008). A summary of *Gaia* EDR3 measurements for these is provided Table A.2, where the name, parallax, proper motion components, the  $G$  magnitude and the RUWE are tabulated. We then applied the following selection criteria. Stars brighter than the sixth  $G$  magnitude were excluded, as were stars with unusual proper motions (see Fig. A.2) and those with a large RUWE, above a value of 1.20. The distance to the Lac OB1b association was calculated from the inverted parallaxes of the remaining 23 objects to  $d_{\text{LacOB1b}} = 542^{+65}_{-52}$  pc ( $1\sigma$  standard deviation), or  $d_{\text{LacOB1b}} = 542^{+14}_{-11}$  pc (standard error of the mean), which agrees well with our spectroscopic distance for 10 Lac.

## Appendix B: Spectral fit for 10 Lac

An example for the fit quality of the global synthetic spectrum with observations is given in Fig. B.1 for the O9 V MK standard star 10 Lac. While the full blue wavelength range is covered, only selected wavelengths are considered beyond that, because the density of diagnostic lines is largely reduced there in the late O-type stars. Overall, excellent agreement is found. One exception is the region around  $\sim 3925$  Å. In contrast to the He II Pickering transitions longwards of  $4000$  Å, He II  $\lambda 3923.49$  Å was not covered by the Stark broadening tables for He II from the detailed quantum-mechanical calculations by Schönning & Butler (1989a,b). Instead, the Griem (1960) theory for Stark-broadened hydrogenic lines as implemented by Auer & Mihalas (1972) was employed, as for the shallow He II lines originating from the  $n = 5$  level, for example He II  $\lambda\lambda 6683.209$  Å and  $6527.107$  Å. A few residuals from the data reduction are also present, as witnessed by a few emission spikes in the last panel of Fig. B.1.

Several observed features are not covered by the synthetic spectrum. These mostly stem from N III. The available nitrogen model atom is insufficient to model the observed lines reliably (this will be improved in future work). Also, some chemical

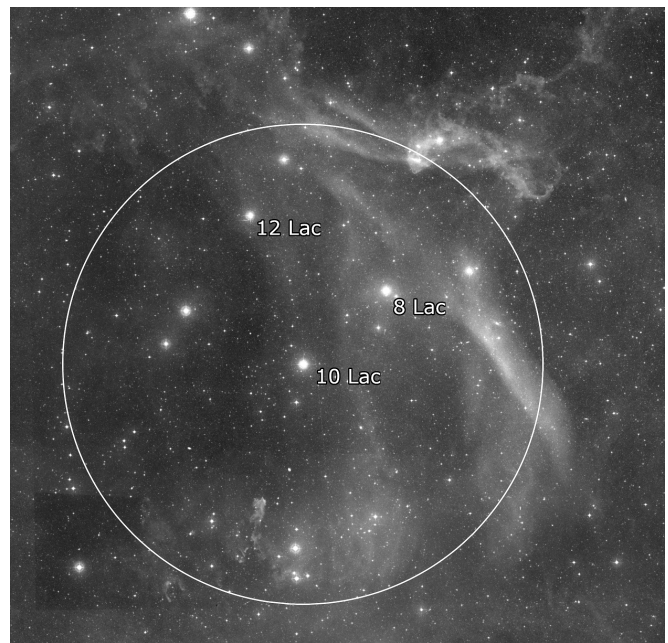


**Fig. A.1.** Image of the Lac OB1 association, adopted from the Digital Sky Survey in the red band. The central extent of the Lac OB1b association is encircled, a few bright stars are labelled.

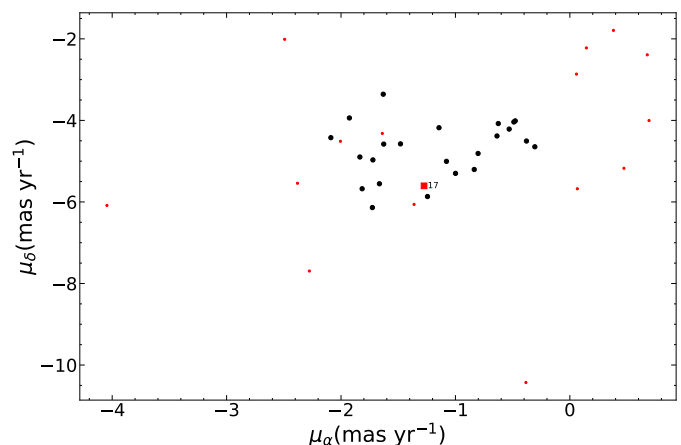


**Fig. A.2.** *Gaia* EDR3 proper motions of stars in the Lac OB1b association. Larger black dots indicate stars retained, small red dots indicate stars removed for the distance estimation of the association based on their brightness, proper motion or RUWE. The sample star 10 Lac (ID#17) is marked by the square.

species, such as sulphur or iron, are completely absent as we lack reliable model atoms. However, they produce only relatively weak features. In addition, some narrow absorption lines, such as the Ca H+K lines, the Na D lines, and a K I resonance line,<sup>7</sup> are of interstellar origin. Diffuse interstellar bands (DIBs; increasingly important in more reddened stars) and the many telluric absorption features due to O<sub>2</sub> (concentrated in the A-, B- and  $\gamma$ -bands of O<sub>2</sub>) and H<sub>2</sub>O bands (e.g. the weak sharp features near H $\alpha$  or the forest of strong lines beyond  $\sim 8900$  Å in Fig. B.1) that are spread over the red wavelength range are also omitted.

<sup>7</sup> Only the K I  $\lambda 7698.9$  Å line is clearly visible, while the other fine-structure component K I  $\lambda 7664.9$  Å overlaps with a saturated telluric O<sub>2</sub> line (see e.g. Kimeswenger et al. 2021), which depends on the radial velocity of the target star.

**Table A.1.** Astrometric data and derived distances for 10 Lac.

$\varpi$ (mas)	$\mu_\alpha$ (mas yr <sup>-1</sup> )	$\mu_\delta$ (mas yr <sup>-1</sup> )	$d$ (pc)	Reference
3.08±0.62	-0.29±0.66	-5.70±0.52	325 <sup>+82</sup> <sub>-55</sub>	Hipparcos, <a href="#">ESA (1997)</a>
1.89±0.22	-0.32±0.25	-5.46±0.19	529 <sup>+70</sup> <sub>-55</sub>	Hipparcos, <a href="#">van Leeuwen (2007)</a>
2.7876±0.2321	-1.437±0.296	-4.803±0.368	391.31 <sup>+32.58</sup> <sub>-29.10</sub>	<i>Gaia</i> DR2, <a href="#">Gaia Collaboration et al. (2018)</a>
2.1920±0.1314	-1.274±0.118	-5.605±0.120	456.20 <sup>+37.10</sup> <sub>-25.80</sub>	<i>Gaia</i> EDR3, <a href="#">Gaia Collaboration et al. (2021)</a>
...	...	...	552±32	spectroscopic, this work
...	...	...	542 <sup>+65</sup> <sub>-52</sub>	<i>Gaia</i> EDR3 distance to Lac OB1b, this work

**Table A.2.** *Gaia* EDR3 parallaxes and photometric and astrometric measurements for stars in the Lac OB1b association.

Name	$\varpi$ (mas)	$\mu_\alpha$ (mas yr <sup>-1</sup> )	$\mu_\delta$ (mas yr <sup>-1</sup> )	$G$ (mag)	RUWE
6 Lac	2.8367 ± 0.1336	-2.380 ± 0.098	-5.541 ± 0.124	4.4775	1.65
10 Lac	2.1920 ± 0.1314	-1.274 ± 0.118	-5.605 ± 0.120	4.8255	1.21
12 Lac	2.5877 ± 0.1327	-2.005 ± 0.150	-4.512 ± 0.117	5.2102	1.21
16 Lac	2.2387 ± 0.0736	-1.639 ± 0.044	-4.319 ± 0.064	5.5638	1.26
<b>HD 212978</b>	2.0135 ± 0.0515	-1.244 ± 0.031	-5.867 ± 0.045	6.1241	1.09
HD 217101	2.2918 ± 0.0423	0.065 ± 0.048	-5.677 ± 0.047	6.1392	0.90
<b>HD 215191</b>	2.1623 ± 0.0519	-0.999 ± 0.045	-5.299 ± 0.041	6.3920	1.11
<b>8 Lac</b>	2.1711 ± 0.0598	-1.721 ± 0.069	-4.969 ± 0.060	6.4409	1.19
<b>HD 214263</b>	1.9604 ± 0.0403	-1.726 ± 0.038	-6.138 ± 0.036	6.8144	1.01
<b>HD 213976</b>	2.0603 ± 0.0446	-1.631 ± 0.027	-3.357 ± 0.041	7.0124	1.08
<b>HD 214432</b>	1.9787 ± 0.0382	-1.835 ± 0.043	-4.898 ± 0.039	7.5643	0.95
HD 216684	1.6846 ± 0.0319	-0.530 ± 0.024	-4.213 ± 0.031	7.7390	1.11
<b>V423 Lac</b>	1.6817 ± 0.0280	-0.477 ± 0.021	-4.012 ± 0.026	7.9560	1.20
<b>HD 212668</b>	1.8088 ± 0.0329	-1.078 ± 0.029	-5.004 ± 0.031	8.0774	1.06
HD 213484	1.5504 ± 0.0268	0.381 ± 0.023	-1.793 ± 0.026	8.2749	1.17
<b>HD 214243</b>	2.0388 ± 0.0390	-2.089 ± 0.029	-4.424 ± 0.037	8.2813	1.08
<b>HD 214098</b>	1.6315 ± 0.0347	-0.306 ± 0.026	-4.647 ± 0.029	8.3035	1.08
HD 212153	0.4510 ± 0.6390	-4.046 ± 0.498	-6.085 ± 0.537	8.6457	9.10
<b>HD 216815</b>	1.6617 ± 0.0276	-0.489 ± 0.017	-4.039 ± 0.022	8.3336	1.16
<b>HD 215211</b>	1.8734 ± 0.0311	-0.836 ± 0.034	-5.204 ± 0.029	8.6368	1.11
<b>HD 216537</b>	1.6559 ± 0.0233	-0.626 ± 0.016	-4.077 ± 0.020	8.7603	1.13
HD 213390	1.3726 ± 0.0167	0.145 ± 0.014	-2.222 ± 0.017	8.8383	0.96
HD 213800	1.6625 ± 0.0229	0.676 ± 0.016	-2.392 ± 0.021	9.1629	1.06
<b>BD +42 4370</b>	1.6166 ± 0.0175	-0.802 ± 0.015	-4.811 ± 0.017	9.2809	0.97
<b>HD 214977</b>	1.7629 ± 0.0204	-1.627 ± 0.011	-4.581 ± 0.019	9.3238	1.06
BD +40 4771	1.1461 ± 0.0229	0.692 ± 0.018	-4.004 ± 0.021	9.4695	1.16
HD 212732	1.6620 ± 0.0253	-2.277 ± 0.022	-7.694 ± 0.026	9.4676	1.33
BD +38 4883	2.0092 ± 0.0239	0.473 ± 0.024	-5.174 ± 0.027	9.4627	1.03
<b>BD +38 4834</b>	2.0849 ± 0.0208	-1.815 ± 0.021	-5.676 ± 0.021	9.5604	1.17
BD +40 4831	2.6886 ± 0.0144	0.058 ± 0.010	-2.864 ± 0.014	9.5632	0.94
<b>HD 214179</b>	1.5980 ± 0.0232	-0.637 ± 0.018	-4.382 ± 0.020	9.6340	1.10
BD +36 4896	1.8517 ± 0.0571	-1.362 ± 0.051	-6.059 ± 0.047	9.6878	3.51
<b>BD +43 4205</b>	1.5696 ± 0.0198	-0.379 ± 0.017	-4.506 ± 0.018	9.8823	1.12
BD +39 4917	2.4690 ± 0.0915	-0.384 ± 0.094	-10.428 ± 0.080	9.8811	4.61
<b>BD +39 4920</b>	1.7941 ± 0.0201	-1.480 ± 0.018	-4.576 ± 0.018	9.9312	1.02
<b>BD +40 4852</b>	1.6312 ± 0.0236	-1.144 ± 0.017	-4.179 ± 0.021	9.9281	1.16
BD +42 4429	0.8706 ± 0.0221	-2.492 ± 0.018	-2.011 ± 0.022	9.9108	1.17
<b>HD 215271</b>	2.1022 ± 0.0177	-1.927 ± 0.013	-3.940 ± 0.017	10.4557	1.09
<b>BD +36 4868</b>	1.9325 ± 0.0182	-1.664 ± 0.015	-5.554 ± 0.016	10.4764	1.07

**Notes.** The names of objects used for the distance estimate of the association are in bold. We rejected the other objects based on their RUWE factor, high brightness or discrepant proper motions.

A number of photospheric emission lines are present in the spectrum of 10 Lac and in the other sample stars. They become more numerous towards the red part of the spectrum, where non-LTE effects are amplified (see e.g. [Przybilla & Butler 2004](#)). They occur between high-lying energy levels. Two examples of the fit of the global synthetic spectra to an O III and a Si III emission line in four sample stars are given in Fig. B.2. This gives additional confidence in the quality of the model atoms as a good fit is achieved without the necessity of fine adjustments of the selected atomic data. We note the stronger contamination of 10 Lac (HD 214680) by telluric H<sub>2</sub>O in the ~8100 Å range in the spec-

trum taken at Calar Alto in Spain as compared with the higher and drier Mauna Kea on Hawaii (spectra of the other three stars were taken at the CFHT).

### Appendix C: The distance to HD 46202, HD 258691, and the Rosette Nebula cluster NGC 2244

The stars HD 46202 and HD 258691 belong to the seven O stars of the open cluster NGC 2244. These seven stars are the main sources of ionising photons that excite the Rosette Nebula. In addition, 24 early B-type stars of spectral types B0 to B3 are

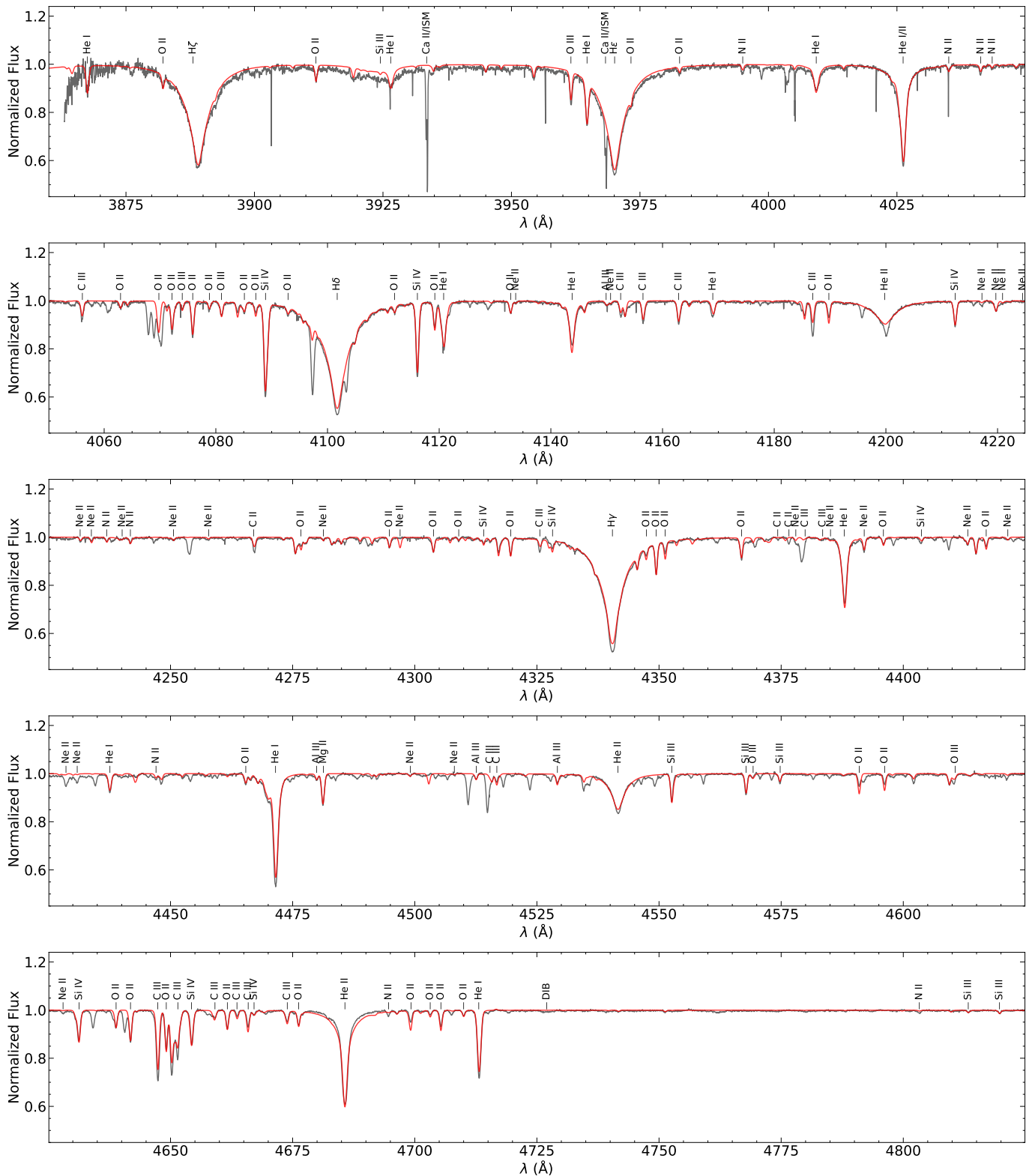


**Fig. B.1.** Comparison between the global synthetic (red) and observed spectrum (black line) for the O9 V standard star 10 Lac (HD 214680) in the spectral range  $\lambda\lambda 3900$  to  $4800 \text{ \AA}$ . Many of the stronger diagnostic lines are identified.

contained in NGC 2244 (see Table 2 of [Román-Zúñiga & Lada 2008](#)). We adopt these 31 stars as basis for the estimation of a cluster distance to NGC 2244 in analogy to Appendix A, with the data collected in Table C.1. The same selection criteria were applied to the *Gaia* EDR3 data. We note that with  $G$  magnitudes between  $\sim 7$  and 15 mag the stars are ideal to deliver high-quality

parallaxes from EDR3. The distribution of all OB-type member stars of NGC 2244 in proper motion space is visualised in the left panel of Fig. C.1, with data from stars that were omitted marked by small red dots. The two sample stars – HD 46202 (ID#13) and HD 258691 (ID#4) – are among those with the most negative proper motions, both in right ascension and in declina-



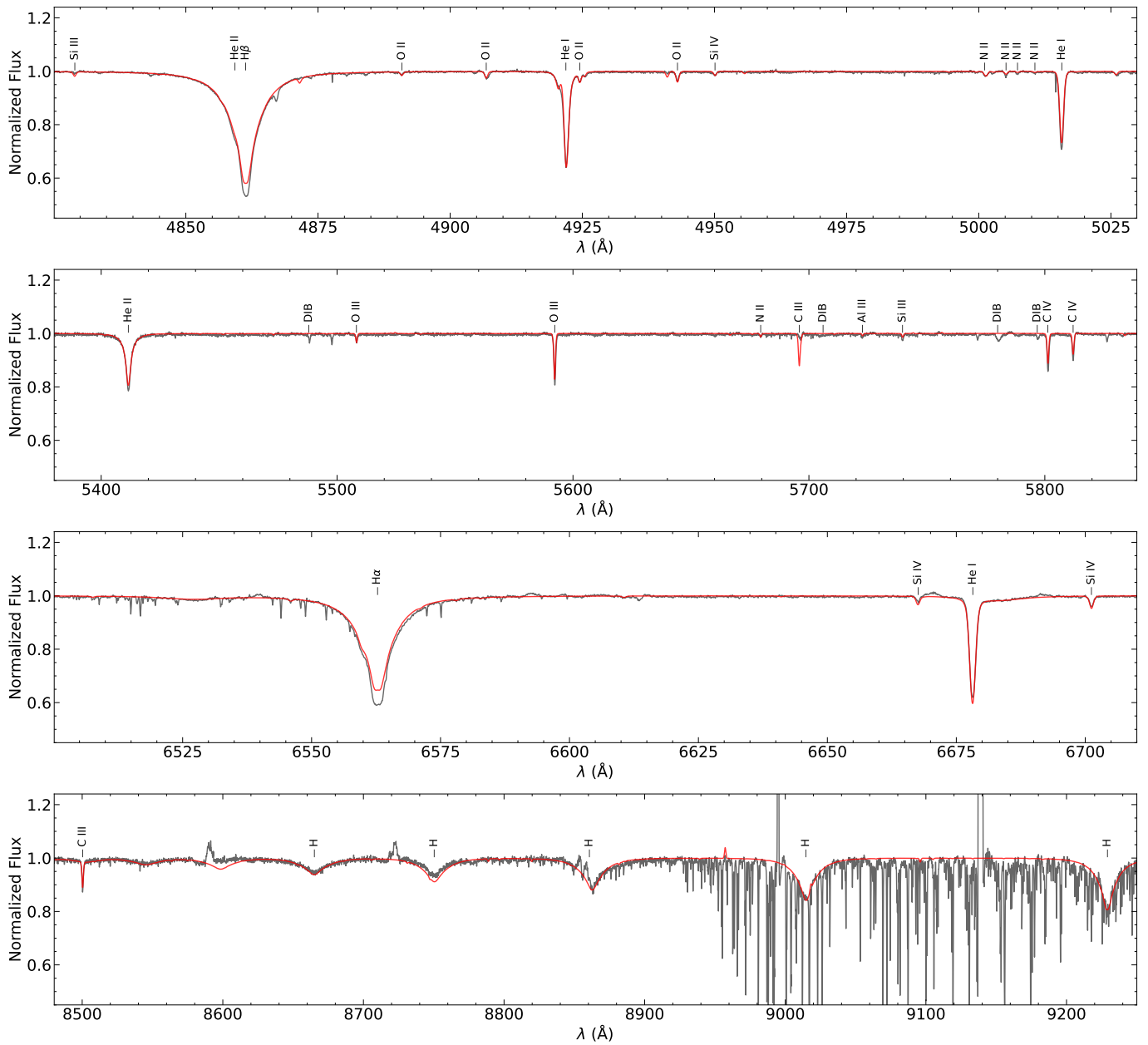


**Fig. B.1. (cont.)** Selected wavelength ranges between  $\sim 4800$  and  $9200 \text{ \AA}$ .

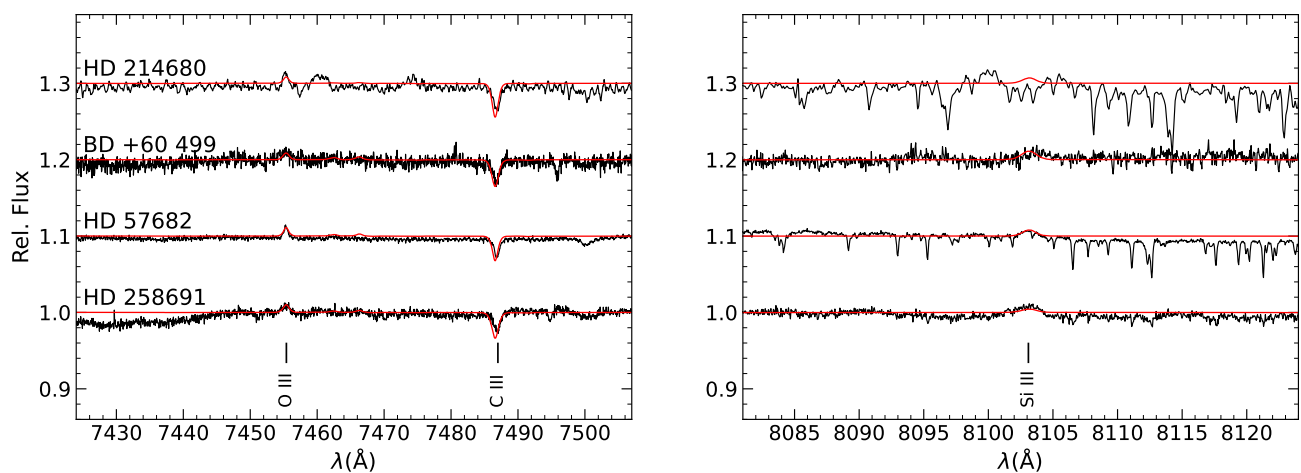


**Fig. B.2.** Same as Fig. B.1, but for examples of O III (*left panel*) and Si III emission lines (*right panel*), for 10 Lac and three other sample stars.

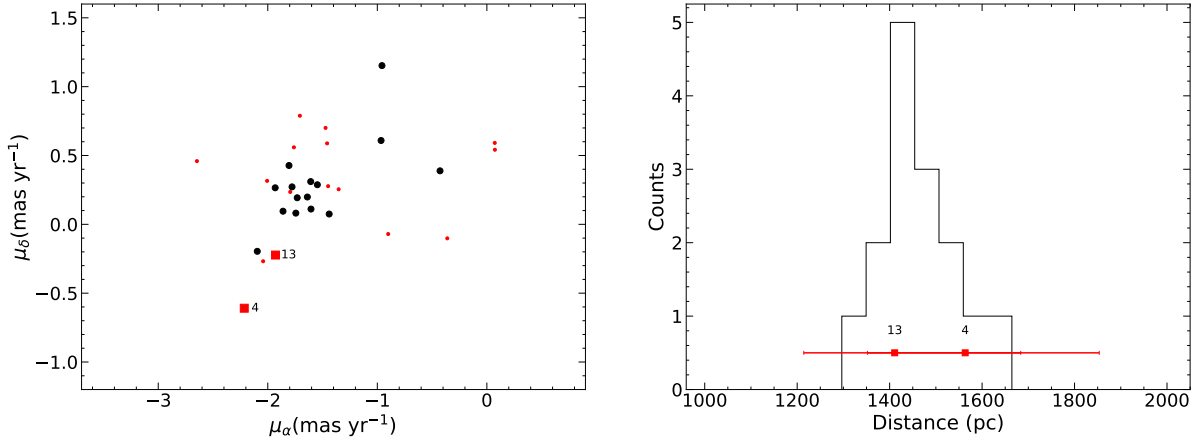


**Fig. C.1.** Proper motion and distances of OB stars in NGC 2244. *Left panel:* *Gaia* EDR3 proper motions of OB stars in the NGC 2244 cluster. Data marked with small red dots are subject to selection criteria and are excluded from the histogram in the right panel. *Right panel:* Distribution of the *Gaia* EDR3 distances, computed from the inversion of the parallaxes. *Gaia* EDR3 distances to the stars HD 46202 (ID#13) and HD 258691 (ID#4) are marked by the squares.

**Table C.1.** *Gaia* EDR3 parallaxes and photometric and astrometric measurements for OB stars in the Rosette nebula cluster NGC 2244.

Name	$\varpi$ (mas)	$\mu_\alpha$ (mas yr <sup>-1</sup> )	$\mu_\delta$ (mas yr <sup>-1</sup> )	$G$ (mag)	RUWE
<b>HD 46150</b>	$0.6431 \pm 0.0340$	$-2.096 \pm 0.031$	$-0.196 \pm 0.030$	6.7138	1.04
<b>HD 46223</b>	$0.6968 \pm 0.0264$	$-1.605 \pm 0.026$	$0.111 \pm 0.023$	7.1998	1.06
<b>HD 46149</b>	$0.6385 \pm 0.0323$	$-1.608 \pm 0.032$	$0.310 \pm 0.028$	7.5508	1.06
<b>HD 46484</b>	$0.7025 \pm 0.0279$	$-0.957 \pm 0.028$	$1.153 \pm 0.025$	7.6406	1.11
HD 46106	$0.6468 \pm 0.0388$	$-2.006 \pm 0.035$	$0.316 \pm 0.029$	7.8970	0.81
HD 46202	$0.7087 \pm 0.1148$	$-1.929 \pm 0.110$	$-0.223 \pm 0.110$	8.1580	4.98
<b>HD 46485</b>	$0.7713 \pm 0.0236$	$-1.639 \pm 0.027$	$0.198 \pm 0.024$	8.1657	0.90
<b>HD 46056</b>	$0.6744 \pm 0.0265$	$-1.861 \pm 0.026$	$0.095 \pm 0.024$	8.1836	0.94
HD 259135	$0.6499 \pm 0.0396$	$-1.762 \pm 0.038$	$0.559 \pm 0.034$	8.5275	1.31
HD 259012	$1.3861 \pm 0.1309$	$-2.647 \pm 0.140$	$0.459 \pm 0.124$	9.2978	6.00
<b>HD 259105</b>	$0.7132 \pm 0.0244$	$-1.744 \pm 0.022$	$0.081 \pm 0.021$	9.3355	1.16
HD 258691	$0.6396 \pm 0.1001$	$-2.215 \pm 0.100$	$-0.609 \pm 0.090$	9.5245	6.97
<b>GSC 00154-02337</b>	$0.6991 \pm 0.0220$	$-1.547 \pm 0.020$	$0.288 \pm 0.018$	9.6817	0.97
<b>GSC 00154-02504</b>	$0.7163 \pm 0.0303$	$-1.932 \pm 0.033$	$0.265 \pm 0.032$	10.5832	0.99
HD 259172	$0.7800 \pm 0.0430$	$-1.707 \pm 0.041$	$0.789 \pm 0.035$	10.6365	2.11
HD 259300	$0.6971 \pm 0.0326$	$-1.795 \pm 0.030$	$0.235 \pm 0.029$	10.6983	2.06
NGC 2244 193	$0.5579 \pm 0.1402$	$-1.353 \pm 0.120$	$0.255 \pm 0.107$	10.7182	5.58
HD 259238	$0.6460 \pm 0.0278$	$-1.458 \pm 0.026$	$0.588 \pm 0.024$	11.0311	1.34
<b>GSC 00154-01247</b>	$0.6486 \pm 0.0218$	$-0.966 \pm 0.025$	$0.609 \pm 0.021$	11.0388	1.04
GSC 00154-01007	$0.6727 \pm 0.0193$	$-1.473 \pm 0.019$	$0.700 \pm 0.017$	11.1379	0.84
<b>GSC 00154-02187</b>	$0.6883 \pm 0.0186$	$-0.428 \pm 0.017$	$0.389 \pm 0.016$	11.1721	0.90
HD 259268	$0.4636 \pm 0.1233$	$-1.449 \pm 0.091$	$0.277 \pm 0.090$	11.1782	3.50
<b>GSC 00154-01016</b>	$0.6706 \pm 0.0213$	$-1.440 \pm 0.020$	$0.075 \pm 0.020$	11.3139	0.87
GSC 00154-00234	$0.4683 \pm 0.0200$	$-0.901 \pm 0.020$	$-0.071 \pm 0.017$	11.4294	1.15
<b>GSC 00154-02141</b>	$0.7172 \pm 0.0199$	$-1.779 \pm 0.026$	$0.272 \pm 0.022$	11.5531	1.11
<b>GSC 00154-01753</b>	$0.6008 \pm 0.0226$	$-1.731 \pm 0.021$	$0.193 \pm 0.020$	11.8841	1.17
<b>GSC 00154-02247</b>	$0.6644 \pm 0.0155$	$-1.806 \pm 0.016$	$0.427 \pm 0.014$	12.7080	1.00
GSC 00154-02164	$0.6654 \pm 0.0231$	$-2.042 \pm 0.023$	$-0.268 \pm 0.021$	12.7863	1.24
ALS 15339	$0.2269 \pm 0.0264$	$-0.361 \pm 0.027$	$-0.102 \pm 0.024$	14.5999	1.09
ALS 15335	$0.1942 \pm 0.0247$	$0.073 \pm 0.026$	$0.542 \pm 0.023$	14.6297	1.02
ALS 15336	$0.1959 \pm 0.0324$	$0.072 \pm 0.029$	$0.591 \pm 0.027$	15.0479	0.90

**Notes.** The names of objects used for the distance estimate of the cluster are in bold. We rejected the other objects based on their RUWE factor, discrepant distance or discrepant proper motions.

tion. The distribution of *Gaia* EDR3 distances from the 15 remaining cluster stars (from the inverted parallaxes) are shown in the right panel. We estimate a mean inverted parallax distance of  $d_{\text{NGC 2244}} = 1464^{+94}_{-84}$  pc ( $1\sigma$  standard deviation) to the cluster ( $d_{\text{NGC 2244}} = 1464^{+24}_{-22}$  pc, standard error of the mean). Both sam-

ple stars agree nicely with the cluster distance estimate in terms of *Gaia* EDR3 distance. However, HD 46202 falls short in terms of spectroscopic distance (possibly because of its binarity), while the spectroscopic distance to HD 258691 matches well.

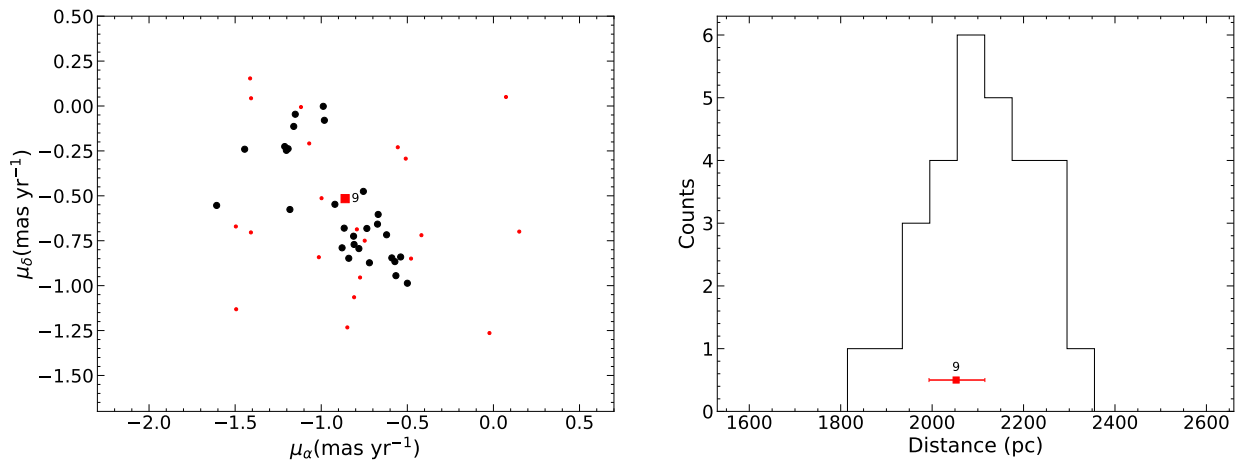


**Fig. D.1.** Same as Fig. C.1, but for OB stars in the cluster IC 1805.

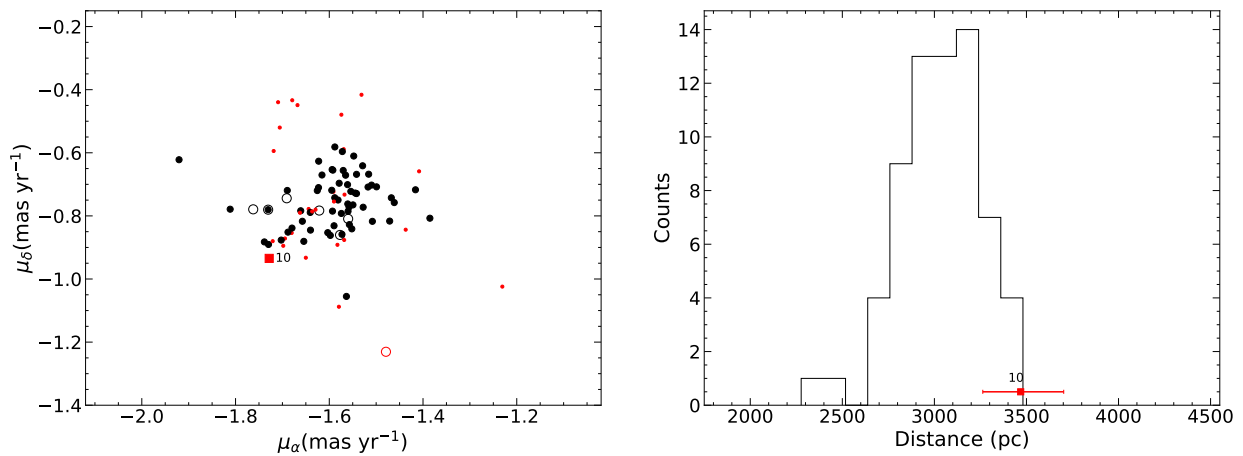


**Fig. E.1.** Proper motion and distances of stars in NGC 457. *Left panel:* *Gaia* EDR3 proper motion of stars in the open cluster NGC 457. Stars marked with small red dots or red circles are subject to selection criteria and are excluded from the histogram in the right panel. Massive stars are marked by open circles. In addition to the massive stars, we included stars with a membership probability  $\geq 70\%$  according to the WEBDA database. *Right panel:* Distribution of the *Gaia* DR3 distances, computed from the inversion of the parallaxes. The sample star BD +57 247 (ID#10) is marked by a square.

## Appendix D: The distance to BD+60 499 and the Heart Nebula cluster IC 1805

The Heart Nebula cluster IC 1805 (Melotte 15, Collinder 26) is the central cluster of the association Cas OB6 in the Perseus spiral arm, with about forty OB star members (Massey et al. 1995; Shi & Hu 1999). The cluster and the surrounding star-forming region W4, and their connection to the close-by star-forming regions W3 and W5, are discussed in detail by Megeath et al. (2008) and Sung et al. (2017). Distances to Cas OB6, including IC 1805, in the range of 2.2 to 2.35 kpc were usually employed in the past (see Megeath et al. 2008), with more recent work indicating  $2.4 \pm 0.2$  kpc for IC 1805 (Sung et al. 2017).

An initial sample of 51 stars of spectral types B3 and earlier with cluster membership probability  $\geq 70\%$  according to Shi & Hu (1999) and including the four brightest O stars of the cluster (Massey et al. 1995) was assembled for the distance estimation to IC 1805 (see Table D.1). Proper motions for these 51 stars and a histogram of the distance distribution of the 29 cluster members, after applying the same selection criteria as for NGC 2244, are shown in Fig. D.1. A distance value of  $d_{IC\ 1805} = 2108^{+129}_{-115}$  pc ( $1\sigma$  standard deviation) or  $d_{IC\ 1805} = 2108^{+24}_{-21}$  pc (standard error of the mean) is derived, slightly shorter than the commonly as-

sumed distance values. Both the spectroscopic and the *Gaia* EDR3-based distance to BD +60 499 agree with the cluster distance within the  $1\sigma$ -uncertainties. The star's proper motions also fit nicely into the proper motion distribution of the cluster stars. We note that the two bright O-star members of IC 1805, HD 15558 and BD +60 497, that were dropped from the cluster average calculations are known binaries (Hillwig et al. 2006; De Becker et al. 2006); some other stars from Table D.1 are probably binaries as well.

## Appendix E: The distance to BD +57 247 and the Owl cluster NGC 457

The open cluster NGC 457 in the Perseus spiral arm is different with respect to all other clusters harbouring O stars from our sample, by lacking active star formation in its vicinity and nebular emission. On the other hand, it possibly harbours three evolved stars, the mid B-type supergiant HD 7902, the yellow supergiant HD 7927 ( $\phi$  Cas) and the red supergiant HD 236697. This is because of its supposedly much older age of about 24 Myr (Kharchenko et al. 2013; Dias et al. 2021). Both these data compilations give also similar distances to NGC 457, of  $2400$  pc (Kharchenko et al. 2013) and  $2540 \pm 133$  pc (Dias

**Table D.1.** *Gaia* EDR3 parallaxes and photometric and astrometric measurements for OB stars in the open cluster IC 1805.

Name	$\varpi$ (mas)	$\mu_\alpha$ (mas yr <sup>-1</sup> )	$\mu_\delta$ (mas yr <sup>-1</sup> )	$G$ (mag)	RUWE
HD 15558	0.5764 ± 0.0662	-0.478 ± 0.063	-0.849 ± 0.064	7.7869	3.06
<b>HD 15570</b>	0.4424 ± 0.0226	-0.720 ± 0.021	-0.873 ± 0.023	7.8909	0.95
<b>HD 15629</b>	0.4848 ± 0.0178	-0.673 ± 0.016	-0.658 ± 0.021	8.2985	0.91
BD +60 497	0.3852 ± 0.0200	-1.496 ± 0.019	-0.671 ± 0.024	8.6066	1.19
<b>BD +60 513</b>	0.4734 ± 0.0153	-0.539 ± 0.014	-0.840 ± 0.017	9.2564	0.90
<b>BD +60 501</b>	0.5060 ± 0.0134	-0.867 ± 0.013	-0.680 ± 0.014	9.4690	0.96
<b>BD +60 498</b>	0.4515 ± 0.0192	-1.192 ± 0.017	-0.238 ± 0.021	9.7939	1.01
<b>BD +60 499</b>	0.4872 ± 0.0145	-0.861 ± 0.013	-0.516 ± 0.015	10.1307	0.97
IC 1805 113	0.4477 ± 0.0470	-1.413 ± 0.047	0.154 ± 0.043	10.4683	3.15
BD +60 496	0.4706 ± 0.0198	-0.848 ± 0.018	-1.233 ± 0.023	10.4816	1.21
IC 1805 161	0.7636 ± 0.0695	-0.809 ± 0.063	-1.065 ± 0.075	10.7771	5.00
IC 1805 259	0.2844 ± 0.3464	-1.494 ± 0.328	-1.131 ± 0.343	10.8137	19.63
IC 1805 21	0.5048 ± 0.0158	-1.408 ± 0.013	-0.704 ± 0.015	10.8269	1.25
IC 1805 211	0.3872 ± 0.1163	-0.023 ± 0.113	-1.264 ± 0.122	10.9194	7.32
IC 1805 136	0.6399 ± 0.1187	-1.118 ± 0.115	-0.006 ± 0.125	10.9250	7.85
<b>BD +60 506</b>	0.4614 ± 0.0194	-0.781 ± 0.019	-0.794 ± 0.019	10.9932	1.18
IC 1805 288	0.4002 ± 0.0179	-0.418 ± 0.017	-0.719 ± 0.020	10.9983	1.07
<b>IC 1805 149</b>	0.4445 ± 0.0178	-0.590 ± 0.017	-0.846 ± 0.019	11.0848	1.03
IC 1805 23	0.5544 ± 0.0506	0.150 ± 0.045	-0.699 ± 0.054	11.1545	3.39
IC 1805 143	0.4324 ± 0.0236	-0.814 ± 0.023	-0.717 ± 0.024	11.2542	1.33
IC 1805 111	0.4274 ± 0.0217	-0.998 ± 0.021	-0.513 ± 0.027	11.3151	1.24
<b>IC 1805 121</b>	0.4405 ± 0.0195	-0.879 ± 0.019	-0.789 ± 0.020	11.4125	1.10
<b>IC 1805 260</b>	0.4517 ± 0.0217	-0.621 ± 0.020	-0.717 ± 0.024	11.4156	1.07
IC 1805 174	0.4858 ± 0.0234	-0.748 ± 0.023	-0.750 ± 0.024	11.4523	1.21
IC 1805 169	0.4852 ± 0.0216	-1.014 ± 0.021	-0.842 ± 0.023	11.4875	1.25
IC 1805 166	0.4102 ± 0.0170	-0.793 ± 0.017	-0.687 ± 0.017	11.8302	1.14
<b>IC 1805 163</b>	0.4726 ± 0.0129	-0.840 ± 0.012	-0.848 ± 0.014	12.0228	0.98
IC 1805 262	0.5504 ± 0.0162	-0.509 ± 0.015	-0.293 ± 0.016	12.0467	1.25
<b>IC 1805 72</b>	0.4246 ± 0.0138	-1.202 ± 0.013	-0.247 ± 0.014	12.0523	1.00
<b>IC 1805 167</b>	0.4930 ± 0.0117	-0.755 ± 0.011	-0.475 ± 0.013	12.1096	0.87
<b>IC 1805 82</b>	0.4576 ± 0.0110	-1.160 ± 0.010	-0.114 ± 0.013	12.1524	0.91
<b>IC 1805 69</b>	0.5029 ± 0.0161	-1.212 ± 0.014	-0.226 ± 0.016	12.1665	1.17
<b>IC 1805 62</b>	0.4891 ± 0.0128	-1.607 ± 0.011	-0.554 ± 0.013	12.2608	1.03
IC 1805 49	0.5230 ± 0.0154	-1.070 ± 0.014	-0.208 ± 0.015	12.2991	1.26
IC 1805 18	0.4090 ± 0.0104	-0.556 ± 0.009	-0.230 ± 0.010	12.3769	0.86
IC 1805 252	0.5635 ± 0.0111	0.073 ± 0.010	0.050 ± 0.011	12.3856	0.90
<b>IC 1805 188</b>	0.4745 ± 0.0134	-0.921 ± 0.013	-0.547 ± 0.016	12.4787	0.93
<b>IC 1805 53</b>	0.5510 ± 0.0145	-1.445 ± 0.012	-0.241 ± 0.014	12.5451	1.03
<b>IC 1805 277</b>	0.4556 ± 0.0127	-0.988 ± 0.011	-0.002 ± 0.014	12.5471	0.88
<b>IC 1805 165</b>	0.4729 ± 0.0115	-0.812 ± 0.010	-0.725 ± 0.011	12.6282	0.90
IC 1805 152	0.5371 ± 0.0356	-0.774 ± 0.033	-0.955 ± 0.036	12.6705	2.64
<b>IC 1805 180</b>	0.4784 ± 0.0138	-0.809 ± 0.013	-0.771 ± 0.014	12.7325	0.92
<b>IC 1805 276</b>	0.4819 ± 0.0150	-0.669 ± 0.014	-0.604 ± 0.016	12.7507	0.97
<b>IC 1805 191</b>	0.4438 ± 0.0127	-1.151 ± 0.012	-0.046 ± 0.014	12.7637	0.95
<b>IC 1805 52</b>	0.5221 ± 0.0130	-1.182 ± 0.011	-0.576 ± 0.012	12.7866	0.98
<b>IC 1805 332</b>	0.5062 ± 0.0159	-0.982 ± 0.016	-0.080 ± 0.017	12.8183	1.05
<b>IC 1805 175</b>	0.4638 ± 0.0167	-0.566 ± 0.015	-0.945 ± 0.016	12.8432	1.03
IC 1805 68	0.4145 ± 0.0183	-1.408 ± 0.016	0.043 ± 0.019	12.9683	1.09
<b>IC 1805 212</b>	0.4931 ± 0.0192	-0.572 ± 0.020	-0.866 ± 0.022	12.9863	1.10
<b>IC 1805 157</b>	0.4598 ± 0.0126	-0.735 ± 0.012	-0.682 ± 0.013	13.2631	0.98
<b>IC 1805 225</b>	0.4705 ± 0.0145	-0.500 ± 0.014	-0.987 ± 0.016	13.4357	0.94

**Notes.** The names of objects used for the distance estimate of the cluster are in bold. We rejected the other objects based on their RUWE factor, discrepant distance or discrepant proper motions.

et al. 2021, thought their *Gaia* DR2-based cluster mean parallax of  $0.318 \pm 0.047$  mas implies a longer distance). The cluster is centred in proper motion space on  $\mu_\alpha = -1.58$  mas yr<sup>-1</sup> and  $\mu_\delta = -0.76$  mas yr<sup>-1</sup> from an analysis of 458 cluster members (Flynn et al. 2022), based on *Gaia* EDR3 data.

The five OB stars plus possibly three supergiants (see Table E.1) are a too small number of stars to pursue a discussion as for the other clusters here. We therefore added all NGC 457 stars with a membership probability  $\geq 70\%$  according to the WEBDA database for our distance investigation (these stars are not in-

cluded in Table E.1). The same selection criteria as used before were employed. The proper motion distribution of this test star ensemble is displayed in the left panel of Fig. E.1, matching nicely the above stated central value. A histogram of the distance distribution of the stars that passed the selection procedure are shown in the right panel of Fig. E.1. Based on this, we estimate a mean inverted parallax distance of  $d_{\text{NGC 457}} = 3026^{+262}_{-223}$  pc ( $1\sigma$  standard deviation) to NGC 457, or  $d_{\text{NGC 457}} = 3026^{+32}_{-27}$  pc (standard error of the mean). This is significantly farther away than previously assumed in the literature.



**Table E.1.** *Gaia* EDR3 parallaxes and photometric and astrometric measurements for massive stars in the open cluster NGC 457.

Name	$\varpi$ (mas)	$\mu_\alpha$ (mas yr <sup>-1</sup> )	$\mu_\delta$ (mas yr <sup>-1</sup> )	$G$ (mag)	RUWE
HD 7927	0.2142 ± 0.0838	-1.479 ± 0.056	-1.231 ± 0.068	4.7361	0.92
<b>HD 7902</b>	0.3679 ± 0.0169	-1.560 ± 0.013	-0.809 ± 0.016	6.8426	0.92
<b>HD 236697</b>	0.3102 ± 0.0182	-1.730 ± 0.012	-0.780 ± 0.015	7.5056	0.87
<b>BD +57 243</b>	0.3335 ± 0.0122	-1.577 ± 0.009	-0.860 ± 0.011	9.2586	0.97
<b>BD +57 252</b>	0.3179 ± 0.0134	-1.621 ± 0.009	-0.783 ± 0.011	9.4132	0.88
<b>HD 236689</b>	0.3501 ± 0.0147	-1.762 ± 0.010	-0.779 ± 0.012	9.4658	0.95
<b>BD +57 249</b>	0.3402 ± 0.0133	-1.691 ± 0.010	-0.744 ± 0.011	9.7400	0.90
BD +57 247	0.2883 ± 0.0182	-1.728 ± 0.013	-0.935 ± 0.017	9.8529	0.94

**Notes.** The names of objects used for the distance estimate of the cluster are in bold. We rejected HD 7927 and BD +57 247 based on the parallax.

Our sample star BD +57 247 overlaps both in *Gaia* EDR3 and spectroscopic distance with the farthest bin of the distance distribution of NGC 457. From a statistical viewpoint it may therefore be a cluster member, as its proper motions also match those of other cluster stars. However, its  $G$  magnitude is 0.6 mag fainter than that of the brightest main-sequence star of the cluster, the B0IV star BD +57 243. The other three massive main-sequence stars, of spectral types B1 to B1.5, are also brighter, though they should be fainter by more than a magnitude if located at the same distance. The difference is so large that it cannot be resolved by differential extinction (the dust emission in the WISE bands appears rather smooth towards the cluster) or binarity (the maximum magnitude difference would be 0.75 mag for two equally bright components). A blue straggler scenario for the star (Mermilliod 1982) can therefore also be excluded, as it should be brighter than the cluster main-sequence B stars. As a consequence, BD +57 247 is probably lying about 400 pc farther away than NGC 457. This is further supported by stronger absorption in the interstellar Na D lines in BD +57 247 when compared to the cluster member supergiant HD 7902 (Weßmayer et al. 2022, and see below), and in particular in the unsaturated interstellar K I resonance line.

Finally, we want to comment on the cluster age. An age of ~24 Myr as given in the literature (Kharchenko et al. 2013; Dias et al. 2021) is incompatible with any of the massive member stars on the main sequence. Even the least massive of spectral type B1.5 V would have reached termination of core hydrogen-burning after this time. NGC 457 must therefore be younger and the presence of the supergiants helps enormously in the age determination. In fact, a high-resolution spectrum of the B6 Ia star HD 7902 has recently been analysed using the same analysis methodology as employed here (Weßmayer et al. 2022). A spectroscopic distance of  $2900 \pm 280$  pc confirms it to be a cluster member. It had a ZAMS mass of  $\sim 20 M_\odot$  and is with an age of ~9 to 10 Myr way younger than the literature cluster age. Such an age would also be compatible with the luminosity class IV of the B0 star and of luminosity class V of the B1 and B1.5 stars. We do not consider the EDR3 parallax for the F0 Ia supergiant  $\phi$  Cas to be reliable as the star is bright for the *Gaia* mission, similar to the case of 10 Lac. Nonetheless, its enormous luminosity ( $B.C.$  is close to zero) may be compatible with cluster membership and cluster age if the star was initially somewhat more massive than HD 7902 and has already advanced well beyond the red supergiant stage (see Fig. 1 of Hirschi et al. 2004 for an exemplary evolution track). The red supergiant HD 236697 appears to be a cluster member from its parallax and kinematics, but it would require substantial extinction to raise its luminosity to fit the ~9 to 10 Myr cluster age. Such extinction could be provided by dust formation in its circumstellar envelope, which is not uncommon among massive red supergiants.

## Appendix F: The distance to HD 206183, HD 207538, and the cluster IC 1396

The cluster IC 1396 (Trumpler 37, Collinder 439) in the Cep OB2 association in the Local spiral arm is one of the youngest among the relatively nearby open clusters showing active star formation (for an overview, see Kun et al. 2008; Errmann et al. 2013). Its age is in the range of 3 to 5 Myr and a distance of about 800 and 870 pc, respectively, in the direction of Galactic rotation was advocated by the two sources.

We used an analogous procedure and selection criteria to identify member stars as discussed before. A starting sample of 38 OB stars of spectral type B3 and earlier was based on the data of Garrison & Kormendy (1976) (see our Table F.1). The proper motion distribution of these stars is visualised in the left panel of Fig. F.1 and a histogram of the distance distribution of the 20 stars that passed the selection procedure are shown in the right panel. From the mean inverted parallax we estimate a distance to IC 1396 of  $d_{IC\ 1396} = 954^{+119}_{-95}$  pc ( $1\sigma$  standard deviation) or  $d_{IC\ 1396} = 954^{+27}_{-21}$  pc (standard error of the mean), slightly farther away than suggested in the pre-*Gaia* era. The *Gaia* EDR3 and spectroscopic distances of both sample stars in IC 1393, HD 206183 and HD 207538 agree with this cluster distance within the mutual  $1\sigma$  uncertainties. Also, the stars' proper motions fit into the range spanned by the other cluster members.

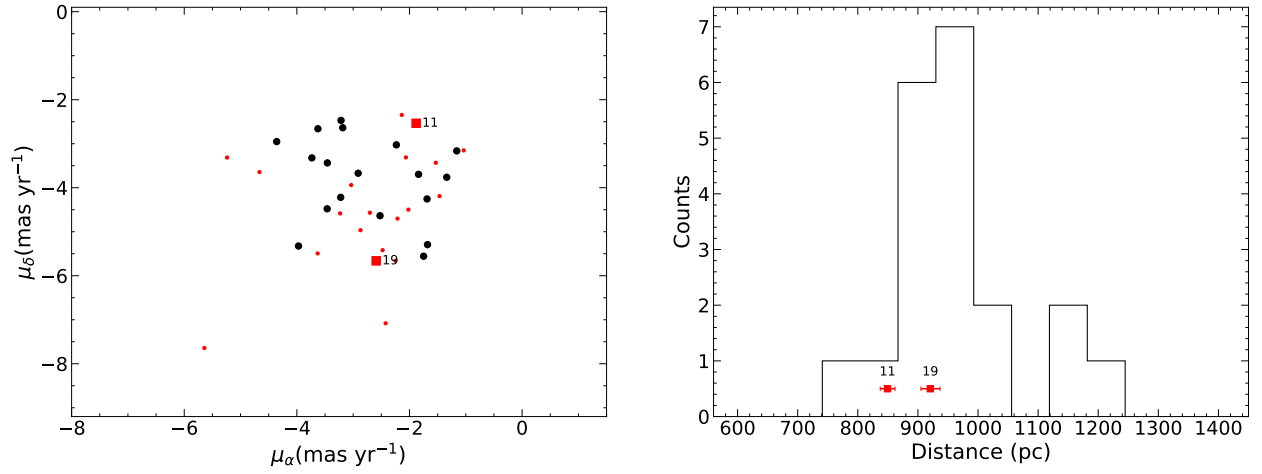


**Fig. F.1.** Same as Fig. C.1, but for OB stars in the cluster IC 1396.

**Table F.1.** *Gaia* EDR3 parallaxes and photometric and astrometric measurements for OB stars in the cluster IC 1396.

Name	$\varpi$ (mas)	$\mu_\alpha$ (mas yr $^{-1}$ )	$\mu_\delta$ (mas yr $^{-1}$ )	$G$ (mag)	RUWE
HD 206267	$1.3604 \pm 0.2188$	$-3.631 \pm 0.224$	$-5.493 \pm 0.281$	5.6124	5.07
<b>HD 206773</b>	$1.0958 \pm 0.0191$	$-1.688 \pm 0.024$	$-4.255 \pm 0.026$	6.7327	0.98
<b>HD 205196</b>	$0.9713 \pm 0.0155$	$-3.733 \pm 0.021$	$-3.322 \pm 0.018$	7.1805	0.96
<b>HD 207538</b>	$1.1773 \pm 0.0170$	$-1.882 \pm 0.020$	$-2.535 \pm 0.019$	7.2152	0.95
<b>HD 206183</b>	$1.0862 \pm 0.0188$	$-2.591 \pm 0.022$	$-5.662 \pm 0.022$	7.3983	0.89
HD 204827	$1.0765 \pm 0.0988$	$-3.231 \pm 0.132$	$-4.584 \pm 0.128$	7.7181	6.67
HD 205329	$0.3658 \pm 0.4385$	$-2.063 \pm 0.527$	$-3.311 \pm 0.446$	7.9544	24.84
<b>HD 239729</b>	$1.0704 \pm 0.0195$	$-2.523 \pm 0.023$	$-4.636 \pm 0.021$	8.2288	1.07
HD 205794	$1.0843 \pm 0.0144$	$-1.466 \pm 0.017$	$-4.191 \pm 0.016$	8.2861	0.84
HD 239712	$1.4020 \pm 0.0156$	$-5.642 \pm 0.019$	$-7.643 \pm 0.018$	8.3937	1.03
HD 239738	$1.0478 \pm 0.0323$	$-2.136 \pm 0.040$	$-2.347 \pm 0.038$	8.5064	1.59
<b>HD 205948</b>	$1.0679 \pm 0.0162$	$-3.222 \pm 0.021$	$-4.219 \pm 0.019$	8.5433	0.87
HD 206081	$1.1328 \pm 0.0407$	$-3.035 \pm 0.058$	$-3.940 \pm 0.046$	8.5563	2.23
<b>HD 239748</b>	$1.0778 \pm 0.0221$	$-1.160 \pm 0.031$	$-3.164 \pm 0.027$	8.6936	1.01
HD 239689	$1.1303 \pm 0.0133$	$-2.018 \pm 0.018$	$-4.498 \pm 0.014$	8.7965	0.82
<b>HD 239745</b>	$1.0706 \pm 0.0163$	$-1.680 \pm 0.018$	$-5.294 \pm 0.015$	8.8278	0.87
V* V427 Cep	$0.8514 \pm 0.0123$	$-2.703 \pm 0.017$	$-4.568 \pm 0.014$	8.9443	0.85
HD 239724	$0.4645 \pm 0.0124$	$-4.664 \pm 0.014$	$-3.644 \pm 0.013$	8.9996	0.81
<b>HD 239731</b>	$1.0486 \pm 0.0133$	$-2.233 \pm 0.016$	$-3.026 \pm 0.015$	9.0408	1.08
V* AI Cep	$0.5235 \pm 0.0141$	$-5.238 \pm 0.017$	$-3.314 \pm 0.015$	9.0573	1.06
HD 239725	$1.0922 \pm 0.0454$	$-2.248 \pm 0.050$	$-5.660 \pm 0.052$	9.0685	2.75
<b>HD 239703</b>	$0.9766 \pm 0.0121$	$-2.912 \pm 0.017$	$-3.671 \pm 0.016$	9.1017	0.99
<b>HD 239683</b>	$1.0857 \pm 0.0128$	$-4.358 \pm 0.015$	$-2.952 \pm 0.016$	9.2378	0.98
<b>HD 239722</b>	$1.3496 \pm 0.0106$	$-3.971 \pm 0.013$	$-5.325 \pm 0.012$	9.3433	0.88
<b>HD 239742</b>	$1.0242 \pm 0.0186$	$-1.749 \pm 0.021$	$-5.557 \pm 0.020$	9.3456	1.14
<b>HD 239710</b>	$1.0686 \pm 0.0134$	$-3.462 \pm 0.017$	$-4.480 \pm 0.015$	9.3663	0.96
BD +57 2395	$1.0964 \pm 0.0195$	$-1.037 \pm 0.023$	$-3.152 \pm 0.024$	9.4444	1.44
<b>HD 239693</b>	$1.0975 \pm 0.0156$	$-1.839 \pm 0.020$	$-3.696 \pm 0.017$	9.5120	1.19
<b>BD +57 2376</b>	$0.8582 \pm 0.0129$	$-3.459 \pm 0.017$	$-3.436 \pm 0.015$	9.6299	0.97
<b>HD 239746</b>	$0.8483 \pm 0.0112$	$-3.215 \pm 0.015$	$-2.471 \pm 0.012$	9.7440	0.90
V* V738 Cep	$1.1851 \pm 0.0088$	$-2.423 \pm 0.011$	$-7.081 \pm 0.012$	9.7550	0.81
<b>BD +58 2292</b>	$0.8033 \pm 0.0162$	$-3.185 \pm 0.018$	$-2.638 \pm 0.018$	9.7551	0.96
<b>BD +58 2294</b>	$1.0619 \pm 0.0128$	$-1.338 \pm 0.015$	$-3.762 \pm 0.013$	9.8482	0.96
BD +56 2596	$1.1322 \pm 0.0296$	$-2.870 \pm 0.039$	$-4.965 \pm 0.031$	9.9765	2.04
BD +56 2622	$1.0595 \pm 0.0118$	$-2.213 \pm 0.014$	$-4.702 \pm 0.013$	10.0479	0.79
<b>BD +57 2358</b>	$1.1290 \pm 0.0127$	$-3.626 \pm 0.016$	$-2.660 \pm 0.014$	10.0703	0.99
BD +57 2395B	$1.0984 \pm 0.0192$	$-1.533 \pm 0.023$	$-3.432 \pm 0.023$	10.1156	1.46
Cl Trumpler 37 430	$1.0707 \pm 0.0185$	$-2.477 \pm 0.026$	$-5.419 \pm 0.019$	10.2841	0.85

**Notes.** The names of objects used for the distance estimate of the cluster are in bold. We rejected the other objects based on their RUWE factor, discrepant distance or discrepant proper motions.